



저작자표시-비영리-변경금지 2.0 대한민국

이용자는 아래의 조건을 따르는 경우에 한하여 자유롭게

- 이 저작물을 복제, 배포, 전송, 전시, 공연 및 방송할 수 있습니다.

다음과 같은 조건을 따라야 합니다:



저작자표시. 귀하는 원저작자를 표시하여야 합니다.



비영리. 귀하는 이 저작물을 영리 목적으로 이용할 수 없습니다.



변경금지. 귀하는 이 저작물을 개작, 변형 또는 가공할 수 없습니다.

- 귀하는, 이 저작물의 재이용이나 배포의 경우, 이 저작물에 적용된 이용허락조건을 명확하게 나타내어야 합니다.
- 저작권자로부터 별도의 허가를 받으면 이러한 조건들은 적용되지 않습니다.

저작권법에 따른 이용자의 권리는 위의 내용에 의하여 영향을 받지 않습니다.

이것은 [이용허락규약\(Legal Code\)](#)을 이해하기 쉽게 요약한 것입니다.

[Disclaimer](#)

공학박사학위논문

**Boiling Heat Transfer Characteristics of  
Water Jet Impingement on Hot Steel  
Surface : Experiment and Analysis**

고온 표면에서 충돌 수분류에 의한 비등 열전달  
특성 : 실험 및 해석

2017년 8월

서울대학교 대학원

기계항공공학부

이 상 건

# Boiling Heat Transfer Characteristics of Water Jet Impingement on Hot Steel Surface : Experiment and Analysis

고온 표면에서 충돌 수분류에 의한 비등 열전달  
특성 : 실험 및 해석

지도교수 김 찬 중

이 논문을 공학박사 학위논문으로 제출함

2017년 8월

서울대학교 대학원

기계항공공학부

이 상 건

이상건의 공학박사 학위논문을 인준함

2017년 8월

위원장 : 이 우 일



부위원장 : 김 찬 중



위원 : 김 민 수



위원 : 이 정 호



위원 : M. Kaviani

# Abstract

Sang Gun Lee

School of Mechanical and Aerospace Engineering

The Graduate School

Seoul National University

Boiling heat transfer of subcooled water impingement on highly superheated plate is investigated by means of heat transfer analysis and high-definition flow visualization. The stainless-steel plate initially heated up to 900°C by an induction heating method is cooled by water of 15°C. The surface temperature and heat flux are estimated by solving 2-D inverse heat conduction problem. The temporal visualization during quench subcooled-jet impingement boiling is synchronized with the heat transfer measurement in the corresponding surface temperature and heat flux. Spread of the subcooled jet over the horizontal plate shows a quasi-steady regime where the wetting front spreads linearly with time. The time for onset of the quasi-steady regime can be explained by a quasi-steady time. The front separates the single-phase/collapsed-bubble region from the outside region which is dry if not for the impinging droplets ejected from the front. As the front expands, the surface experiences sequence of single-phase, collapsed-bubble, wetting front evaporation, ejected-droplet evaporation cooling. The fraction of water ejected from the front increases linearly with time (reaches over 10%) and is predicted.

After that, enhancement resulting from interaction of two adjacent jets impinging

on largely superheated stainless-steel plate is investigated. Subcooled water jets with varying jet separation distance (up to 30 nozzle diameter) show that following an elapsed time of isolated-jet behavior, the spreading liquid wetting fronts merge and in the merged region the heat transfer coefficient increases substantially. This enhancement is presented as the two-jet cooling efficiency and we show this efficiency initially increases with the increase in separation distance, reaching a peak and then vanishes for large separation.

Finally, the comparative study of 4-type of quenching methods on hot steel block is experimentally performed with heat transfer analysis and microscopic examination. For the comparison, water/oil immersion, forced immersion and multiple jet quenching are selectively adopted. Two material types of steel such as stainless steel (SUS310S) and alloy steel (SNCM439) are used to compare boiling heat transfer characteristics and microscopic examination, separately. The surface temperature and heat flux are determined by solving inverse heat conduction and followed boiling phenomena are visualized by high-speed imaging. Furthermore, microscopic examination was performed with SEM to verify the metallographic structures after each quenching method, and the mechanical properties are also examined. All 4-type methods showed qualitative agreement in the variation of martensitic fraction depending on each cooling rate. As the surface is cooled more rapidly, the higher volume fraction of martensite are formed and shows enhanced mechanical properties.

**Keyword :** water jet impingement, two interacting jets, multiple jet quenching, boiling heat transfer, inverse heat conduction, microscopic examination

**Student Number :** 2011-20732

# **Contents**

<b>Abstract</b> .....	<b>i</b>
<b>Contents</b> .....	<b>iii</b>
<b>Nomenclature</b> .....	<b>v</b>
<b>List of Tables</b> .....	<b>vi</b>
<b>List of Figures</b> .....	<b>xiii</b>
<b>1. Introduction</b> .....	<b>1</b>
1.1 Overview .....	1
1.1.1 Overview of Liquid Jet Impingement .....	1
1.1.2 Boiling Mechanism of Jet Impingement Boiling .....	4
1.2 Objectives of Present Study .....	8
<b>2. Experimental Apparatus and Arrangements</b> .....	<b>16</b>
2.1 Flow System of Single/Two Jet Impingement .....	16
2.2 Experimental Apparatus for 4-types of Quenching Method .....	20
2.3 Experimental Conditions of Present Study .....	26
<b>3. Estimate Thermal Boundary Condition and Microscopic Analysis</b> .....	<b>28</b>
3.1 Inverse Heat Conduction Problem (IHCP) .....	28
3.1.1 Overview of IHCP .....	28
3.1.2 Algorithm/Calculation of IHCP .....	32
3.1.3 Evaluation of Heat Transfer Coefficient .....	35
3.2 Microscopic Analysis of Quenched Surface .....	37
<b>4. Experimental Results and Discussion</b> .....	<b>39</b>
4.1 Quasi-steady Front in Single Subcooled-jet Impingement Boiling .....	39
4.1.1 Flow Visualization and Cooling Regions .....	39
4.1.2 Quasi-steady Regime .....	46
4.1.3 Wetting Front Propagation .....	50
4.1.4 Fraction of Liquid Ejected at Propagating Front .....	53
4.2 Effect of Two Interacting Jets on Boiling Heat Transfer .....	56

4.2.1 Flow Visualization and Cooling Regions .....	56
4.2.2 Boiling Heat Transfer Analysis of Two Interacting Jets .....	60
4.2.3 Enhancement of Two Interacting Jet .....	70
4.3 Comparison of 4-type of Quenching Method .....	74
4.3.1 Comparison of Heat Transfer Analysis of 4-type of Quenching Methods .....	74
4.3.2 Comparison of Microstructure Analysis of 4-type of Quenching Methods .....	88
<b>5. Concluding Remarks .....</b>	<b>92</b>
<b>References .....</b>	<b>95</b>
<b>Abstract in Korean .....</b>	<b>102</b>

# List of Tables

Table 2.1 Arrangement of experimental configurations and conditions of present study.

# List of Figures

Figure 1.1 Various boiling regimes with temperature distribution of highly heated surface cooled with water coolant.

Figure 1.2 Axisymmetric schematic of spreading of subcooled water circular jet over a superheated horizontal plate, showing the geometric parameters, flow regimes, and plate transient conduction.

Figure 1.3 CCT diagram of SNCM439 alloy steel with various cooling curves.

Figure 2.1 Schematic of the jet quench boiling experiment and its components.

Figure 2.2 (a) Image of the stainless steel plate and the locations of the thermocouples, (b) Schematic of the thermocouple-holes for measuring temperature.

Figure 2.3 Schematic and experimental apparatus for water/oil immersion quenching methods(1st and 2nd types).

Figure 2.4 Schematic of experimental setup of forced immersion(3rd type) and multiple jet quenching(4th type) methods.

Figure 2.5 Experimental apparatus of forced immersion (3rd type) and multiple jet quenching (4th type) methods.

Figure 2.6 Image of steel block and schematic of the thermocouple-holes for measuring temperature for steel material of (a) stainless steel (SUS310S), (b) alloy steel (SNCM439).

Figure 3.1 Flow chart of 2-D inverse heat conduction problem for determining the transient surface temperature and heat flux distributions based on internally measured temperatures.

Figure 3.2 Comparison between the measured and predicted (inverse heat conduction) plate temperature distributions at several radial locations: (a) 1 mm below surface and (b) at surface.

Figure 4.1 Snapshot images of spreading jet, for several elapsed times, showing the wetting front, liquid eject (droplets), and eventual cooling of the plate (fading out red color). The progressively increasing central single-phase and the collapsed-bubble regions are also observed. The radial location is shown at the bottom of each snapshot.

Figure 4.2 Snapshot image comparison at two elapsed times, with marking of the various regions. (a) Plate has significant superheat, and (b) plate is significantly cooled with large subcooled single-phase inner region. The spread of the wetting front is linear with time. The fraction liquid eject from the front remains constant with time, but the front perimeter increases so the droplet are more spread.

Figure 4.3 Variations of the transient local surface flux with respect to local surface superheat at various radial locations: (a) inner, (b) middle, and (c) outer regions. Note that two set of data are shown for each radial location (one each side) to confirm presence of symmetry. The inner region is least affected by cooling with the ejected droplets, so has experiences rather steady cooling, while the outer region is substantially cooled by droplets before the front arrives.

Figure 4.4 (a) Variations of local surface heat flux distribution with respect to the local surface superheat and (b) variations of the local surface heat flux and heat transfer coefficient with respect to time, at locations  $r/D_n = \pm 30$ . (c) and (d), same but for  $r/D_n = \pm 40$ . Various cooling regime encountered are also shown.

Figure 4.5 Snapshot image combined with the radial distributions of the surface heat flux and heat transfer coefficient at wetting front radii  $R_{do}/D_n$  (a)  $\pm 0$ , (b)  $\pm 5$ , (c)  $\pm 10$ , and (d)  $\pm 15$ . The elapsed time is chosen accordingly to reveal the regimes.

Figure 4.6 Same as Figure 2.10, but for  $R_{do}/D_n$  (a)  $\pm 20$ , (b)  $\pm 25$ , (c)  $\pm 30$ , and (d)  $\pm 35$ . The elapsed time is also chosen accordingly to reveal the regimes.

Figure 4.7 Variations of the inverse-conduction predicted temperature distribution within the plate at several elapsed times. The onset of the quasi-steady behavior is marked by the quasi-steady time reaching the back of the plate.

Figure 4.8 Three-dimensional presentation of the simultaneous variations of the surface heat flux, surface temperature, and the elapsed time of (a) 0~24 (i.e.,  $\tau_{qs}$ ), and (b) 24~200 s, at several radial locations. The quasi-steady regime is noted with a similarity of the cooling behavior at various locations.

Figure 4.9 Variation of the wetting front location with respect time, showing the quasi-steady regime where  $R_{do}$  increases linearly with time. The position of the maximum heat flux at specific time is also marked.

Figure 4.10 (a) Variations of the fraction of liquid ejected at wetting front and evaporating as droplets in the dry region against the elapsed time and (b) variations of the fraction of liquid ejected at wetting front with the value of maximum heat flux along the radial position.

Figure 4.11 Schematic of two interacting water circular jets over a superheated horizontal plate.

Figure 4.12 Flow visualization of two interacting jets along with different width per nozzle diameter ( $W/D_n$ ) of (a) 10, (b) 20, (c) 30.

Figure 4.13 Snapshot images of boiling visualization of  $W/D_n = 30$  at three elapsed times. The inner part of two jets wets faster than that of outside part.

Figure 4.14 Snapshot of boiling visualization at the center wetting time of  $W/D_n$  (a) 10, (b) 20, (c) 30.

Figure 4.15 Sequence images of two interacting jet quench along to jets separation distance at elapsed times of (a) 12, (b) 50, (c) 150 s.

Figure 4.16 Snapshot image combined with the radial distributions of the surface heat flux and heat transfer coefficient of  $W/D_n = 10$  case at elapsed time of (a) 4.5, (b) 20, (c) 50, and (d) 100s.

Figure 4.17 Snapshot image combined with the radial distributions of the surface heat flux and heat transfer coefficient of  $W/D_n = 20$  case at elapsed time of (a) 4.5, (b) 20, (c) 50, and (d) 100s.

Figure 4.18 Snapshot image combined with the radial distributions of the surface heat flux and heat transfer coefficient of  $W/D_n = 30$  case at elapsed time of (a) 15, (b) 34, (c) 42, and (d) 50 s.

Figure 4.19 Snapshot image combined with the radial distributions of the surface heat flux and heat transfer coefficient of  $W/D_n = 30$  case at elapsed time of (a) 62, (b) 80, (c) 100, and (d) 150 s.

Figure 4.20 Surface temperature distribution along with time of  $W/D_n$  of (a) 10, (b) 20 and (c) 30. The thick red line represents the center position of plate.

Figure 4.21 Heat flux distribution against the temperature of  $W/D_n$  of (a) 10, (b) 20 and (c) 30. The thick red line represents the center position of plate.

Figure 4.22 Variations of the inverse-conduction predicted temperature distribution in radial direction at elapsed time of (a) 50, (b) 100 s.

Figure 4.23 Variation of the wetting front location with respect time, showing the quasi-steady regime where  $R_{do}$  increases linearly with time.

Figure 4.24 Comparison of boiling visualization and heat transfer coefficient between single jet and two interacting jet of  $W/D_n = 10$ .

Figure 4.25 Heat transfer coefficient enhancement ( $\eta$ ) of single jet and two interacting jet of  $W/D_n = 10$ .

Figure 4.26 Comparison of (a) heat transfer coefficient, (b) efficiency enhancement between single jet and two interacting jet of  $W/D_n = 10, 20, 30$  at elapsed time 50 s.

Figure 4.27 Sequence of high-speed imaging of water immersion quenching at lateral surface with rotating speed of (a) no rotation and (b) 300 rpm.

Figure 4.28 Temperature distribution of water immersion quenching at rotating speed (a) no rotation, (b) 3000 rpm at T-top, L-lateral and B-bottom surface.

Figure 4.29 Heat transfer distribution of water immersion quenching at rotating speed (a) no rotation, (b) 3000 rpm at T-top, L-lateral and B-bottom surface.

Figure 4.30 Temperature distribution of oil immersion quenching at rotating speed (a) no rotation, (b) 3000 rpm at T-top, L-lateral and B-bottom surface.

Figure 4.31 Heat transfer distribution of oil immersion quenching at rotating speed (a) no rotation, (b) 3000 rpm at T-top, L-lateral and B-bottom surface.

Figure 4.32 Comparison of cooling rate of (a) water and (b) oil immersion quenching along the various rotation speed.

Figure 4.33 Consecutive boiling visualization images of forced immersion quenching at lateral surface along the various elapsed time.

Figure 4.34 Temperature distribution of forced immersion quenching with total flow rate of (a) 60, (b) 120m<sup>3</sup>/hr at T-top, L-lateral and B-bottom surface.

Figure 4.35 Heat transfer distribution of forced immersion quenching with total flow rate of (a) 60, (b) 120m<sup>3</sup>/hr at T-top, L-lateral and B-bottom surface.

Figure 4.36 Temperature distribution of multiple jet quenching with flow rate of each multiple jet nozzle (a) 10, (b) 20m<sup>3</sup>/hr at T-top, L-lateral and B-bottom surface.

Figure 4.37 Heat transfer distribution of multiple jet quenching with flow rate of each multiple jet nozzle (a) 10, (b) 20m<sup>3</sup>/hr at T-top, L-lateral and B-bottom surface.

Figure 4.38 Comparison of cooling performance for 4-type quenching methods of (a) cooling curves and (b) cooling rate distribution.

Figure 4.39 Transient temperature distribution of 4-type of quenching methods (a) water immersion, (b) oil immersion, (c) forced immersion and (d) multiple jet quenching at measuring position of 1 mm from surface.

Figure 4.40 SEM images of surface after 4-type of quenching with (a) water immersion, (b) oil immersion, (c) forced immersion and (d) multiple jet quenching.

Figure 4.41 SEM images of surface after 4-type of quenching with (a) water immersion, (b) oil immersion, (c) forced immersion and (d) multiple jet quenching.

Figure 4.42 Comparison of surface elongation profile of 4-type of quenching methods.

Figure 4.43 Hardness profiles of 4-type of quenching methods of elongation at (a) surface and along (b) depth thickness from surface.

# Nomenclature

$A$	area, $m^2$
$D_n$	diameter of circular nozzle, m
$h$	heat transfer coefficient, $W/m^2\cdot k$
$k$	thermal conductivity, $W/m\cdot k$
$L_n$	height position of nozzle, m
$Nu$	local Nusselt number
$q$	heat flux, $W/m^2$
$r$	radial distance from stagnation point, m
$R_{do}$	wetting front radius, m
$Re_D$	nozzle Reynolds number
$\Sigma$	sum of squared function
$T$	temperature, $^{\circ}C$
$u$	velocity, m/sec
$W$	width between two interacting jets, m

## Greek Letters

$\alpha$	thermal diffusivity, $m^2/s$
$\beta$	fraction of liquid undergoing phase change
$\mu$	viscosity, Pa-s
$\rho$	density, $kg\ m^{-3}$
$\delta$	surface tension, N/m
$\tau_{qs}$	quasi-steady time, s

## Subscripts and superscripts

$ab$	ambient
$n$	nozzle
$fg$	evaporation
$ini$	initial

<i>ONB</i>	onset of boiling
<i>qs</i>	quasi-steady
<i>sat</i>	saturation
<i>sub</i>	subcooling
<i>sur</i>	surface
<i>sh</i>	superheat

# Chapter 1. Introduction

## 1.1 Overview

### *1.1.1 Overview of Liquid Jet Impingement*

Impinging jet has been broadly used where higher rates of heat and mass transfer rate. Heat transfer coefficients of this system typically exceed  $10,000 \text{ W/m}^2\text{-}^\circ\text{C}$  of single-phase convection system which is much larger due to the presence of boiling. Many industrial applications include the thermal treatment [1-3], cooling of internal combustion engines [4], and more recently, thermal control of high-heat-dissipation electronic devices [5]. Especially, the production of steel, aluminum, and other metals having desirable mechanical and metallurgical properties requires accurate temperature control. This attractiveness of jet impingement cooling with high heat transfer rate intrigues numerous studies on impinging jets. These are recently review by Wolf et al. [6] for investigations treating liquid jet impingement boiling. This review addresses liquid jets with continuous cross sections, thereby excluding spray and droplet impingement studies.

The jets configurations can be delineated into the five categories of plunging jets, submerged jets, confined jets, wall jets and free-surface jets. For the first four types, the plunging jet differs only in that it impinges into a pool of liquid covering the surface, where the depth of the pool is less than the nozzle-to-surface spacing. The submerged jet where the fluid exits a nozzle or orifice into a body of surrounding fluid is injected directly into a miscible atmosphere (liquid into liquid), and the

confined jet is injected into a region bounded by the impingement surface and nozzle- plate. The wall jet flows parallel to the surface and occurs in both free-surface and submerged configurations [6].

The last free-surface jet is injected from a nozzle or orifice into an atmospheric environment (liquid into gas). The liquid travels relatively unimpeded to the impingement surface and surrounding fluid is therefore negligible. The shape of the free surface is governed by a balance of pressure force, gravity, and surface tension of liquid. The pressure force is determined with nozzle size and orientation. The influence of gravity which is affected by distance to surface may be far more important in free-surface liquid jets than in their submerged jet counterparts. As the free-surface jet strikes the target surface, the flow stagnates and flows outward in a thin liquid layer. At downstream location the liquid layer forms a hydraulic jump because of associated sudden deceleration of the fluid and consequent degradation in transport characteristics. This free-surface jet can be configured in two distinct shape of flow after impinged.

Numerous experimental studies on the heat and mass transfer at the target surface under liquid jets have been conducted to verify the jet theoretical results and to characterize boiling phenomena that are intractable analytically. In experiments, it is highlighted that experimental apparatus must be carefully instrumented so as not to interfere the viscous and thermal boundary layers. Mainly investigated factors affecting free-surface jet are jet Reynolds number, coolant temperature, nozzle configuration and distance of nozzle-to-surface. Copeland [7] and Ruch and Holman [8] performed boiling experiments for a Reynolds number of impinging jet on a

downward-facing, superheated surface. They found that the heat flux in the fully developed nucleate boiling regime was independent of impingement velocity (0.79-6.84 m/s) and depended only on the wall superheat. Otherwise, Monde and Okuma [9] examined about low flow rate for a jet of saturated R-113 and showed that, under some circumstances, the heat flux was clearly affected by the impingement velocity. They also shows the amount of heat extracted from the surface is approximately equal to the latent heat required to evaporate completely the supply of saturated liquid. But, they did not address about the mechanism surrounding this phenomenon. Copeland [7] and Monde and Katto [10], Nonn et al. [11] investigated of the effect of subcooling temperature. They shows that no differences in the boiling curves for water at subcoolings on fully developed nucleate boiling condition. However, Nonn et al. [11] addressed even moderate changes in the degree of subcooling can affect the nucleate boiling heat transfer and heat flux. Several investigations have addressed the dependence of nucleate boiling heat transfer on the nozzle configuration [7-8,10,12]. They all confirmed that fully developed nucleate boiling was not dominantly affected by the jet diameter.

And also, many extra factors have been examined like as multiple jet impingement, wall roughness, jet pulsation/splattering and motion of impingement surface. But, relatively a small number of attempts have been made at determining experimentally the hydrodynamic characteristics of axisymmetric free-surface liquid jets. And only a few studies are performed to thoroughly investigate the boiling mechanism at highly superheated temperature with rapid cooling performance.

### ***1.1.2 Boiling Mechanism of Jet Impingement Boiling***

In moderate quenching method, the mode of heat transfer is primarily forced convection of the vapor, with radiation becoming dominant at higher surface temperatures. But for the jet impingement of rapid quenching method, film boiling can often accompany other regimes of boiling on the same surface. Observations of a transient quench with an impinging jet reveal that, at low subcoolings and high plate temperatures, the jet is isolated from the surface by the vapor layer. As the plate temperature declines, the jet penetrates the vapor and wets the surface surrounding the stagnation point while film boiling persists at locations farther downstream. Likewise, the complex and various boiling phenomenon occurs when the coolant impinges on highly superheated surface.

There exist several boiling regimes like as single-phase forced convection, transition, nucleate and film boiling as shown in Fig. 1.1. The single-phase forced-convection regime represents heat transfer with the absence of boiling, and the relationship between the heat flux and wall superheat is governed by Newton's law of cooling,

$$q = h( \Delta T_{sat} + \Delta T_{sub} ) \quad (1.1)$$

For jet impingement, the convection coefficient ( $h$ ) varies over the surface due to hydrodynamic variations in radial direction. So, factors such as viscosity, boundary layer development and transition affect the distribution of the convection coefficient.[13-15]

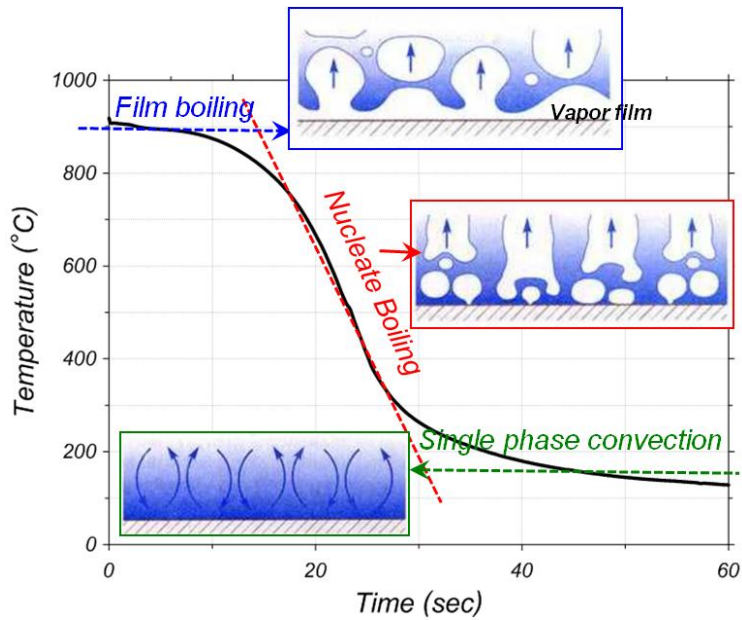


Figure 1.1 : Various boiling regimes with temperature distribution of highly heated surface cooled with water coolant.

The transition boiling regime represents conditions where unstable vapor blankets form and collapse accompanied by intermittent wetting of the surface. This regime occurs at the intermediate time at forming and collapsing of nucleate boiling of fully developed boiling condition. The film boiling regime represents heat transfer from the surface to the liquid across a vapor film. When the highly superheated surface cooled with coolant liquid, rapid evaporation occurs due to the high surface temperature, resulting in the formation of vapor film on the surface. This formed vapor film which acts as a thermal insulator and serves to reduce the cooling performance as shown in early stage of Fig. 1.1.

After film boiling, the surface is start to wet and the nucleate boiling start accompanying high heat transfer and show sharp gradient and the surface is cooled rapidly. The attractive feature of nucleate boiling is the large increase in heat

transfer that accompanies only moderate changes in the surface temperature. Consequently, it is the desired region of operation for many high-heat-flux cooling applications and commonly maximum heat flux obtained through a quench. In jet quenching, single-phase convection occurs at the center of the plate with nucleate boiling around the perimeter for a free-surface, circular jet. With increased heating, the nucleate boiling region propagated inward toward the stagnation point [16-19].

The onset of nucleate boiling (ONB), or boiling incipience, is important for rapid cooling rate because we can approximately predict formation of nucleate boiling. Toda and Uchida [20] reported that the ONB was recognized by both visual observations and a marked change in the slope of the temperature distribution graph of Fig. 1.1. Many researchers have devoted to establish the correlation of boiling incipience. Hsu [21] reported that the ONB depends on heat flux and surface superheat for a given fluid and operating pressure. Moreover, the velocity and subcooling can also affect through their effect on the relationship between heat flux and surface superheat. These effects may be represented by applying Newton's law of cooling at the point of incipience,

$$q_{ONB} = h_{ONB}((\Delta T_{sat})_{ONB} + \Delta T_{sub}) \quad (1.2)$$

The surface superheat in Eqs.(1.2) could be replaced by the convective heat transfer coefficient.

$$(\Delta T_{sat})_{ONB} = \frac{1 + (1 + 4\Gamma\Delta T_{sub})^{1/2}}{2\Gamma} \quad (1.3)$$

So, the Eqs.(1.2) may be expressed directly in terms of  $h_{ONB}$  by

$$q_{ONB} = \frac{h_{ONB}}{2\Gamma} \left[ 1 + (1 + 4\Gamma\Delta T_{sub})^{1/2} \right] + h_{ONB}\Delta T_{sub} \quad (1.4)$$

Where

$$\Gamma = \frac{h_{fg}k_f}{8\sigma T_{sat}v_g h_{ONB}} \quad (1.5)$$

So, the relationship between the convective heat transfer coefficient ( $h_{ONB}$ ) and the impingement velocity would provide closure for the implicit effects of velocity and subcooling on incipience.

## 1.2 Objectives of Present Study

In material processing, the quenching processes strongly control the phase transformation, grain size distribution and thermal stresses of metallic work pieces. By applying proper quenching configuration, we can obtain final products with desirable properties such as low residual stresses, specific hardness, and achievement of improved properties. In the quenching process, the highly heated steel are cooled down to coolant temperature by immersion into a specific liquid, spraying with a liquid or by submerged/free-surface jet impinging over the surface.[22-29] The main purpose of the heating and the holding stages is the transformation of the starting microstructure into a homogeneous austenitic phase. In the quenching, the high temperature austenite is transformed into diverse microstructures, such as ferrite, pearlite, bainite, martensite, and the residual austenite. These various phase distribution after heat treatment can be obtained by adopting different strategy of cooling.[30-32] The cooling rate strongly characterizes the surface morphology, structure and composition of the quenched steel as shown in Fig. 1.2 which shows the CCT diagram of low-alloy steel(SNCM439). Comparing with various cooling curve, a specific quenching rate shows a certain microstructure deformation. With slow and moderate cooling curves, the ferrite with bainite and bainite structure are mainly formed, separately. To form dominant volume fraction of martensite on quenched surface, the highly heated steel has to be quenched instantaneously. This optimization problem will determine the optimum quenching process to form 100 percent martensite up to quenching methods with diverse

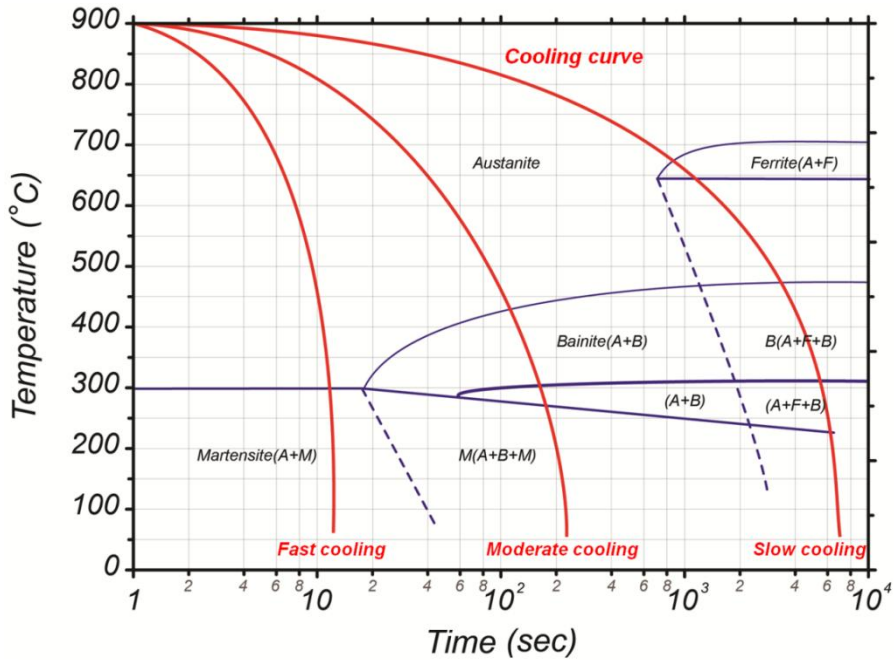


Figure 1.2 : CCT diagram of SNCM439 alloy steel with various cooling curves.

cooling rate.

Water jet impingement has been widely used for its rapid and intensive cooling capacity [33-37]. The surface morphology, structure and composition of the quenched steel are also characterized by the initial heating and then the cooling rate during quenching process. However the fundamental studies of this cooling process are rather sparse due to complexity of its transient, heterogeneous boiling modes, in particular for subcooled jets. The boiling heat transfer is also affected by the dimensions and thermal properties of the quenched material (metallic). So, a thorough understanding of boiling heat transfer, including the hydrodynamic of the jet impingement, is required for predicting the characteristics and the qualitative improvement of material. Here we aim at providing further insights into the jet

quench boiling and Fig. 1.3 gives a schematic of the subcooled circular free-surface jet flowing over a highly superheated surface, showing three different regions, namely the wet, wetting front, and dry region. Furthermore, at the stagnation point shortly after cooling commences, and under high local heat flux (cooling rate), evaporation is suppressed, and single-phase convection cooling continues there. At larger radial locations, the surface temperature is in high and due to the subcooled jet, the region of collapsed-bubble boiling prevails. Further outward, the dry region is reached with an active droplet spouting evaporation front. The otherwise dry region is not cooled by landing of these droplets which evaporate with intensity depending on the local landing site surface superheat.

A review of prior experimental investigations of the characteristics of jet impingement quenching is given by Wolf et al. [6], covering the hydrodynamics of the jet flow, various boiling regimes, and key jet-surface parameters. But, few experiments regarding rapid cooling on a high-temperature surface over 500 °C were investigated due to complicated coupled boiling heat transfer of highly unsteady cooling. The visual observation reveals formation of “dark zone” (contrast by glowing high superheat region) beneath the jet (Karwa et al. [38]) with the surface temperature there under 500 °C with the peripheral boundary of this zone called the wetting front. The liquid deflection was observed outside of wetting front due to surface tension and shear forces. These splashed droplet velocity is governed by jet velocity. Hall et al. [39] and Ishigai et al. [40] reported that film boiling was not observed in the stagnation region with highly subcooled jet, even though an initial temperature of about 1000 °C. They concluded that in the stagnation region direct

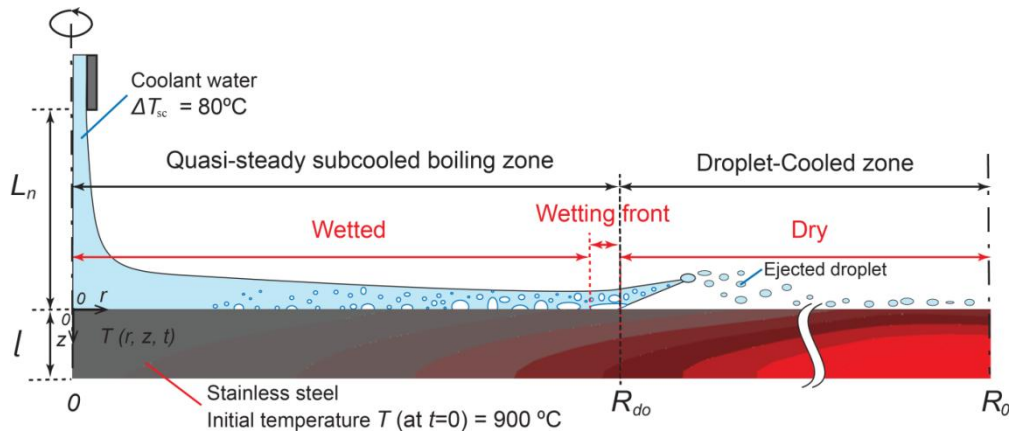


Figure 1.3 : Axisymmetric schematic of spreading of subcooled water circular jet over a superheated horizontal plate, showing the geometric parameters, flow regimes, and plate transient conduction.

contact between the coolant and surface occurred without any noticeable period of film boiling. At the stagnation point, minimum heat flux of film boiling decreased with increasing nozzle diameter and increased with jet velocity and subcooling. Monde and coworkers [41-45] have studied cylindrical plates (copper, brass and carbon steel) with relatively low initial temperature (under 500°C). Woodfield et al. [41] investigated the flow behavior and quenching sound with a high-speed video camera and microphone. They suggested that flow phenomenon can be changed depending on the initial temperature, and the changed flow pattern accompanied different boiling sound. Hasan et al. [45] developed a mechanistic model to describe the homogeneous nucleate boiling of jet impingement by applying the concept of 1-D semi-infinite heat conduction. Toghraie et al. [46, 47] performed numerical analysis about the subcooled jet boiling on hot surface with 800°C. Volume of fluid method was adopted to track the evolving free-surface between two or more fluids.

They numerically confirmed that the increase of jet velocity and subcooled temperature caused an improving in cooling rate and high rewetting temperature. Existence of maximum heat flux ( $q_{\max}$ ) in quench boiling is experimentally by Mozumder et al. [48] and Hammad et al. [49] and they found that  $q_{\max}$  occurs in the nucleate boiling region or boundary between the nucleate boiling and transition boiling region. They reported that the boundary is in the fully-wetted region and location varies with the surface wetting conditions. However, boiling characteristics with very high superheat and larger plate surface area, and its theoretical analysis, are still unanswered.

The first object of this study is to investigate using high-resolution imaging and analyse the hydrodynamics of round, subcooled (80°C subcooling) single water jet (jet Reynolds number of 15,000) quench boiling of large stainless-steel plate area under very high initial temperature (900°C). We use the axisymmetric inverse heat conduction problem (IHCP) to determine the transient plate temperature distribution, and predict the transient surface heat flux distribution. We explain the various boiling regions (spatial) and regimes (temporal), including the presence of a quasi-steady cooling behavior.

Moreover, we adopt the two interacting jets to evaluate the enhancement by comparing with single jet impingement in previous section. The flow visualization is performed beforehand quenching to characterize the interacting jet flow. The experimental conditions like as initial/coolant temperature, jet Reynolds number and nozzle height are set as a same value for comparison. And also, we adopt 4-type of quenching methods to compare the heat treatment rate and following microstructure.

Immersion quenching technique is adopted for the quenching type 1<sup>st</sup> and 2<sup>nd</sup>. Among various heat treatment methods available, immersion quenching process has widely used to minimize the formation of undesirable thermal and transformational gradients which may lead to distortion and cracking.[22,32] The quenching medium for immersion quenching is diversely selected as water, oils and aqueous polymer solutions. But, C.E. Bates[50] mentioned that direct immersion into highly subcooled water can induce large temperature differences areas of a part. This can cause unpredictable distortions and have a deleterious effect after quenching. To minimize the distortion, other coolant medium of oil or polymers can be a substitute of water coolant by inducing the slow cooling rate which improves the temperature uniformity. However, a low cooling speed may result in some precipitation that impairs the strength and corrosion resistance of the steel.

N. I. Kobasko et al.[51-52] developed the Intensive Quenching(IQ) technique is an alternate way of hardening steel parts. They commercially patented IntensiQuench<sup>SM</sup> process which is defined as cooling at a rate several times higher than the rate of conventional quenching like as immersion quenching of type 1<sup>st</sup> and 2<sup>nd</sup>. Kobasko's research calls for very high cooling rates for parts within the martensite phase and showed that very fast and uniform part cooling actually reduced the probability of part cracking and distortion, while improving the surface hardness and durability of steel parts. The water falls down with high flow rate on the upper part of hot steel. We name for this quenching technique as forced immersion quenching and adopt as 3<sup>rd</sup> quenching type.

Another quenching technique widely used for rapid cooling performance is water

jet impingement. We developed multiple jets impinging with staggered array nozzles and adopt as 4<sup>th</sup> quenching type. The injected water jet from the nozzle is directly impinged on surface with high momentum and induces the high cooling rate. Many investigations have been performed about the boiling heat transfer characteristics of jet impingement quenching experimentally. Wolf et al.[6] have integrated the review of jet impingement studies about hydrodynamics of jet flow, various boiling regime and influencing key factors. The visual observation about the formation of a dark zone in a circle beneath the jet is issued by some researchers. N. karwa et al.[34] reported that the surface temperature of relatively dark zone was approximately under 500°C and called the peripheral boundary of this zone as wetting front. Ishigai et al.[40] reported that film boiling was not observed in the stagnation region with an initial temperature of about 1000 °C. The authors concluded that, in the stagnation region, direct contact between coolant and surface occurred without any noticeable period of film boiling. Monde's group[41-44,48-49] have specifically studied with cylindrical shape of specimen at relatively low initial temperature under 500°C.

The third object of this study is to perform comparative analysis of 4-type of quenching methods using the boiling heat transfer and microscopic analysis. The cooling rate and microstructure transformations highly related to the quenching process. We use two of specimen materials of stainless-steel (SUS310S) and alloy steel (SNCM439) for heat transfer analysis and microscopic examination, separately. The 2-D invers heat conduction problem (IHCP) is used as numerical analysis to

determine the transient surface temperature distribution, and a LePera etching is adopted to examine the microstructure after quenched surface. We explain the various and temporal boiling regimes, including the comparison of microstructure and mechanical properties.

# Chapter 2

## Experimental Apparatus and Arrangements

### 2.1 Flow system of Single/Two jet impingement

The experimental setup is schematically shown in Fig. 2.1, and the components are heat flux gauge, flow loop and data acquisition system (DAQ). The flow loop consists of water reservoir, pump, electromagnetic flowmeter, water chamber and the jet nozzle. The water coolant temperature is maintained with  $20^{\circ}\text{C}$  ( $\pm 0.5^{\circ}\text{C}$ ) with a constant-temperature reservoir composed of insulated stainless-steel tank of 700 L, electric heater of 10 kW, and chiller for water temperature control. The coolant of water can be delivered by a pump (CRN 1-15, Grundfos) which has nearly total head of 100 m. The water flow rate was directly measured by an electromagnetic flowmeter (GF630A/LF600, Toshiba). During the experiments, the water flow rate was consistently kept constant as determined from an electromagnetic flowmeter connected in the flow loop. The water chamber with jet nozzle is mounted 100 mm above the flat plate center with axisymmetric circular nozzle. The center of the nozzle is carefully aligned to the center of the heated flat plate with a laser pointed guide. The distance between the nozzle and the surface of the heated surface is fixed at 100 mm. The inner diameter of the nozzle is 3 mm and its length is 100 mm. The water flow rate is  $0.14\text{ m}^3/\text{hr}$ , corresponding to Reynolds number ( $Re_D$ ) of 15,000. The measurement uncertainty is within 0.7%, for the volumetric flow rate

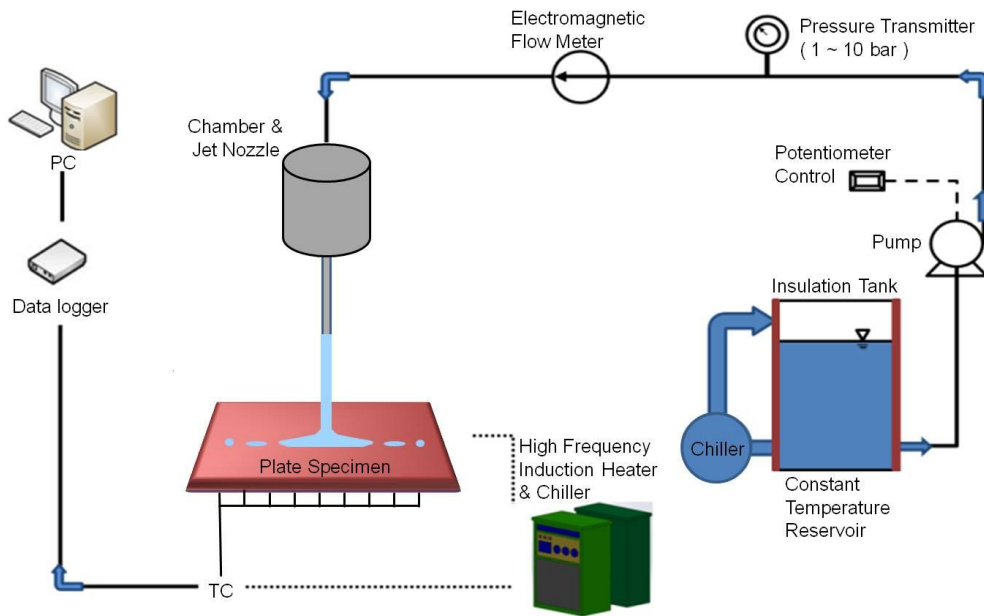


Figure 2.1 : Schematic of the jet quench boiling experiment and its components.

measurement. The test flat plate and its embedded thermocouples used as the high-temperature heat flux gauge are shown in Fig. 2.2. The test assembly consists of flat plate, induction heating system, porous ceramic insulators and the thermocouples.

An image of the heat flux gauge is shown in Fig. 2.2(a), and the plate is made of stainless-steel ANSI 304 which avoids phase-transformation heat generation encountered in most of carbon steels. The 304 stainless-steel is well known for its chemical inertness at elevated temperature and does not go through solid-solid phase transformation that can exert noticeable amount of heat and distract temperature reading during water quenching process. The flat plate is rectangular, length 300 mm, width 200 mm and thickness of 20 mm, with twenty two  $1 \pm 0.1$  mm diameter holes drilled accurately through electric discharge machining (EDM). 22 K-type thermocouples (KMTXL-040G-6, OMEGA®) with 1 mm thick are installed inside

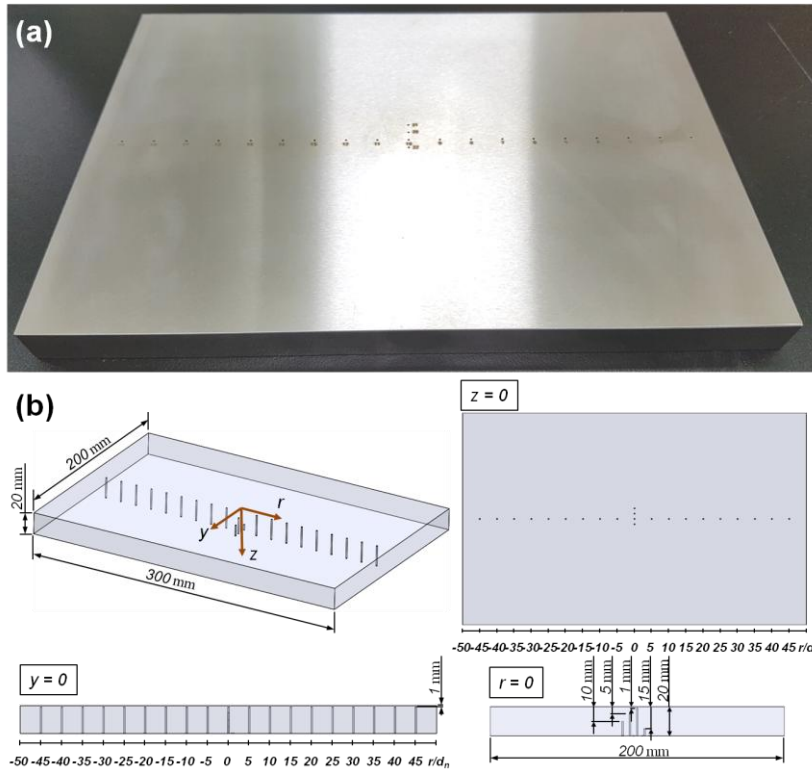


Figure 2.2 : (a) Image of the stainless steel plate and the locations of the thermocouples, (b) Schematic of the thermocouple-holes for measuring temperature.

the test flat plate as shown in Fig. 2.2(b). Nineteen holes have depth of 19 mm and are radially 15 mm apart. Three holes have depth of 5, 10 and 15 mm respectively and are located near the plate center.

The thermocouples are placed in these holes and precisely spot welded. A calibration on thermocouples is carefully performed with platinum resistance thermometer and the uncertainty of the thermocouples is found to be within  $0.1^{\circ}\text{C}$ . Temperature is measured and recorded with high-speed data acquisition system (EX1032A, VTI Instruments Co.) with sampling rate of 10 data/s. The side and bottom of the plate are thermally insulated with porous ceramic insulators.

Induction heating is used to heat the plate up to 900°C above austenite temperature. Induction heating suited for noncontact heating is applied using rectangular-shaped coil specially manufactured for uniform heating. The rectangular-shaped coil unit with tube diameter is 9.4 mm is placed above the plate. When high-frequency of 19 kHz current is applied to the coil, eddy current is generated on the surface of the plate by Faraday's law. So the joule heating is the product of electrical resistance of the material and square of the induced current. During the induction heating process, as the eddy current generation is uniformly distributed in the plate, and its temperature is maintains at 1,000°C within 5°C across the plate. By using the induction heating method, the plate electrically heated up to 1,000°C within 20 min. An ultra-high-definition (UHD) video camera is used to visualize the complex boiling phenomena on the heated flat plate during the water jet quenching. The UHD camera is also synchronized to the data acquisition system which is to measure temperatures inside the flat plate.

## 2.2 Experimental apparatus for 4-types of quenching method

Figure 2.3 shows a schematic and apparatus setup for water/oil immersion quenching methods. The highly heated specimen is vertically held and inserted into the isothermal bath by automatic pneumatic system. The different coolant mediums with  $20 \pm 0.5^\circ\text{C}$  are properly selected to control the cooling capacity as water or oil for 1<sup>st</sup> and 2<sup>nd</sup> quenching types, separately. The transparent windows with a size of  $200 \times 200 \text{ mm}^2$  are placed at both front and rear of isothermal bath to visualize the boiling phenomena on heated surface. The boiling behavior was visualized by the color high-speed CCD camera (Phantom® M320) with 1,000 frames per second. In order to shorten the cooling time of immersion method, 4 of stirrers are installed at each corner of isothermal bath to induce the dynamic flow around specimen. Each stirrer has maximum rotating speed of 3000 rpm and is controlled from 0 to 3000 rpm by watching the rpm meter.

Figure 2.4 shows a schematic of experimental setup of forced immersion (3<sup>rd</sup> type) and multiple jet quenching (4<sup>th</sup> type) methods. The flow loop mainly consists of the test section, flow loop, chamber and induction heating and data acquisition system. The water coolant temperature is maintained with  $20^\circ\text{C}$  ( $\pm 0.5^\circ\text{C}$ ) with a constant-temperature reservoir composed of insulated stainless-steel tank of 700 L, electric heater of 10 kW, and chiller for water temperature control. To deliver the coolant of water, six pumps (MGE132SC2-FF265-G3, Grundfos) are installed and the flow rate of each pump is directly measured by an electromagnetic flowmeter (OPTIFLUX2300, Krohne).

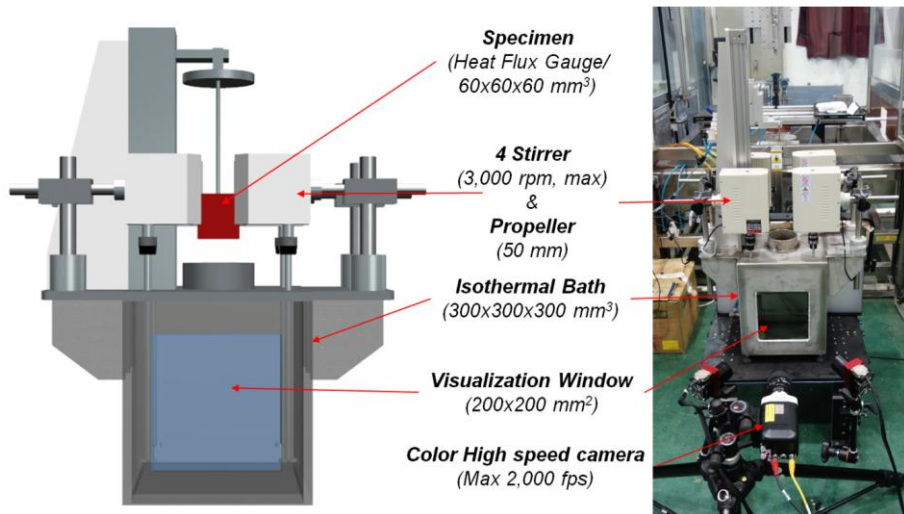


Figure 2.3: Schematic and experimental apparatus for water/oil immersion quenching methods(1<sup>st</sup> and 2<sup>nd</sup> types).

The water flow rate is consistently kept constant as determined from an electromagnetic flowmeter connected in the flow loop. The flow rate of each pump is designed to enable individual control from 0 to 25m<sup>3</sup>/hr. Fig. 2.5 shows installed experimental apparatus for 3<sup>rd</sup> and 4<sup>th</sup> quenching types which is designed to be able to perform two-stages of experiment in one system. During the forced immersion quenching, the water flows from 6 pumps line are integrated in one large pipe line and directly entered to the transparent quartz cylinder with the diameter of 101.6 mm. The total flow rate is adjusted as 60, 90, 120 m<sup>3</sup>/hr and falls down like as a waterfall to the upper part of specimen. In multiple jet quenching, six of multiple jets nozzle surround the six faces of cube shape specimen at top, 4 of lateral and bottom faces.

The test assembly consists of test block, induction heating system, porous ceramic insulators and the thermocouples. The image of test block and its embedded

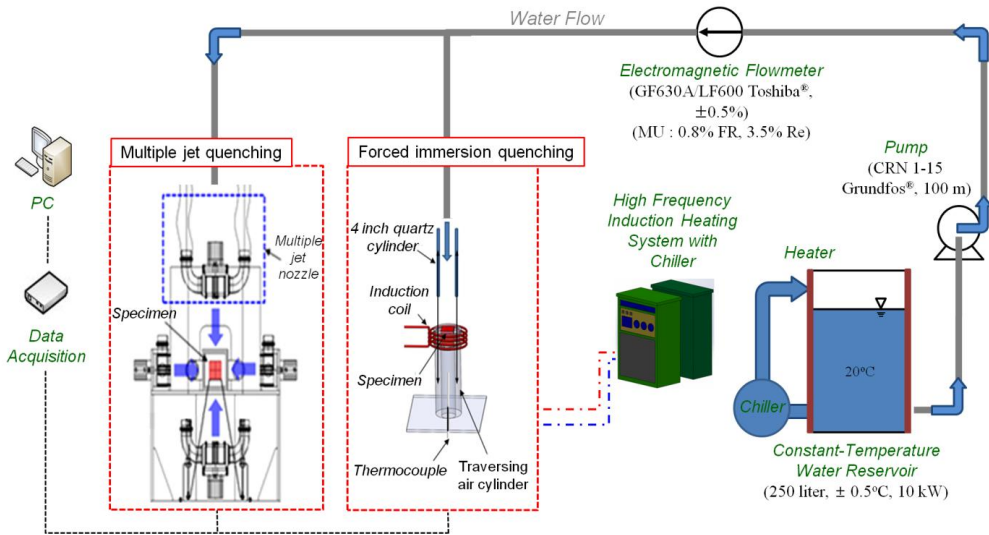


Figure 2.4 : Schematic of experimental setup of forced immersion(3<sup>rd</sup> type) and multiple jet quenching(4<sup>th</sup> type) methods.

thermocouples used as the high-temperature heat flux gauge are shown in Fig. 2.6. The test block is designed as a cube shape with the length of the edges equal to 60 mm and two of the steel materials are adopted for comparison. Fig. 2.6(a) shows the block is made for inverse heat transfer analysis by stainless-steel ANSI 310S which avoids phase-transformation heat generation encountered in most of carbon steels. The 310S stainless-steel is well known for its chemical inertness at elevated temperature and does not go through solid-solid phase transformation that can exert noticeable amount of heat and distract temperature reading during water quenching process. To evaluate the surface thermal characteristics, the total twenty-eight  $1\pm 0.1$  mm diameter holes drilled accurately through electric discharge machining (EDM). Twenty-two holes with depth of 59 mm and radially 5 mm apart are placed near the surface. Six holes have depth of 5, 15, 30, 45, 52 and 58 mm respectively and are

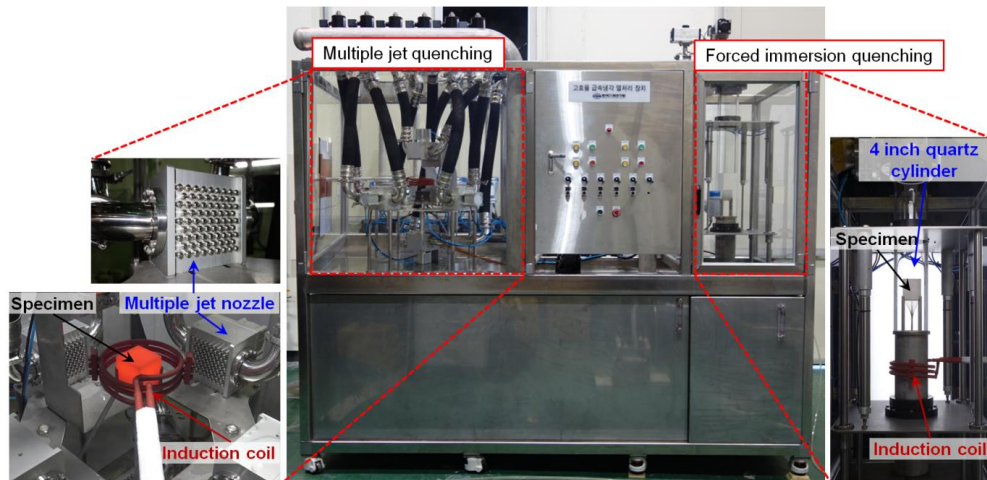
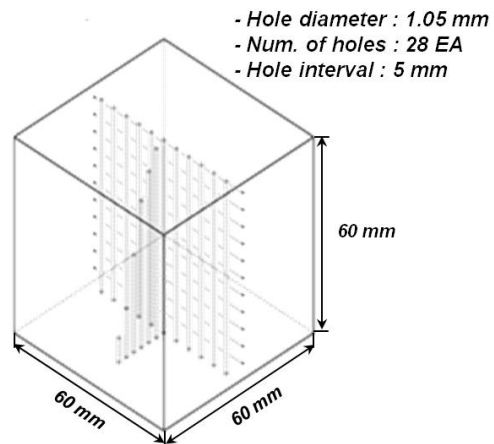


Figure 2.5: Experimental apparatus of forced immersion (3<sup>rd</sup> type) and multiple jet quenching (4<sup>th</sup> type) methods.

located near the center. Whereas, Fig. 2.6(b) is made of SNCM439 low alloy steel to compare the microstructure and mechanical properties after quenched surface. In order to ensure the necessary part on microstructure examination, only nine of holes are worked and three holes are arranged with hole interval of 15 mm for each surface(top, lateral and bottom). The K-type thermocouples (KMTXL-040G-6, OMEGA<sup>®</sup>) with 1 mm thick are placed in these holes and precisely spot welded. A calibration on thermocouples is carefully performed with platinum resistance thermometer and the uncertainty of the thermocouples is found to be within 0.1°C. Temperature is measured and recorded with high-speed data acquisition system (EX1032A, VTI Instruments Co.) with sampling rate of 10 data/sec. Induction heating is used to heat the specimen up to 900°C above austenite temperature.

Induction heating suited for noncontact heating is applied using rectangular-shaped coil specially manufactured for uniform heating. The cylinder-shaped coil unit with tube diameter of 13 mm is placed around the block. When high-frequency of 19 kHz

**(a) Stainless steel (SUS310S)**



**(b) Alloy steel (SNCM439)**

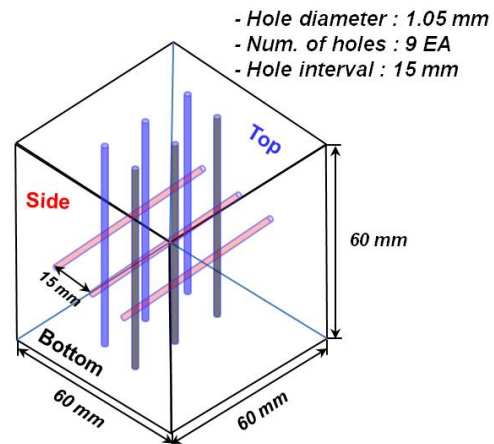


Figure 2.6: Image of steel block and schematic of the thermocouple-holes for measuring temperature for steel material of (a) stainless steel (SUS310S), (b) alloy steel (SNCM439).

current is applied to the coil, eddy current is generated on the surface of the plate by Faraday's law. So the joule heating is the product of electrical resistance of the material and square of the induced current. During the induction heating process, as the eddy current generation is uniformly distributed in the block, and its temperature is maintains at 1,000°C within 5°C across the block. The whole sides of the block

are thermally insulated with porous ceramic insulators and glass fiber. By using the induction heating method, the block electrically heated up to 1,000°C within 20 min.

## 2.3 Experimental Conditions of Study

Table 2.1 shows the arrangement of experimental conditions of present study for single/two interacting jets and 4-type of quenching methods. The main parameters of jet impingement are highlighted in thick character. The experimental condition of single jet impingement and two interacting jets are equal like as jet Reynolds number, initial/coolant temperature, number or position of hole and hole interval

Table 2.1 Arrangement of experimental configurations and conditions of present study.

Experiment	Quenching Configuration	Main variable	Range	$T_{ini}$ (°C)	$T_w$ (°C)	Number of hole	Interval size (mm)
Circular Subcooled-jet	Single jet	<b>Jet Reynolds number (Re)</b>	<b>15000</b>	900	20	23	15
Two interacting jets	Two jets	<b>Width of two interacting jets (<math>W/D_n</math>)</b>	<b>10, 20, 30</b>	900	20	23	15
Comparison of 4-type quenching method	Type-1 : Water Immersion	<b>Rotation speed of stirrer (rpm)</b>	<b>1000 - 3000</b>	900	15	28	5
	Type-2 : Oil Immersion	<b>Rotation speed of stirrer (rpm)</b>	<b>1000 - 3000</b>	900	15	28	5
	Type-3 : Forced immersion	<b>Total flow rate (<math>m^3/hr</math>)</b>	<b>60 - 120</b>	900	15	28	5
	Type-4 : Multiple Jet Quenching	<b>Total flow rate (<math>m^3/hr</math>)</b>	<b>60 - 120</b>	900	15	28	5

size only except for the number of jet. The jet Reynolds number for single/two interacting jet is set as 15,000. This is sufficient large value where there is no significant enhancement at larger Reynolds number.

For the 4-type of quenching method, conventional quenching method (Type 1&2), intensive quenching method (Type 3&4) are selected as comparison. The main variable of conventional quenching is rotation speed of stirrer, whereas the total flow rate is set as variable for intensive quenching methods.

## Chapter 3

# Estimate Thermal Boundary Condition and Microscopic Analysis

### 3.1 Inverse Heat Conduction Problem (IHCP)

#### 3.1.1 Overview of IHCP

When the thermal boundary conditions like as surface heat flux or surface temperature histories of specimen, the temperature distribution can be easily calculated by the simple direct problem. But, in many heat transfer treatment cases, the surface thermal boundary cannot be easily obtained for a precise experiment without interfering with the external flow of surface. So, the surface heat flux and temperature histories must be determined from transient temperature measurements at least one or more interior positions.

The inverse heat conduction problem (IHCP) have gained widespread acceptance in computer aided engineering (CAE), and we can access usual measurements only record some indirect aspect of the phenomenon. However, solving the IHCP is difficult because they are extremely sensitive to measurement errors and exact solution practically does not actually exist. Small measurement errors can be the source for unacceptable perturbations in the solution. Therefore, when solving an inverse problem the approximate methods like iterative procedures, regularization techniques, stochastic and system identification methods, combined techniques or straight numerical methods are needed to be properly used.

Above mentioned, the IHCP is a fundamentally ill-posed problem which does not have exact solution. The concept of well-posed or correctly posed problems was introduced by Hadamard. Assume that a problem is defined as

$$Au = g \quad (3.1)$$

where  $u \in U, g \in G, U$  and  $G$  are metric spaces and  $A$  is an operator so that  $AU \in G$ . In general  $u$  can be vectors that characterize a model of phenomenon and  $g$  can be the observed attribute of the phenomenon. To be established as a well-posed problem, the problem must meet the following requirements :

- the solution of equation (1) must exist for any  $g \in G$ ,
- the solution of equation (1) must be unique,
- the solution of equation (1) must be stable with respect to perturbation on the right hand side, i.e., the operator  $A^{-1}$  must be defined throughout the space  $G$  and be continuous.

If one of the above requirements is not fulfilled, the problem is termed as an ill-posed problem. For ill-posed problems the inverse operator  $A^{-1}$  is not continuous in its domain  $AU \in G$  which means that the solution of the equation (1) does not depend continuously on the input data  $g \in G$ . Generally, the solution of an ill-posed problem does not necessarily depend continuously on the measured data and the structure of the solution can have a tenuous link to the measured data.

In engineering field, the problems are defined as a boundary and initial conditions, shape and size of the domain, material properties of the media, governing partial

differential/integral equation and by internal sources and external forces or inputs. As mentioned, when all of information is known, the problem is of a direct type and generally considered as well posed and solvable. However, in the case of heat conduction problems, the governing equations and possible boundary and initial conditions have the following form :

$$\rho c \frac{\partial T}{\partial t} = \nabla \cdot (k \nabla T) + Q_v, (x, y, z) \in \Omega \subset R^3, t \in (0, t_f] \quad (3.2)$$

$$T(x, y, z, t) = T_b(x, y, z, t) \quad \text{for } (x, y, z, t) \in S_D, t \in (0, t_f] \quad (3.3)$$

$$-k \frac{\partial T(x, y, z, t)}{\partial n} = q_b(x, y, z, t) \quad \text{for } (x, y, z, t) \in S_n, t \in (0, t_f] \quad (3.4)$$

$$\begin{aligned} -k \frac{\partial T(x, y, z, t)}{\partial n} &= h[T(x, y, z, t) - T_\infty(x, y, z, t)] \\ &\text{for } (x, y, z, t) \in S_r, t \in (0, t_f] \end{aligned} \quad (3.5)$$

$$T(x, y, z, 0) = T_0(x, y, z, t) \quad \text{for } (x, y, z) \in \Omega \quad (3.6)$$

Where  $\nabla$  stands for gradient differential operator;  $\rho$  denotes density of mass, [ $\text{kg}/\text{m}^3$ ];  $c$  is the constant-volume specific heat, [ $\text{J}/\text{kg K}$ ];  $Q_v$  is the rate of heat generation per unit volume, [ $\text{W}/\text{m}^3$ ] and  $D$  for Dirichlet,  $N$  for Neumann and  $R$  for Robin boundary condition. The Eqs. (3.2) with conditions (3.3) to (3.6) describes an initial-boundary value problem for transient heat conduction.

The IHCP can be subdivided into the following categories: inverse conduction, inverse convection, inverse radiation and inverse phase change (melting or solidification) problems. In present study, boundary value determination inverse

problem is adopted to estimate surface thermal boundary condition based on the measured internal temperature histories. In this kind of IHCP on a part of a boundary the condition is not known. Instead, in some internal position of the quenched specimen some results of temperature measurements or anticipated values of temperature or heat flux are prescribed. The measured values by inserted thermocouples are called internal responses. They can be known on a line or surface inside the considered body or in a discrete set of points. If the internal responses are known as values of heat flux, on a part of the boundary a temperature has to be known, i.e., Dirichlet or Robin condition has to be prescribed. The more specific calculation for 2D domain for present study is described next section.

### 3.1.2 Algorithm/Calculation of IHCP

To quantify the boiling heat transfer characteristics, the surface thermal characteristics such as temperature and heat flux are required and without disturbing the jet flow on the surface, we adopt the numerical method of estimating the local heat transfer characteristics using the plate internal temperature distribution (from thermocouples). The inverse heat conduction method of Twomey [53] and Beck et al. [54] is used and the flow chart is shown in Fig. 3.1 for obtaining the axisymmetric temperature distribution. The measured data is converted and imported into the calculation nodes of axisymmetric IHCP domain with the initial temperature known.

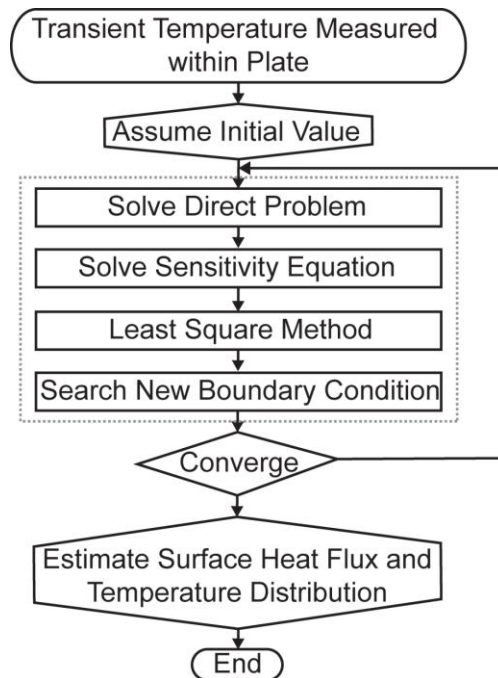


Figure 3.1 : Flow chart of 2-D inverse heat conduction problem for determining the transient surface temperature and heat flux distributions.

The unknown temperature at each position is calculated by interpolation. The unknown boundary condition (heat flux) is initially assumed and the temperature distribution is updated using the calculated temperature by the direct problem. In direct problem, the information of assumed boundary condition feeds into the temperature distribution. Because the IHCP is extremely sensitive to the measurement errors, the concept of sensitivity coefficient ( $\zeta$ ) is adopted to improve the experimental design. The sensitivity coefficient is defined as the first derivative of a dependent variable, such as the temperature, with respect to the unknown heat flux. The mathematic formulation of the sensitivity coefficient is expressed as

$$\begin{aligned} \delta T_{k,i}(r, z, t) &= \delta T_{k,i}^*(r, z, t) + \left. \frac{\partial T_{k,i}^*(r, z, t)}{\partial q_k} \right|_{q_k=q_k^*} (q_k - q_k^*) + \dots \\ &\approx \delta T_{k,i}^*(r, z, t) + \zeta_{k,i} (q_k - q_k^*) \end{aligned} \quad (3.7)$$

Where \* indicates former time iteration and subscripts  $k$ , and  $i$  presents the time and position. The calculated data is applied to sum of the squared functions ( $\Sigma$ ) to search for an optimal boundary condition by minimizing the  $\Sigma$ . The difference between measured and calculated temperature is

$$\Sigma = \sum_{i=1}^N [T_{k,i}^m(r, z, t) - T_{k,i}^c(r, z, t)] \quad (3.8)$$

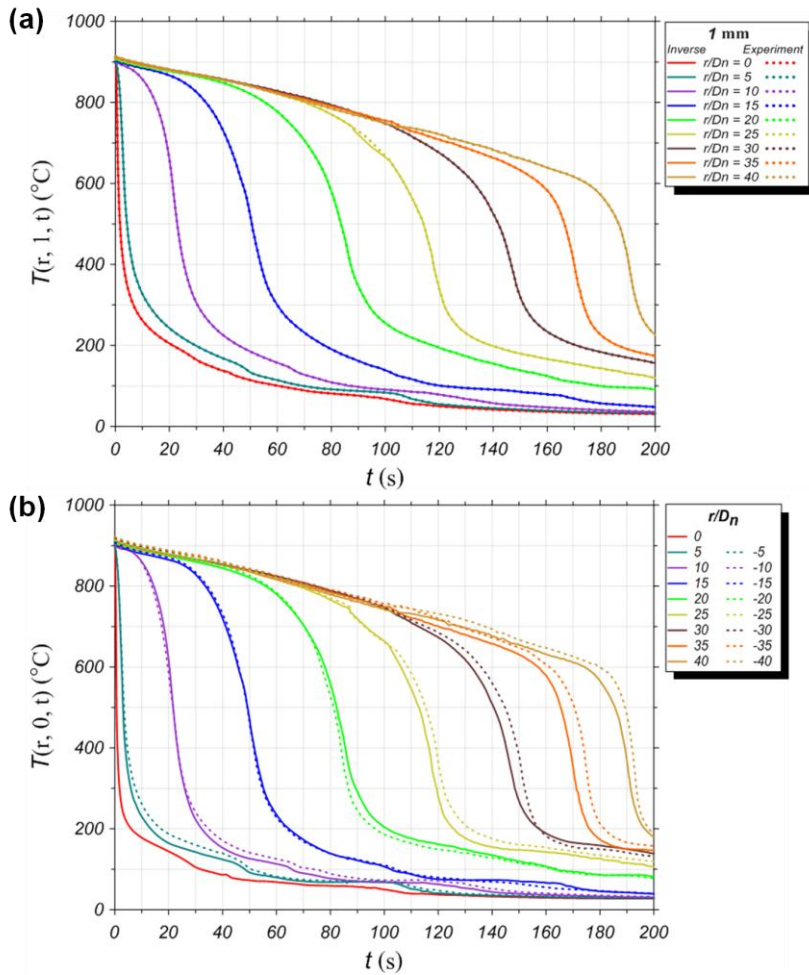


Figure 3.2 : Comparison between the measured and predicted (inverse heat conduction) plate temperature distributions at several radial locations: (a) 1 mm below surface and (b) at surface.

where  $N$  is the total number of measurement points. The comparison of measured temperature ( $T^m$ ) at 1 mm from the surface and calculated temperature ( $T^c$ ) at the surface are shown in Figs. 3.2(a)-(b). The dotted lines represent the measured temperature and the solid lines denote the calculated temperature from the IHCP. The graphs show good agreement, with a maximum error less than 4%.

### 3.1.3 Evaluation of Heat Transfer Coefficient

The estimation of the heat transfer coefficient ( $h$ ) from transient temperature measurements has aspects of both the inverse heat conduction problem and parameter estimation. The definition of the heat transfer coefficient can be obtained by estimated value by IHCP of surface temperature ( $T_{sur}$ ) and surface heat flux ( $q$ ) with a local adiabatic wall temperature ( $T_{aw}$ ).

$$h_n = \frac{q_n^c}{T_{aw} - 0.5(T_{sur,n}^c + T_{sur,n-1}^c)} \quad (3.9)$$

Where  $T_{sur,n}^c$  is an estimated temperature at time ( $t_n$ ) and  $h_n$  is usually more accurately evaluated at  $t_{n-1/2}$ .

The experimental heat transfer coefficient and the adiabatic wall temperature ( $T_{aw}$ ) results are presented in terms of the local Nusselt number. The local Nusselt number was therefore calculated with heat flux due to fluid conduction through the layer,

$$Nu = \frac{h_n D}{k} \quad (3.10)$$

Where  $D$  is the nozzle exit diameter defined as the hydraulic diameter and  $k$  is the thermal conductivity. The local Nusselt number distribution can be averaged to obtain an average Nusselt number which was defined as,

$$\overline{Nu} = \frac{\overline{h}_n D}{k} = \frac{D}{k} \int_n h_n \frac{(T_{sur,n}^c - T_{aw}) dA}{A \overline{\Delta T}} \quad (3.11)$$

### **3.2 Microscopic Analysis of Quenched Surface**

In the analysis of steel microstructures, the phases which need to be discriminated and quantified will be austenite and its transformation products. The latter includes the three major phases of ferrite, bainite and martensite according to transformation temperature and mechanism. Each of them also has a few sub-classes of characteristic morphology and crystallography. These diverse microstructures from austenite decomposition make the phase analysis of steels the most complicated among modern engineering alloys. In this study, it was aimed to evaluate the portion of martensite structure of after quenched surface along with their associated mechanical properties (harness, elongation). The surface morphology after each quenching method is observed by SEM and mechanical properties test. The quenched surface is etched by LePera etching(4% Picric acid, 1% Sodium metabisulfite) solution with 32 s, and etched surface shows different colors according to phases. Ferrite is known to appear as brown, martensite and retained austenite as white, bainite as black [55-58]. The baitnite volume fraction is optically measured using a Leopard image analyzer based on ASTM E112(E1382). In this paper, the martensitic volume fraction was expressed as the fraction of light gray area. Although the light gray area actually included retained austenite, its fraction of quenched steel can be negligible in most cases. The hardness profile is analyzed after removing 200  $\mu\text{m}$  of decarburized layer and examined up to 10 mm from surface with 0.05 mm interval. Samples prepared for optical metallography were examined in a Shimadzu HMV-2000 microindentation hardness tester. Hardness of

the after quenched surface was measured in the depth direction. Moreover, elongation test are also performed to investigate the cooling uniformity of the surface.

# Chapter 4

## Experimental Results and Discussion

### 4.1 Quasi-steady Front in Quench Subcooled-jet Impingement Boiling

#### *4.1.1 Flow Visualization and Cooling Regions*

Figure 4.1 shows sequence of images of jet quench boiling and during early stage (short elapsed time), Figs. 4.1(a)-(d), the cooled region (black) grows as a circular around the stagnation point. There is also droplet ejection which is ejected at the wetting front. In Fig. 4.1(d) there are three distinct regions, namely, wetted, wetting front, and dry region and these are also shown in Fig. 4.2(a). The covered the black spot area and its inner portion is single-phase convection while the outer portion is subcooled (collapsed bubble) boiling. In the dry region, the ejected droplets land (impinge) and evaporate under high surface superheat (Leidenfrost effect). The droplet hovers over the surface without physical contact and quickly ejected to outside of the specimen. The wetting front region is defined as the intermediate part between the wetted region and dry region. With increase in elapsed time in Figs. 4.1(e)-(i), the radius of black region grows but the front speed decreases due to the area expansion and there appears to be a hydraulic jump is formed as seen in Fig. 4.2(b). This radius of hydraulic jump depends on the initial jet flow velocity and the surface roughness which occurs when water flow is hindered. As shown in the Figs. 4.1(e)-(i), the wetting front region becomes larger with violent

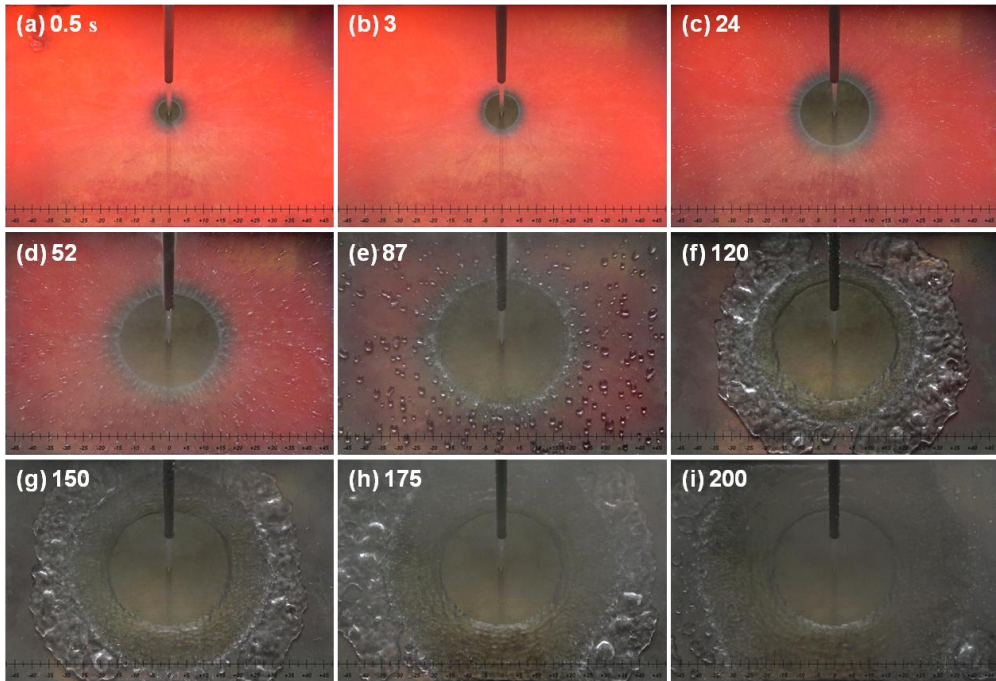


Figure 4.1 : Snapshot images of spreading jet, for several elapsed times, showing the wetting front, liquid eject (droplets), and eventual cooling of the plate (fading out red color). The progressively increasing central single-phase and the collapsed-bubble regions are also observed. The radial location is shown at the bottom of each snapshot.

boiling. But, it should be noted that the surface of wetting front region remained unwetted like as the film boiling in pool boiling.

Above-mentioned visualization results are well synchronized with a quantitative analysis of IHCP result. Figure 3.1(b) shows the transient temperature distribution at various radial locations along elapsed time. The slope of each graph closely associates with the local boiling regime at specific time. The temperature distribution of  $r/D_n = 0$  shows rapid gradient in early time ( $<0.8$  s), and, after that, its slope becomes gradual and almost flat after 60 sec. Since the coolant directly

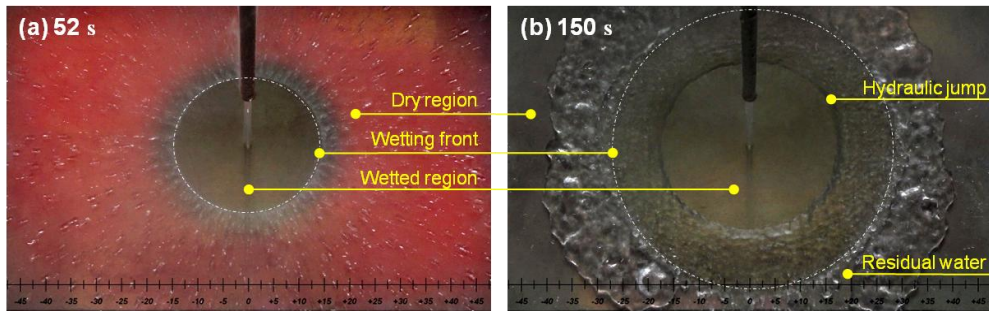


Figure 4.2: Snapshot image comparison at two elapsed times, with marking of the various regions. (a) Plate has significant superheat, and (b) plate is significantly cooled with large subcooled single-phase inner region. The spread of the wetting front is linear with time. The fraction liquid eject from the front remains constant with time, but the front perimeter increases so the droplet are more spread.

impinges on the stagnation point, the surface is wetted in very short time and the nucleate boiling immediately occurs [39-40]. Therefore, the film boiling regime could not be observed in the graph of  $r/D_n = 0, \pm 5$ . The nucleate boiling results in the sharp temperature drop but disappears going through the transition boiling. After that, the single-phase convection accompanying gradual temperature drop is followed. Comparing to the slopes of  $r/D_n = 0$  and  $\pm 5$ , the temperature profile of outside zone ( $\pm 10 \leq r/D_n \leq \pm 40$ ) shows three steps: a slow grade in early stage, a steep grade in middle stage and a modest gradient until final stage. Each step of slope is categorized as a film boiling, a nucleate boiling and single-phase convection, respectively.

The specific boiling regimes are specified in more detail with the local heat flux distribution at various radial locations against the local surface superheat of Fig. 4.3. The heat flux distribution shows almost zero at beginning stage in the Fig. 4.3(a).

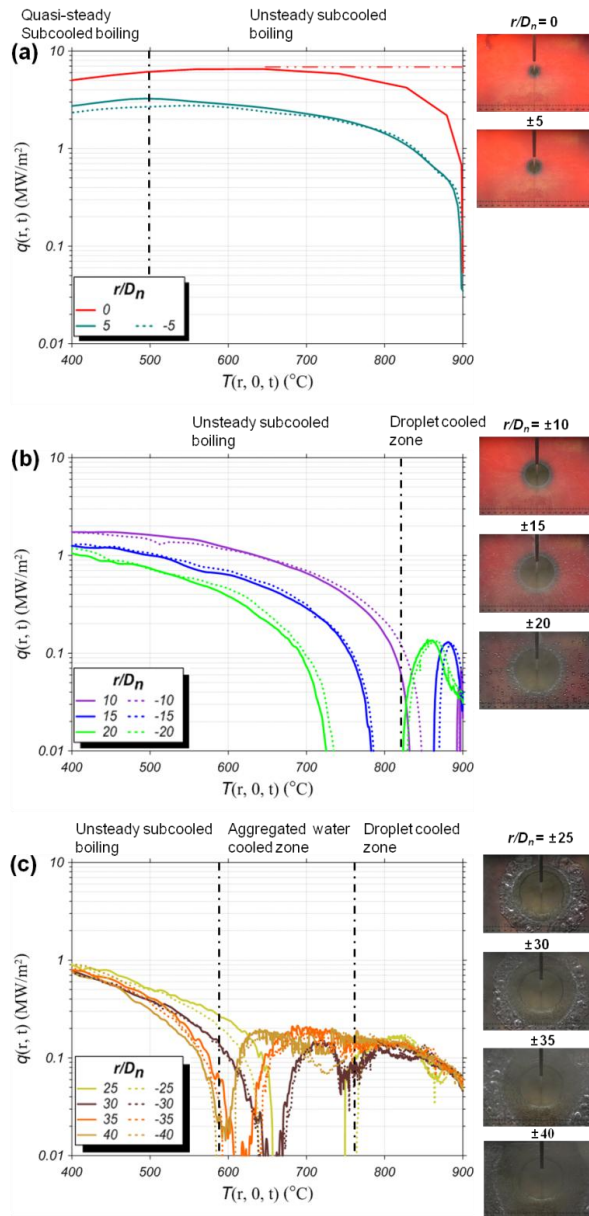


Figure 4.3 : Variations of the transient local surface flux with respect to local surface superheat at various radial locations: (a) inner, (b) middle, and (c) outer regions.

Note that two set of data are shown for each radial location (one each side) to confirm presence of symmetry. The inner region is least affected by cooling with the ejected droplets, so has experiences rather steady cooling, while the outer region is substantially cooled by droplets before the front arrives.

But Karwa et al.[38] and Akmal et al. [59] suggested that the time response of the thermocouple can lead the additional delay on the time required to reach the maximum heat flux ( $q_{\max}$ ). Considering the limitation of measurement technique, we can assume that the  $q_{\max}$  of the  $r/D_n = 0$  appears almost at the initial jet impingement quench as marked with dotted red line. Whereas one of  $q_{\max}$  appears in Fig. 4.3(a), the Fig. 4.3(b) and (c) show two and three of peaks, separately. Each of peak value is originated from the distinct boiling heat transfer regime. The sole peak in radial position of  $r/D_n = 0, \pm 5$  in Fig. 4.3(a) shows high value of  $q_{\max}$  that reaches 6.4 and 3.2 MW/m<sup>2</sup>. The temperature where the nucleate boiling occurs relates with the value of  $q_{\max}$ . These high values come from the nucleate boiling occurs in short time right after jet impingement. On the other hand, the first peak in radial position of  $r/D_n = \pm 10, \pm 15$  and  $\pm 20$  is originated from the air and droplet cooling. When the radius of wetting area is smaller than each of radial position, the surface is unwetted and the surface temperature is gradually decrease until 850°C as shown in Fig. 3.1(b). After the surface wetting, the nucleate boiling regime starts with heat flux increasing and shows the second maximum peak with  $q_{\max}$ . The value of  $q_{\max}$  of Fig. 4.3(b) is smaller than that in Fig. 4.3(a) due to the lower starting temperature of nucleate boiling. The more outer radial position of  $r/D_n = \pm 25, \pm 30, \pm 35$  and  $\pm 40$  shows three bends of curves. Like as Fig. 4.3(b), the first curve located in right side comes from the air and droplet cooling, and the third curve in left side presents the nucleate and transition boiling regime. The second curve in middle part is caused by the residual water at wetting front region. Figure 4.4 shows local heat flux at  $r/D_n = \pm 30, \pm 40$  with respect to the surface temperature and elapsed time, separately, shows

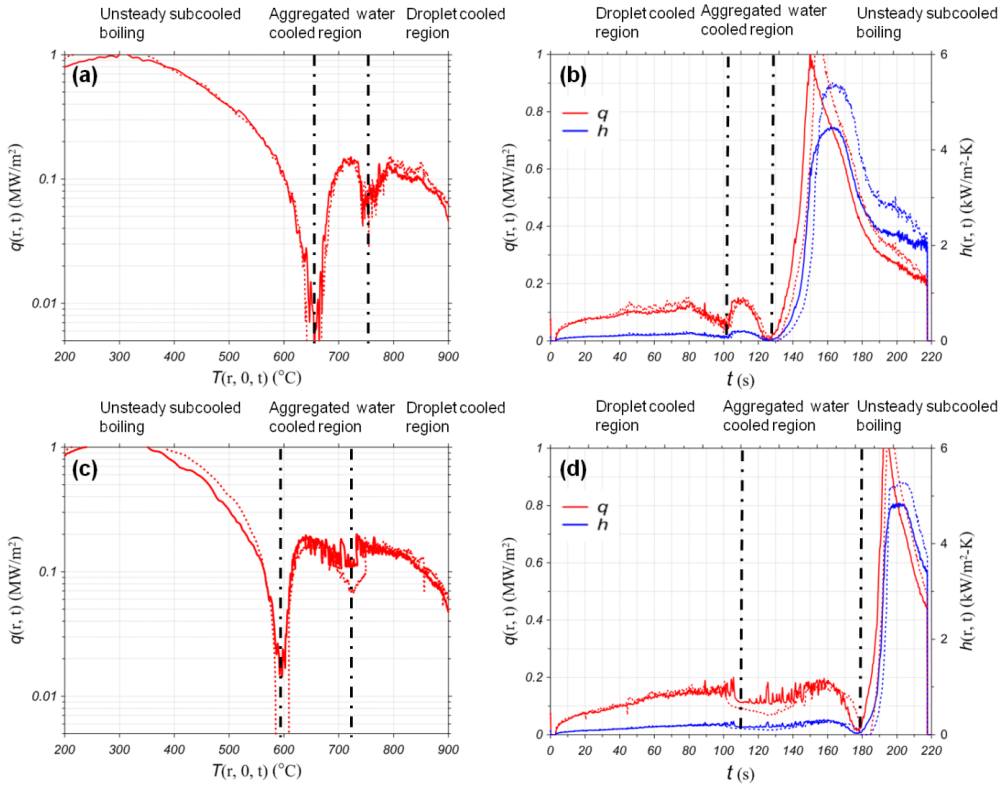


Figure 4.4 : (a) Variations of local surface heat flux distribution with respect to the local surface superheat and (b) variations of the local surface heat flux and heat transfer coefficient with respect to time, at locations  $r/D_n = \pm 30$ . (c) and (d), same but for  $r/D_n = \pm 40$ . Various cooling regime encountered are also shown.

the boiling phenomenon of second curve more specifically. The starting temperature and time of second curve of  $r/D_n = \pm 30$  in Fig. 4.4(a) is relatively higher than that of  $r/D_n = \pm 40$  in Fig. 4.4 (c). It is due to the outer side is cooled in more time with droplet cooling. After starting residual water cooling, Fig. 4.4(b) is for larger elapsed time compared to Fig. 4.4(d). The residual water with stagnant flow motion causes the film boiling phenomenon in pool boiling and the magnitude of heat flux in wetting front region is almost same with the droplet cooling in wetting region. This

confirms nucleate boiling does not occur at the wetting front.

### 4.1.2 Quasi-steady Regime

Figures 4.5 and 4.6 show the synchronization of boiling visualization with the surface temperature, heat flux and heat transfer coefficient along the wetting radius with specific time. The orange colored vertical means the position of  $q_{\max}$  calculated by IHCP at specific time. At the start of quenching in Fig. 4.5(a), the  $q_{\max}$  and maximum heat transfer coefficient locates at the stagnation point. And the starting temperature of nucleate boiling is almost same with the initial temperature of 900°C. It confirms again that the film boiling does not occur at the stagnation point. At the wetting radius of  $R_{\text{do}}/D_n = \pm 5$  in Fig. 4.5(b), the temperature at the stagnation point decreases near 250°C and shows sharp gradient along radial position. The nucleate boiling site with  $q_{\max}$  positions at the inner of wetting radius has relatively low value than that of Fig. 4.5(a). After that, the  $q_{\max}$  position of Figs. 4.5(c) and (d) shows almost accords with the boundary of wetted region. This result indicates that the nucleate boiling occurs in very early time where the jet flow is directly impinged. But after the short time, the surface wetting is the key of distinguishing the position of nucleate boiling site. This tendency is continuously observed in more elapsed time of Fig. 4.6. In Figs. 11(a)-(c), the position of  $q_{\max}$  is completely identical with the wetting radius. But at the outer radial position of  $R_{\text{do}}/D_n = \pm 35$  in Fig. 4.6(d), the nucleate boiling with  $q_{\max}$  locates slightly out boundary of wetted region. It can be regarded as due to the long duration of residual water cooling. Moreover, it is also confirmed again that the nucleate boiling temperature which is overlapped with vertical line decreases and the magnitude of  $q_{\max}$  decreases with the same rate.

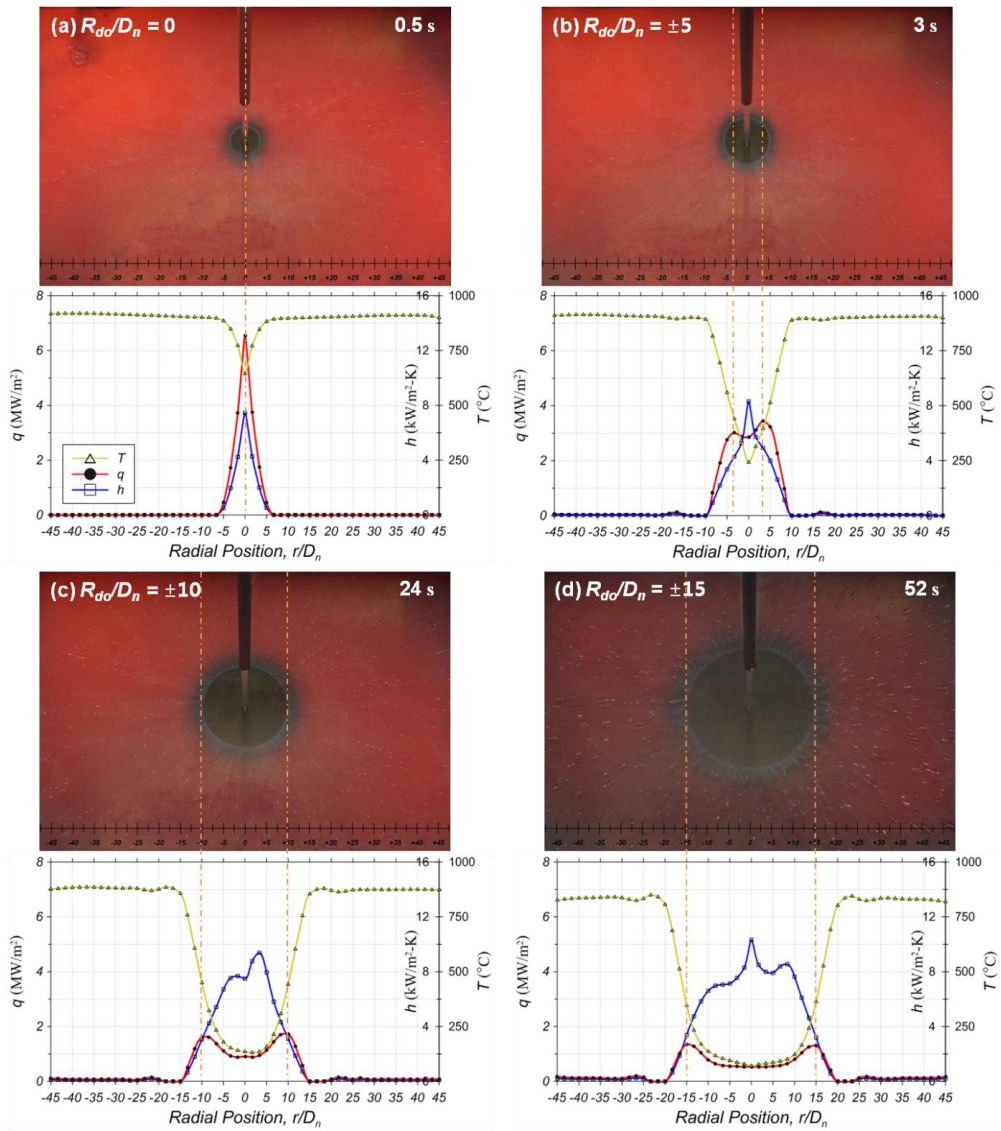


Figure 4.5 : Snapshot image combined with the radial distributions of the surface heat flux and heat transfer coefficient at wetting front radii  $R_{d0}/D_n$  (a)  $\pm 0$ , (b)  $\pm 5$ , (c)  $\pm 10$ , and (d)  $\pm 15$ . The elapsed time is chosen accordingly to reveal the regimes.

However the decrease of  $q_{\max}$  over time becomes rapidly smaller after the specific time of  $24$  s as shown in Fig. 4.5(c). From above-results, it can be seen that the distinct tendency comes to existence from the comparison of boiling visualization

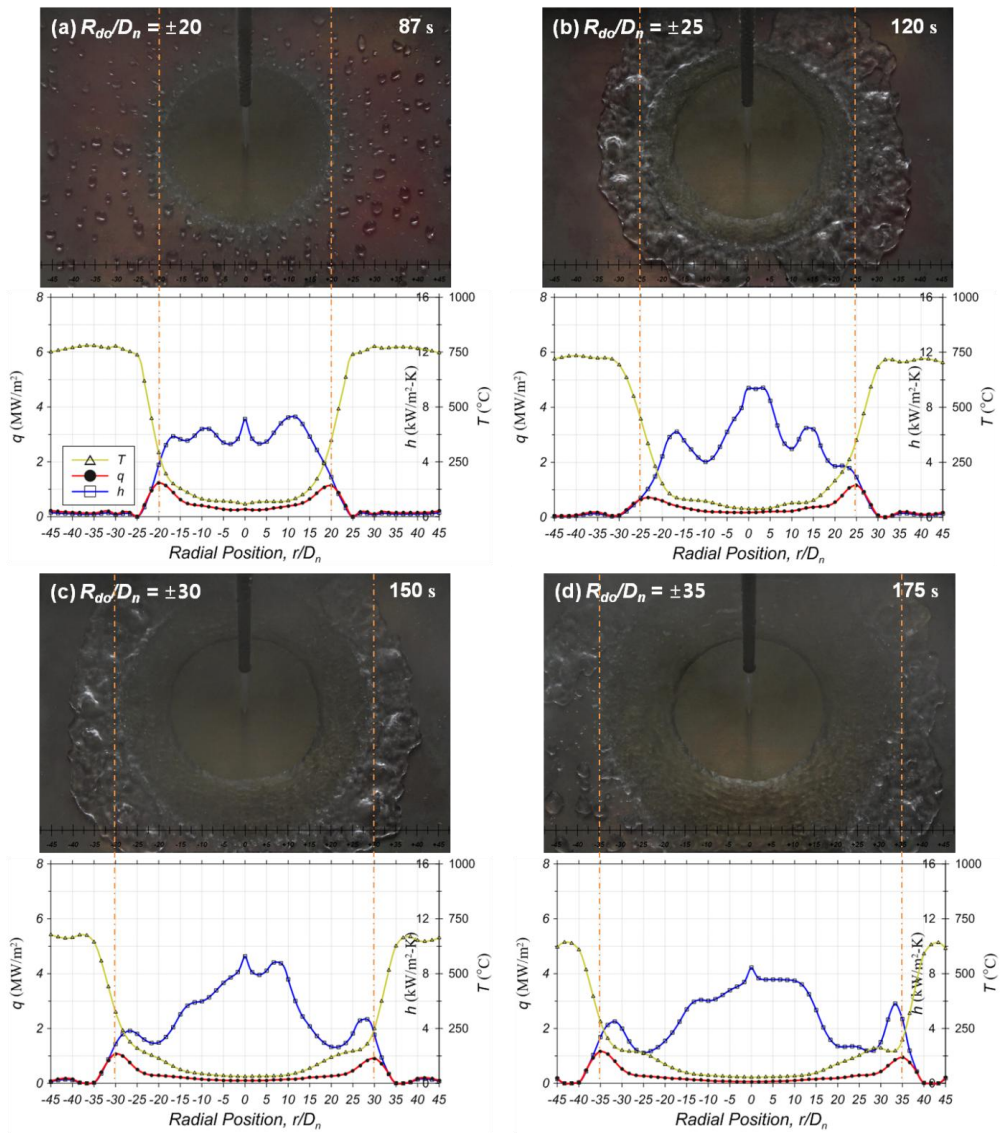


Figure 4.6 : Same as Figure 4.5, but for  $R_{do}/D_n$  (a)  $\pm 20$ , (b)  $\pm 25$ , (c)  $\pm 30$ , and (d)  $\pm 35$ .

The elapsed time is also chosen accordingly to reveal the regimes.

with thermal distribution data by IHCP.

From above-results, it can be seen that the distinct tendency comes to existence from the comparison of boiling visualization with thermal distribution data by IHCP. After a specific time, the position of  $q_{\max}$  is approximately identical to that of

wetting radius. We assume that not only the temperature distribution of surface but also the inner temperature of specimen can associate with the boiling phenomenon. Figure 4.7 shows the sequence of inner temperature contour sliced at stagnation point. The  $(r,z)=(0,0)$  point denotes the stagnation point. As the boiling heat transfer occurs at surface, the conduction heat transfer in depth direction occurs at the same time. The heat transfer rate going through the top surface is composed of complex interaction between the internal energy of surface and the conduction heat transfer from inside of specimen. Therefore, the thickness of specimen and thermal properties for conduction are deeply involved with the duration time of boiling heat transfer mode. As the thickness of specimen is thicker, the duration of each boiling mode can be longer. As shown in Fig. 4.7(c), the cooling of bottom surface starts in progress at 24 s. After that, the synchronization results of Figs. 4.5 and 4.6 show distinct quasi-steady characteristics like as the position of  $q_{\max}$  and its value, and which time means the quasi-steady time ( $\tau_{qs}$ ).

### 4.1.3 Wetting Front Propagation

Figure 4.8 shows the 3-D graph of surface heat transfer characteristic with surface heat flux, temperature and elapsed time. The difference of  $q_{\max}$  at  $r/D_n = 0$  and 5 before the quasi-steady time shows larger value, but that of after the quasi-steady time shows very little change. This might be explained by two possible causes. First, the overall temperature of surface decreases as the time passes. The  $q_{\max}$  highly relates with the starting temperature of nucleate boiling. But the nucleate boiling at a radially outward position occurs at lower starting temperature as mentioned previous section. Second, the temperature gradient at outward position in depth direction becomes larger as time passes as shown in Figs. 4.7(d)-(i). The larger temperature gradient causes larger conduction heat transfer rate in depth direction. As a result, the low starting temperature of nucleate boiling can lower the heat transfer rate, but the conduction heat transfer in depth direction is relatively high at the outward position. Therefore, the  $q_{\max}$  at several outward positions can be remained in similar value.

The quasi-steady regime is well presented in the graph of Fig. 4.9 which shows the radius of wetting front and position of  $q_{\max}$  against the elapsed time. In early stage before the quasi-steady time, the radius of wetting front shows exponential increase and the  $q_{\max}$  occurs inside of wetted region. After the time  $\tau_{qs}$ , the both lines shows the linear increase and a good agreement between the radius of wetting front and position of  $q_{\max}$ . These results are already visually and quantitatively verified in Figs. 4.5 and 4.6.

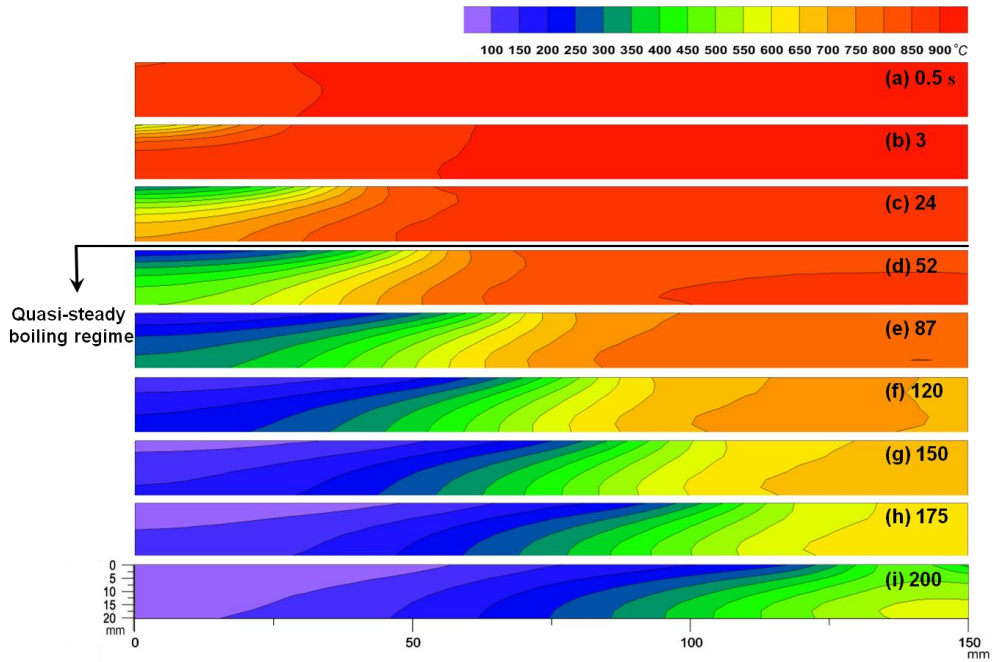


Figure 4.7 : Variations of the inverse-conduction predicted temperature distribution within the plate at several elapsed times. The onset of the quasi-steady behavior is marked by the quasi-steady time reaching the back of the plate.

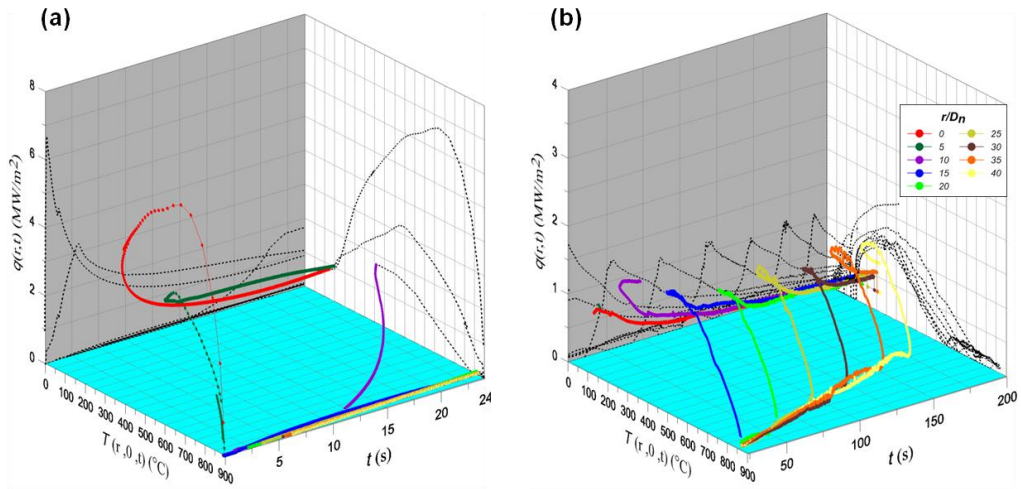


Figure 4.8 : Three-dimensional presentation of the simultaneous variations of the surface heat flux, surface temperature, and the elapsed time of (a) 0~24 (i.e.,  $\tau_{qs}$ ), and (b) 24~200 s, at several radial locations. The quasi-steady regime is noted with a similarity of the cooling behavior at various locations.

#### 4.1.4 Fraction of Liquid Ejected at Propagating Front

In addition to the single-phase and subcooled boiling heat transfer, the droplets ejected at the front land on in the otherwise region and evaporate, resulting in significant cooling in that region. The fraction of liquid ejected is estimated as the evaporation fraction ( $\beta$ ). The local (discrete locations) surface heat flux  $\langle q \rangle_i$  from the axisymmetric inverse heat conduction analysis is used to obtain the total, instantaneous heat flow rate

$$Q = \sum_{i=1}^n \pi (R_{i+1}^2 - R_i^2) \langle q \rangle_i \quad (4.1)$$

where  $n$  is the number of surface segment sections and  $R_i$  is their radial locations from the center. The water jet flow is assumed to reach saturation temperature before ejection, so the fraction of liquid ejected and undergoing phase change can expressed as the following equations,

$$\sum_{i=1}^n \pi (R_{i+1}^2 - R_i^2) \langle q \rangle_i = \beta \rho_l \pi \frac{D_n^2}{4} u_n \Delta h_{lg} \quad (4.2)$$

$$\therefore \beta = \frac{\sum_{i=1}^n \pi (R_{i+1}^2 - R_i^2) \langle q \rangle_i}{\rho_l \pi \frac{D_n^2}{4} u_n \Delta h_{lg}}$$

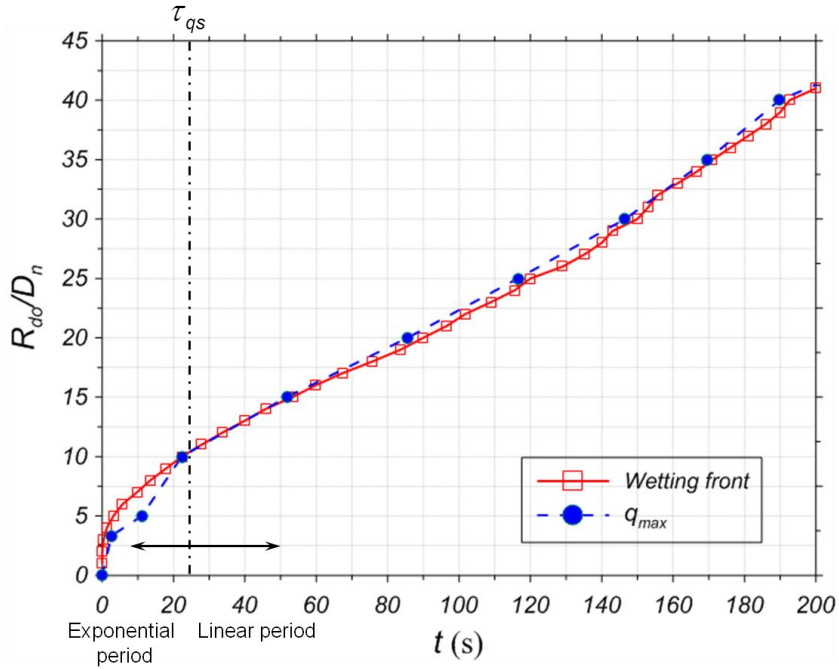


Figure 4.9: Variation of the wetting front location with respect time, showing the quasi-steady regime where  $R_{do}$  increases linearly with time. The position of the maximum heat flux at specific time is also marked.

If we neglect evaporation at the wetting front, this would be the fraction of the ejected front (so it is rather overestimated). Figure 4.10(a) shows the fraction of liquid undergoing phase change  $\beta$  as a function of the elapse time. Once the quasi-steady state is reached  $\tau_{qs}$ , this fraction shows the linear shapes of graph. And the fraction of liquid  $\beta$  also shows the linear increase along the radial position and reaches over 10% of the liquid flowing out the nozzle as shown in Fig. 4.10(b). These ejected droplets land on the otherwise dry region and turn to be evaporated.

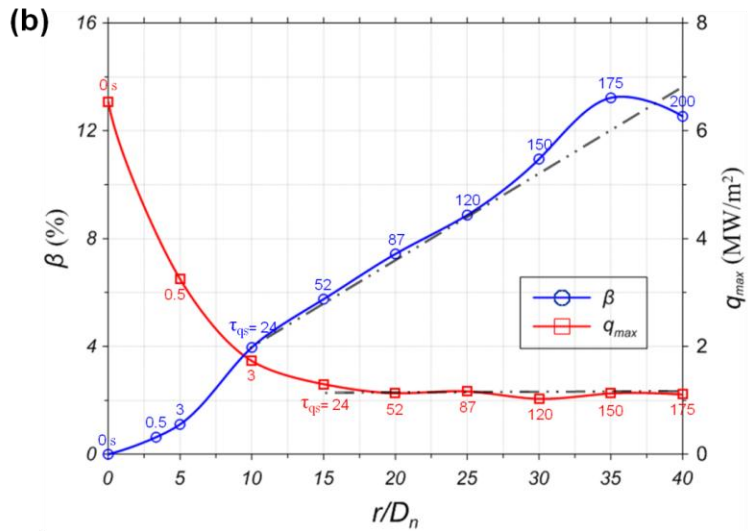
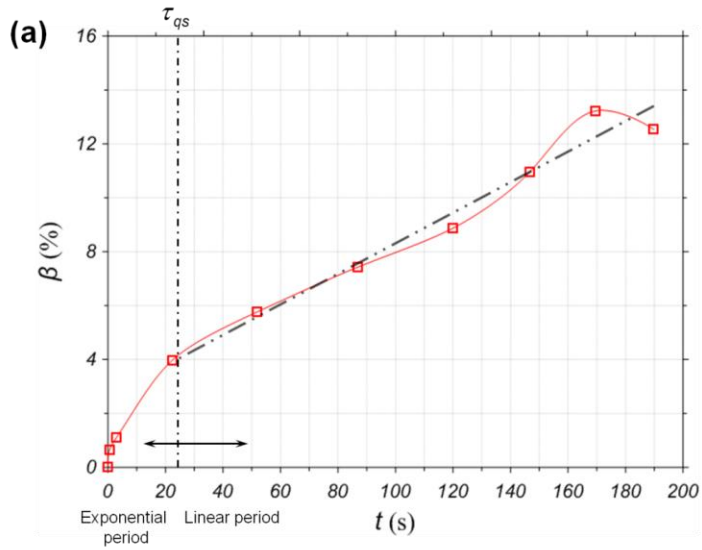


Figure 4.10 : (a) Variations of the fraction of liquid ejected at wetting front and evaporating as droplets in the dry region against the elapsed time and (b) variations of the fraction of liquid ejected at wetting front with the value of maximum heat flux along the radial position.

## 4.2 Effect of Two Interacting Jets on Boiling Heat Transfer

### 4.2.1 Flow Visualization and Cooling Regions

In previous section, the boiling heat transfer mechanism of single jet impingement is thoroughly investigated. In this section, two interacting jets is adopted and following experimental results explored by comparing that result of single jet impingement. Fig. 4.11 shows the schematic of two interacting jets impinge over a superheated surface of plate. Each jet impinged over the stagnation point spreads on along the radial direction. At the middle part of two jets, the distinct flow interaction is observed on the center of plate because the radial jet flow of each jet meets and aggregated. This flow interaction affects the local boiling heat transfer and show distinct cooling performance. Whereas, the flow of outside of two jets is almost same with the single jet flow accompanying three distinct cooling regions.

The intensity of interacting flow usually depends on the jet Reynolds number and the width of two jets. In this study, we set the spacing of two jets as a main parameter and the flow visualization is firstly explored with high speed camera and 4K high resolution video camera without boiling heat transfer as shown in Fig. 4.12.

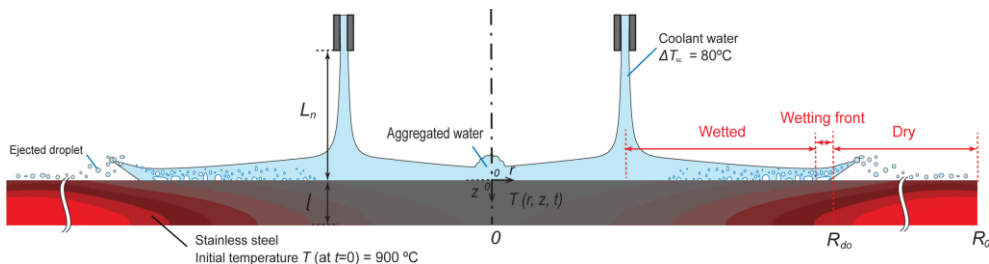


Figure 4.11 : Schematic of two interacting water circular jets over a superheated horizontal plate.

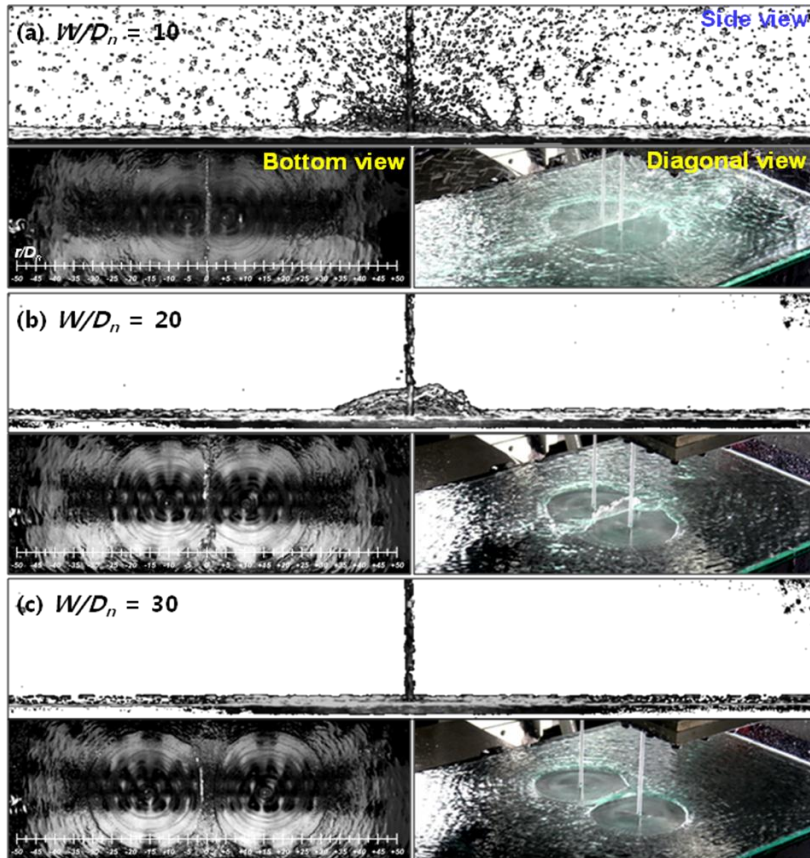


Figure 4.12 : Flow visualization of two interacting jets along with different width per nozzle diameter ( $W/D_n$ ) of (a) 10 , (b) 20 , (c) 30.

Above mentioned, the shape of interacting flow of Fig. 4.12 at fixed jet Reynolds number only depends on the width per nozzle diameter ( $W/D_n$ ). The gathering flow shows different intensity along with width of two jets, and as the width becomes closure, numerous of droplets are observed and popped up from the interacting flow. These numerous droplets can affect the mechanism of cooling by dropping on the dry region of superheated surface. And also, the volume loss of water occurs as the droplets popped and leaved the plate.

The Fig. 4.13 shows the snapshot image of boiling visualization of  $W/D_n = 30$  at

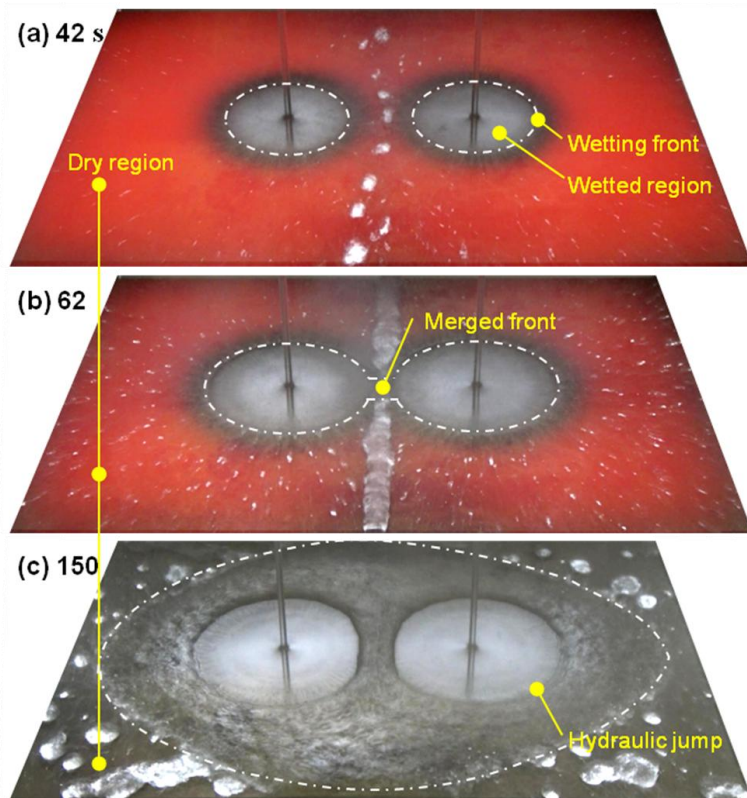


Figure 4.13 : Snapshot images of boiling visualization of  $W/D_n = 30$  at three elapsed times. The inner part of two jets wets faster than that of outside part.

three elapsed times. The surface wetting shows axisymmetric, and there are three distinct regions, namely, wetted, wetting front, and dry region in the Fig. 4.13(a). Note that the wetting of inner part of two jets becomes different with that of outside part due to the flow interaction. The surface of inner part wets faster and shows distinct aggregated water flow along the traversing line at the center of plate. This phenomenon can be shown easily at fully wetted time of each case. The Fig. 4.14 shows the snapshot of each width case at the center wetting time. The faster wetting of inside of two jets is confirmed at all cases. The different time at center wetting

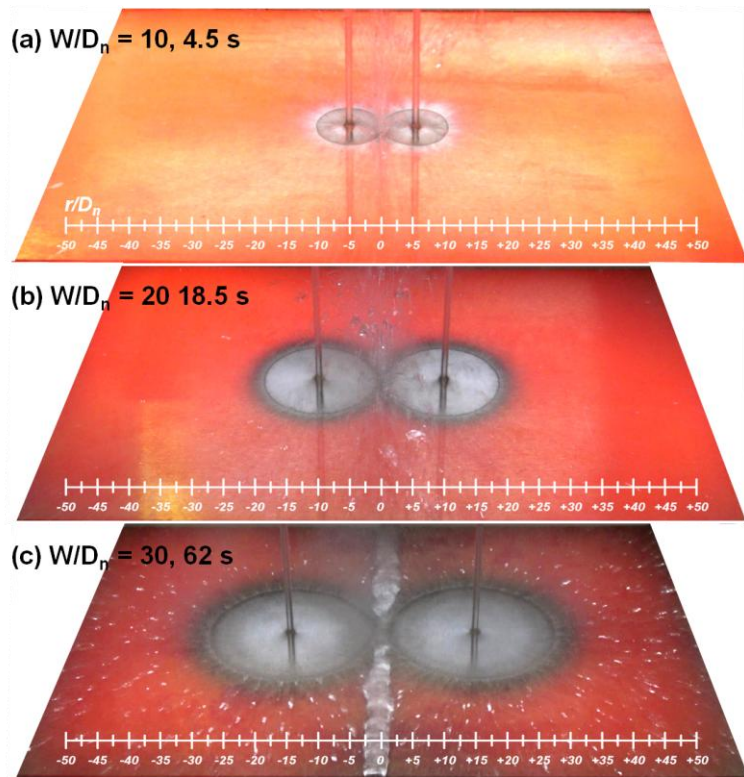


Figure 4.14 : Snapshot of boiling visualization at the center wetting time of  $W/D_n$  (a) 10, (b) 20, (c) 30.

time is shown with 4.5, 18.5 and 62 s for  $W/D_n$  of 10, 20 and 30, separately. After center wetting of plate, the interacting flow is formed and it is confirm that the similar shape of interaction of flow visualization of Fig. 4. 12.

#### 4.2.2 Boiling Heat Transfer Analysis of Two Interacting Jets

Figure 4.15 shows the sequence of images of two interacting jets quench along to jets separation distance. At the early stage, Fig. 4.15(a1), (b1) and (c1) shows small area of wetted region (gray) and the each jet flow behaves as independently with each other. The numerous droplets from each jet flow with small radius are observed and fast escape to outside of plate. Above mentioned, in the gray part of wetted region, single phase convection regime dominantly occurs. After the time of 50 s, the flow of two jets met and merged in Fig. 4.15(a1) and (b1). But for  $W/D_n$  of 30 cases, the flow not yet meets. It needs more elapsed time but, the droplet gathers and forms a fountain shape of interaction flow which is ejected outside along the traverse center line. After 50 s, all cases of two jets meet and show the aggregated water flow at the center. As the wetting radius becomes larger, the jet flow along radial direction becomes slower. The ejected droplet from the wetting front slowly ejected as hover over the surface without wetting.

Figure 4.16 shows the synchronization of boiling visualization combined with the radial distributions of the surface heat flux and heat transfer coefficient of  $W/D_n = 10$  case at various elapsed time. The red, blue and yellow line represents the heat flux, heat transfer coefficient and temperature, respectively. The time of 4.5 s in Fig. 4.15(a) is the time when the two jets meet at the center for the first time. In this figure, we should compare the center value with the outside position for same distance from each jet. So, in this case, the position of  $R_{do}/D_n = \pm 10$  is the comparable position for the interacting flow cooling (center position).

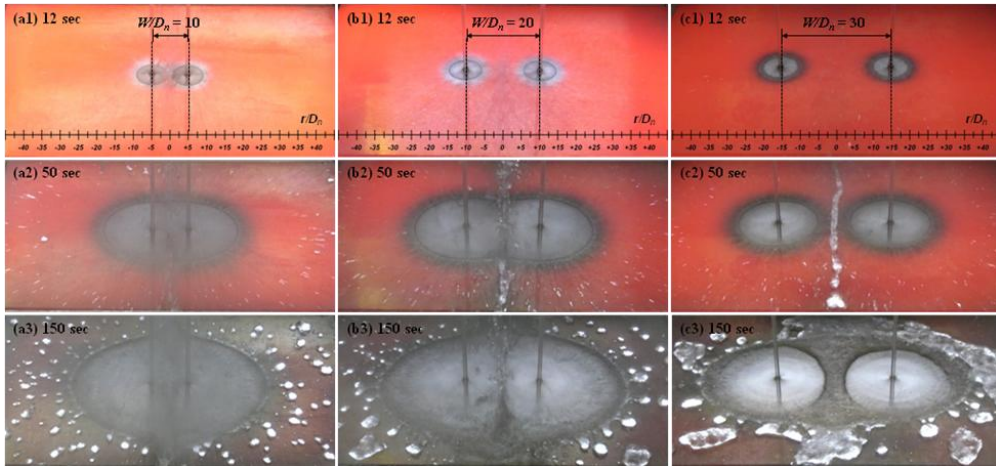


Figure 4.15 : Sequence images of two interacting jet quench along to jets separation distance at elapsed times of (a) 12, (b) 50, (c) 150 s.

The peak of heat flux graph always agrees with nucleate boiling regime. In all graph, the peak of heat flux almost coincidences with wetting front which is dealt in detail with previous section of single jet impingement. The heat transfer coefficient shows several peak values. Generally, the peaks around the wetting front are attributed to the nucleate boiling regime accompanying high heat flux. But the other peaks almost locate at the stagnation point of each jet as shown in Fig. 4.16(c) and (d). The value of heat flux of stagnation point is lower than that of wetting front, but the peak value of heat transfer coefficient means the relatively more heat flux occurs at the stagnation point even considering the lowest temperature of entire surface. Consequently, the lowest temperature is always positioned at the stagnation point with high heat transfer coefficient. The effect of interacting flow doesn't show critical in  $W/D_n = 10$  case because the distance is short and wetting of center occurs at early time. In the case of  $W/D_n = 20$  and  $30$ , it is easily confirm the effect due to

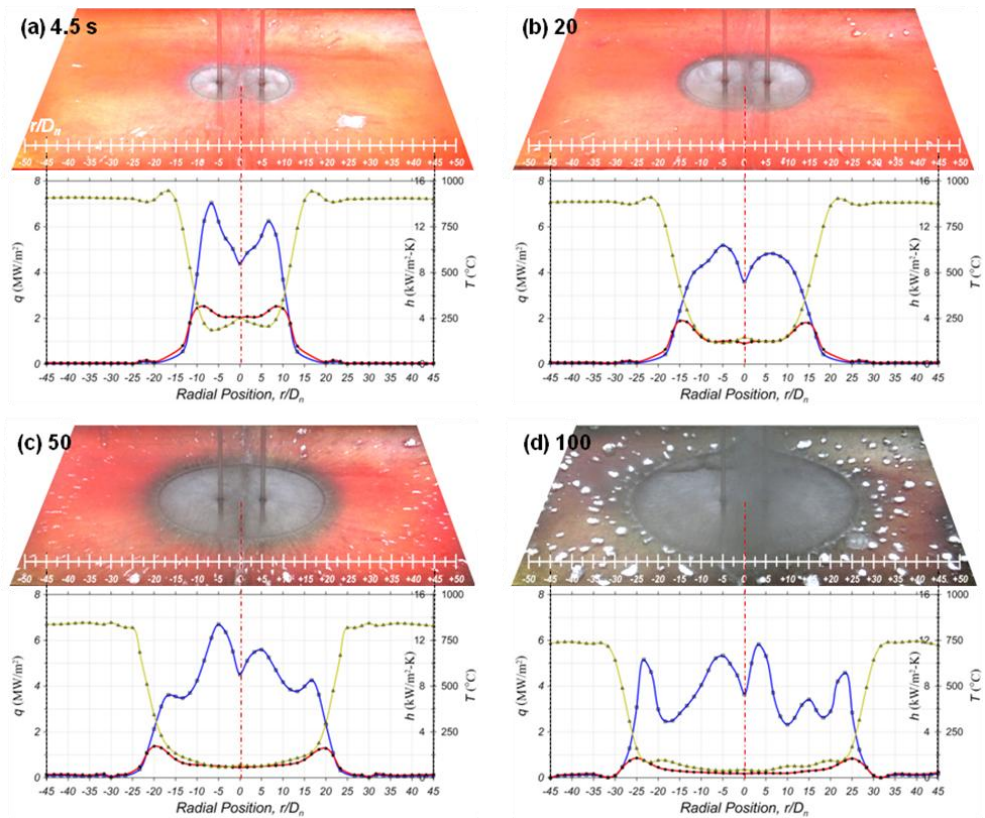


Figure 4.16 : Snapshot image combined with the radial distributions of the surface heat flux and heat transfer coefficient of  $W/D_n = 10$  case at elapsed time of (a) 4.5, (b) 20, (c) 50, and (d) 100s.

flow interaction. In the Fig. 4.17(a), the four of peak values are positioned at the wetting front of two jets. And as the two jet flow merged, tree peaks are shown in Fig. 4.17(b). This result shows that the wetting front is merged at the center position and the flow interacting can affect the boiling heat transfer regimes. But, the effect is not clearly shown in Fig. 4.17 of  $W/D_n = 20$  case. Anyways, the peaks of heat transfer coefficient are positioned at the wetting front or jet stagnation point in all figures. And the symmetric cooling performance can be also confirmed in the Fig. 4.16 and 4.17. Like as the Fig. 4.16, Fig. 4.17 shows maximum peak of heat transfer

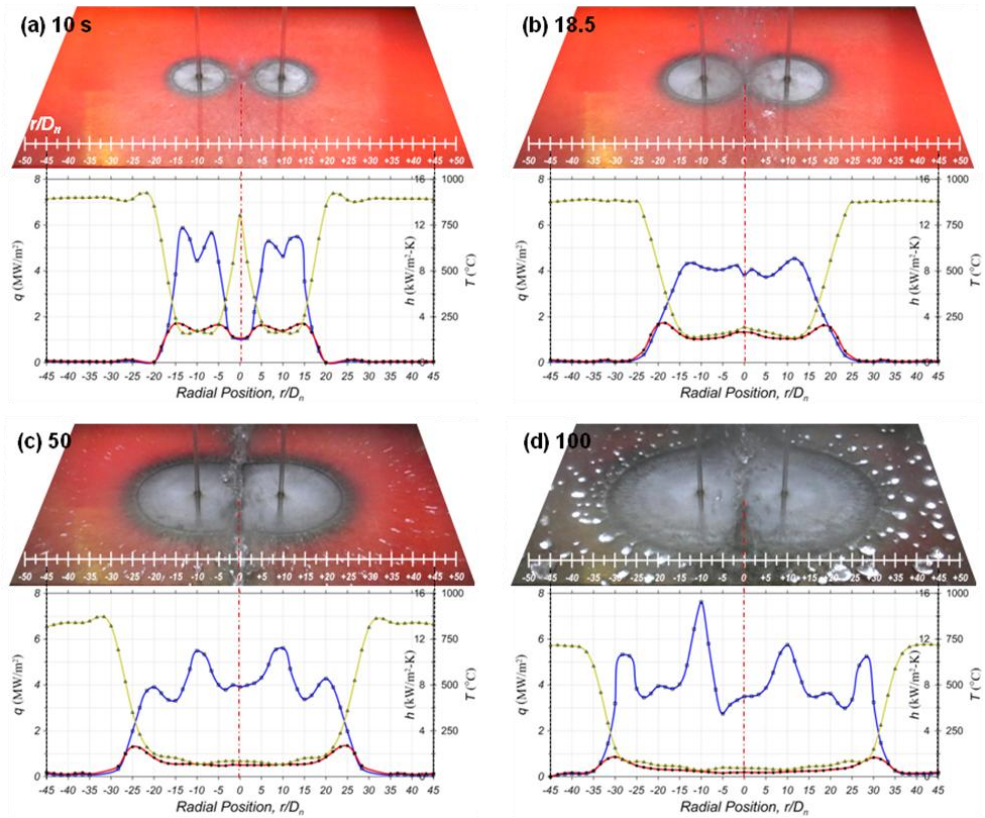


Figure 4.17 : Snapshot image combined with the radial distributions of the surface heat flux and heat transfer coefficient of  $W/D_n = 20$  case at elapsed time of (a) 4.5, (b) 20, (c) 50, and (d) 100s.

coefficient occurs at the wetting front with early elapsed time as shown in Fig. 4.16(a) and 4.17(a). And after some time, the peak values of blue line always position at the stagnation point in Fig. 4.16(b-d) and Fig. 4.17(b-d).

The synchronization result for  $W/D_n = 30$  case is dealt in more detail with more specific elapsed times in Fig. 4.18 and 4.19. As mentioned, the four peak values of maximum heat flux occur at wetting front of two jets until the merged flow occur at

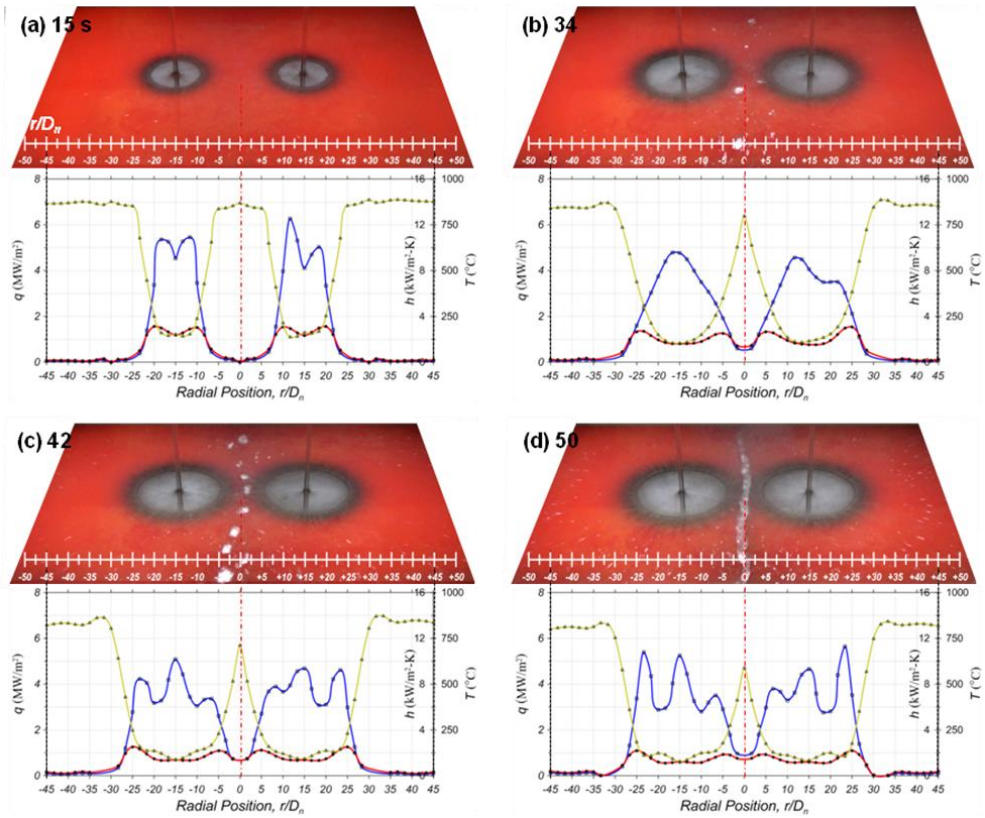


Figure 4.18 : Snapshot image combined with the radial distributions of the surface heat flux and heat transfer coefficient of  $W/D_n = 30$  case at elapsed time of (a) 15, (b) 34, (c) 42, and (d) 50 s.

center. In the case of  $W/D_n$  of 30, the merged interaction occurs at elapsed time of 62 s due to the large separation distance. So, the surface temperature of center is maintained in high until 50 s of Fig. 4.18(d) and shows rapid decrease at the merging time of 62 s of Fig. 4.19(a). Before the merging time of 62 s, an interesting interacting flow occurs at the center. In early stage, the droplets which are detached and popped from wetting front meet and combine with each other. The combined droplets fast ejected to the outside of plate along traverse line of center. As the time passes, the size of detached droplet grows and larger combined droplets are formed as shown

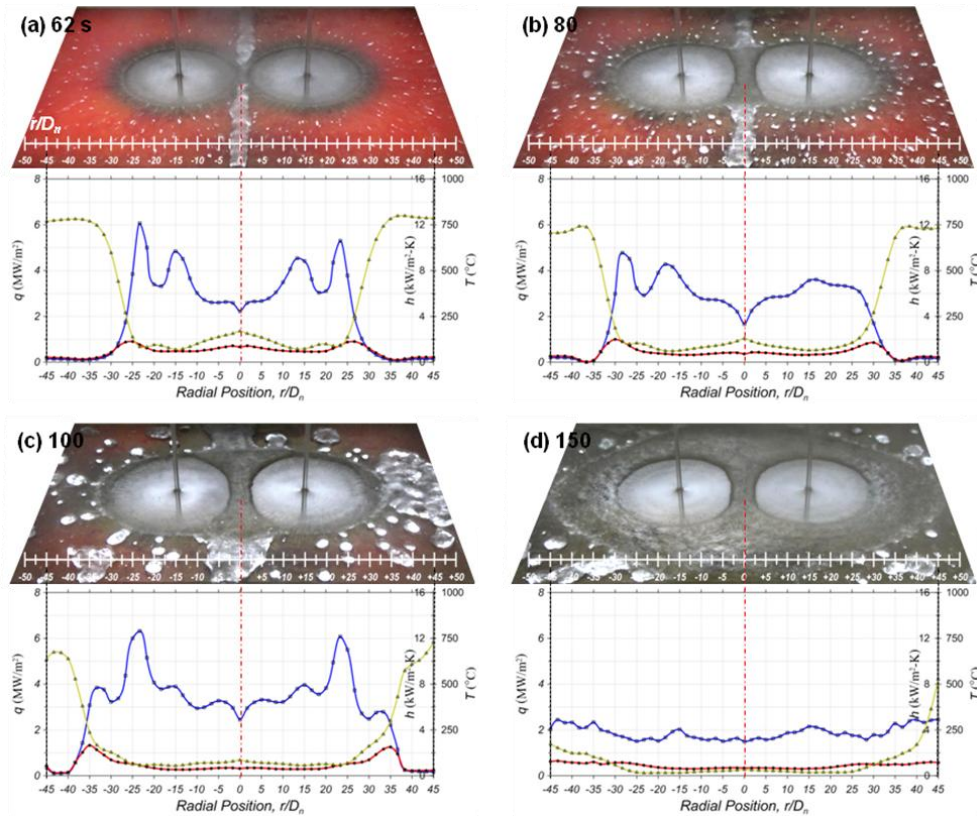


Figure 4.19 : Snapshot image combined with the radial distributions of the surface heat flux and heat transfer coefficient of  $W/D_n = 30$  case at elapsed time of (a) 62, (b) 80, (c) 100, and (d) 150 s.

in Fig. 4.18(a-c). After the time of 50 s, the combined droplet becomes a continuous interacting flow. That locates along the center line and continuously cools down the center surface without wetting surface until the time 62 s of Fig. 4.19(a). So, the center surface relatively cools and wets faster than the outside same distance position of two jet  $R_{d0}/D_n = \pm 30$ . After 80 s, the width of merged flow grows and finally combines with peripheral wetted region at time of 150s in Fig. 4.19(d). From these results, it is confirmed that the interacting flow affect to the boiling heat

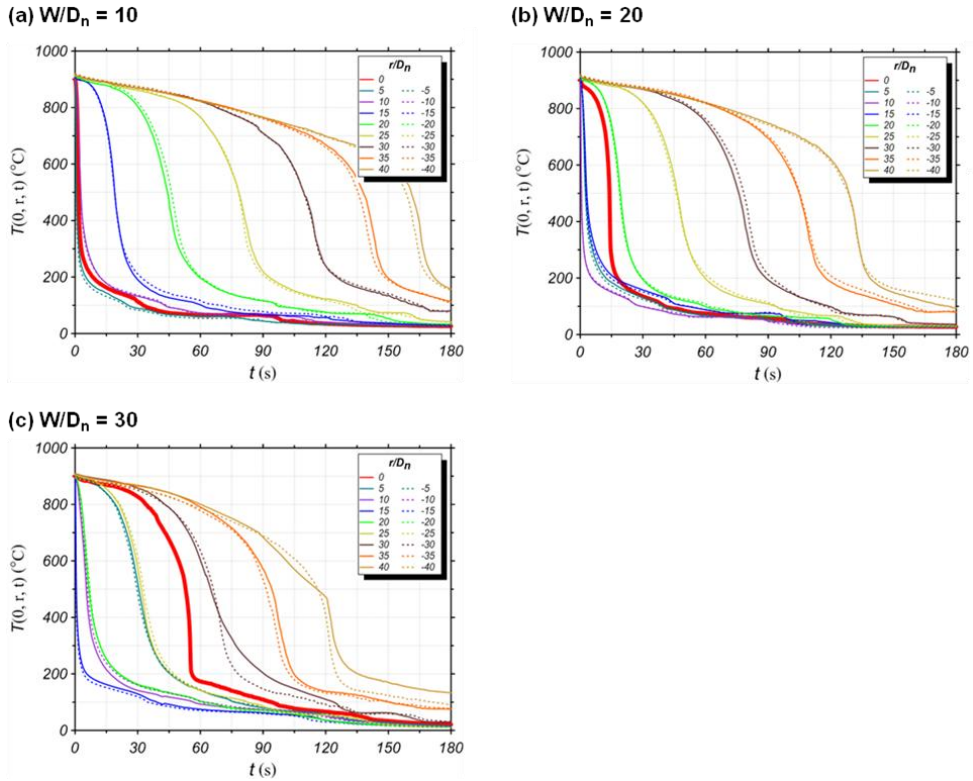


Figure 4.20 : Surface temperature distribution along with time of  $W/D_n$  (a) 10, (b) 20 and (c) 30. The thick red line represents the center position of plate.

transfer regime especially on center.

Figure 4.20 shows the surface temperature distribution with respect time of  $W/D_n$  10, 20 and 30. The thick red line represents the center position value. At first, we can see that the same distance position of graph form the center shows good cooling symmetry. And above mentioned, the center line should be compare with the same distance of outside of two jets. For example, the red line of Fig. 4.20(a), (b) and (c) could compare with  $R_{do}/D_n$  of  $\pm 10$ ,  $\pm 20$  and  $\pm 30$  , respectively. In Fig. 4.20(a), the red line show steeper graph than both of continuous and dashed purple line. And also, the red line of  $W/D_n$  20 and 30 shows faster cooling performance than the light

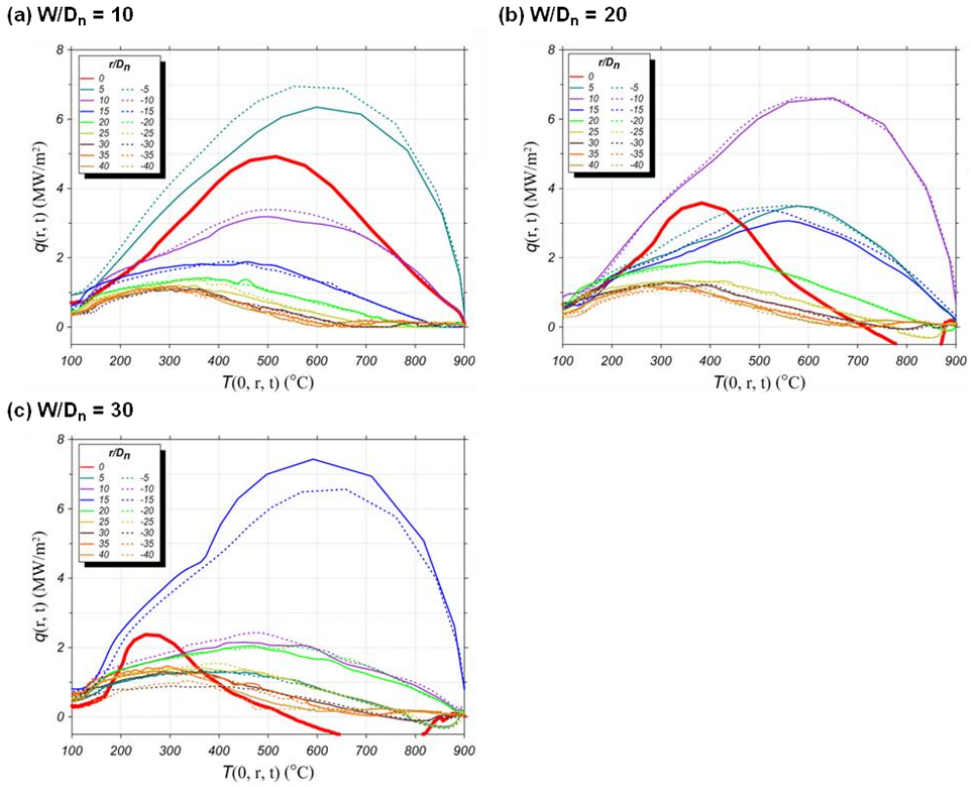


Figure 4.21 : Heat flux distribution against the temperature of  $W/D_n$  (a) 10, (b) 20 and (c) 30. The thick red line represents the center position of plate.

green and brown line like of Fig. 4.20(b) and (c). Second, the temperature of onset of nucleate boiling is changed. As shown in Fig. 1.1, almost perpendicular shape of temperature distribution graph represent for nucleate boiling regime. And it is also confirmed with heat transfer distribution of Fig. 4.21. The peak of each graph is the nucleation boiling point. As we can see, the peak of thick red line formed at lower temperature as the separation distance becomes larger. It is interesting result because the cooling performance of center grows due to the interacting flow, especially in Fig. 4.21(c). However, the peak of red line occurs at 250°C of surface temperature.

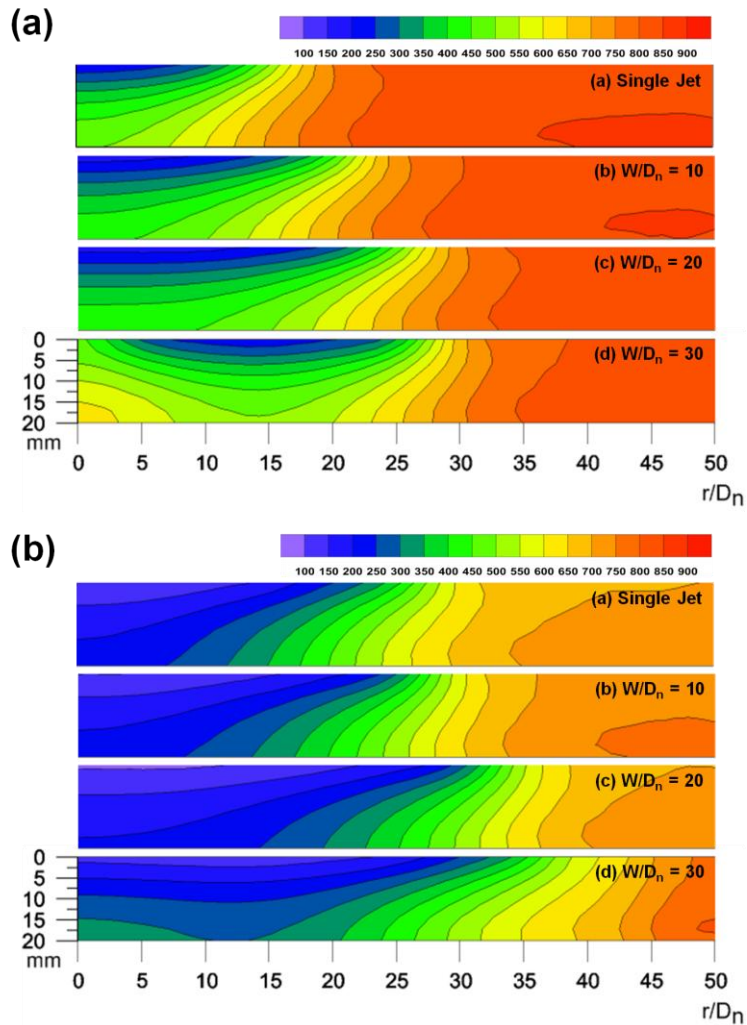


Figure 4.22 : Variations of the inverse-conduction predicted temperature distribution in radial direction at elapsed time of (a) 50, (b) 100 s.

It is the lowest value even considering entire graph of Fig. 4.21. This indicates that the interacting flow cools the center surface continuously, but the surface wetting of center is delayed due to the dynamic flow with radial momentum.

The temperature contour in radial and depth direction from the center along to  $W/D_n$  as shown in Figs. 4.22(a) and (b). The larger temperature gradient occurs at

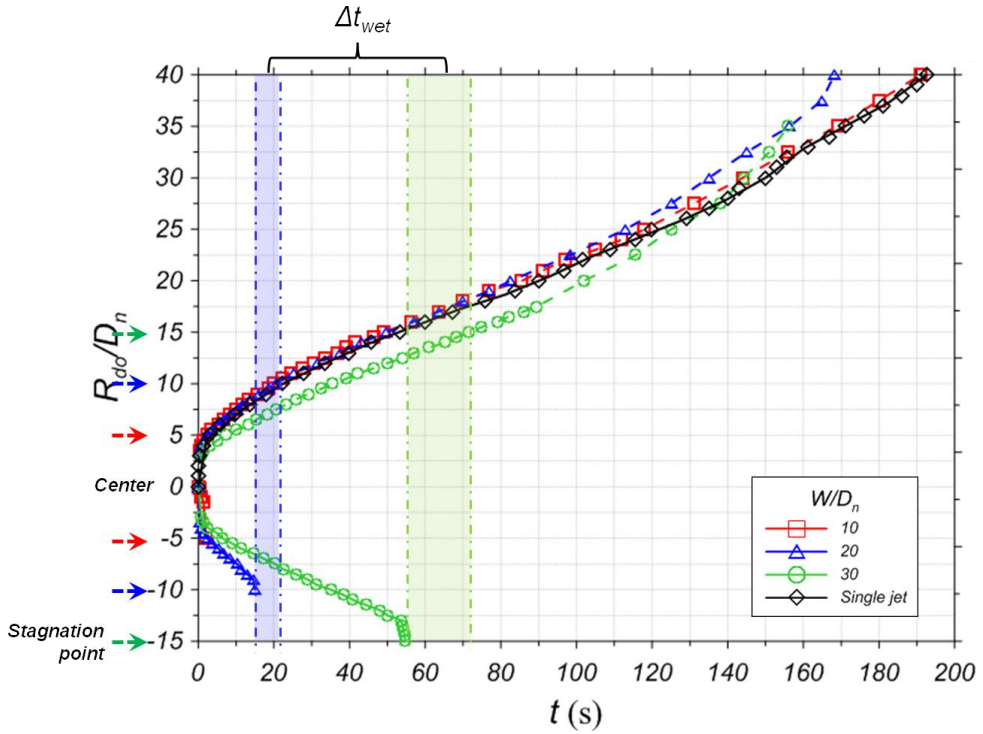


Figure 4.23 : Variation of the wetting front location with respect time, showing the quasi-steady regime where  $R_{do}$  increases linearly with time.

each stagnation point and causes larger conduction heat transfer rate in depth direction. As seen in Fig. (b), the inner part of two jets is cooled and the relatively large area, but the conduction heat transfer in depth direction is relatively high at the outward position.

Variation of the wetting front location with respect time is presented in Fig. 4.23. It is confirmed that the quasi-steady regime of single jet in Fig. 4.9 is also applied on the outer area of two jets. And also, the shortened time for wetting the same distance from each jet is marked in blue and green area for  $W/D_n$  of 20 and 30. With  $W/D_n$  of 30, the shortened time is almost 20 s.

### 4.2.3 Enhancement of Two Interacting Jets

In this section, we evaluate the enhancement of two interacting jets compared with single jet impingement. The heat transfer coefficient is set as a main comparable parameter. At first, the comparison is performed between single jet impingement and two interacting jets of  $W/D_n = 10$ . Fig. 4.24 shows the comparison of  $h$  at elapsed time of 50 s with red and blue line for single and two jets, respectively. It is easily distinguished that the under area of blue line is larger than that of red. The three peaks of single jet impingement is observed at one point for the stagnation point and the other point at wetting front. On the other hand, the four of peaks are shown with two interacting jet. The two peaks closer the center( $r/D_n = 0$ ) is attributed to the stagnation points of two jets. And the other peaks occur at the wetting front which located the outside of two jets.

It is seemed to be too reasonable that the cooling performance of two jets with same Reynolds number is larger than single jet impingement. However, this study finally develops and evaluates the multiple array jet with optimization of nozzle configuration like as nozzle-to-nozzle distance. So, the single jet is considered as infinite distance for jet separation. At first, the detailed comparison of single/two interacting jet( $W/D_n = 10$ ). The Fig. 4.25 shows the heat transfer coefficient enhancement of single jet and two interacting jet of  $W/D_n = 10$ . For the exact comparison, the average value of positive and negative coordinate is used and the red curved is shifted. In figure, the blue and red area represents for two jets and single jet enhancement. The enhancement ( $\eta$ ) is defined as,

$$\eta = \frac{A1 - A2}{A_{single}} \quad (4.1)$$

where  $A_{single}$  is the total area of single impinging jet. The calculated value of  $\eta$  is 67.2 %. This is significantly large value of enhancement and shows the number of jets can enhance the cooling performance. And second, the enhancement comparison along to jet separation distance is performed in Fig. 4.26. The Fig. 4.26(a) shows the area comparison for three separation distances and single jet. The calculated value of  $\eta$  by Eqs. (4.1) is 67.2, 42.3 and 37.3 for  $W/D_n = 10, 20$  and  $30$ , separately. Based on this calculated value, the enhancement graph along to  $W/D_n$  is presented. The result shows that maximum value occurs at  $W/D_n = 10$ . From this result, the number of nozzle and separation distance both can attribute for cooling performance.

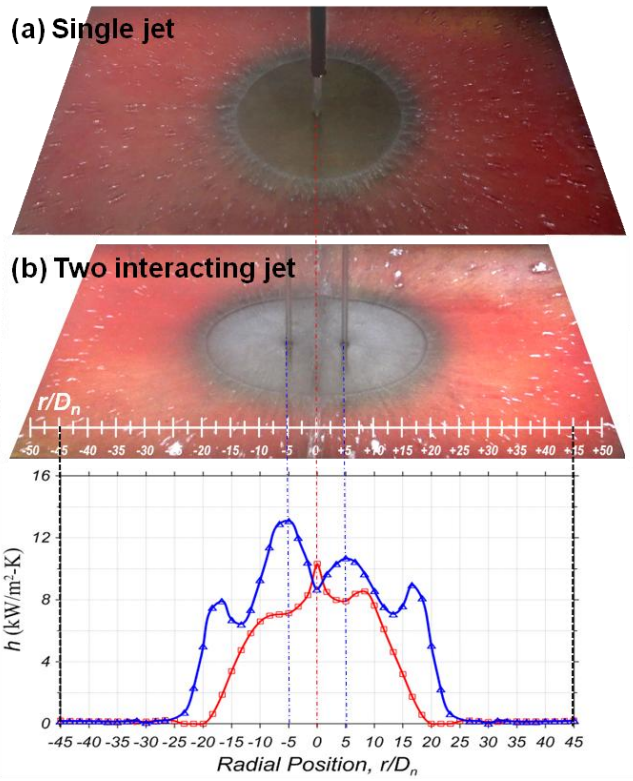


Figure 4.24 : Comparison of boiling visualization and heat transfer coefficient between single jet and two interacting jet of  $W/D_n = 10$ .

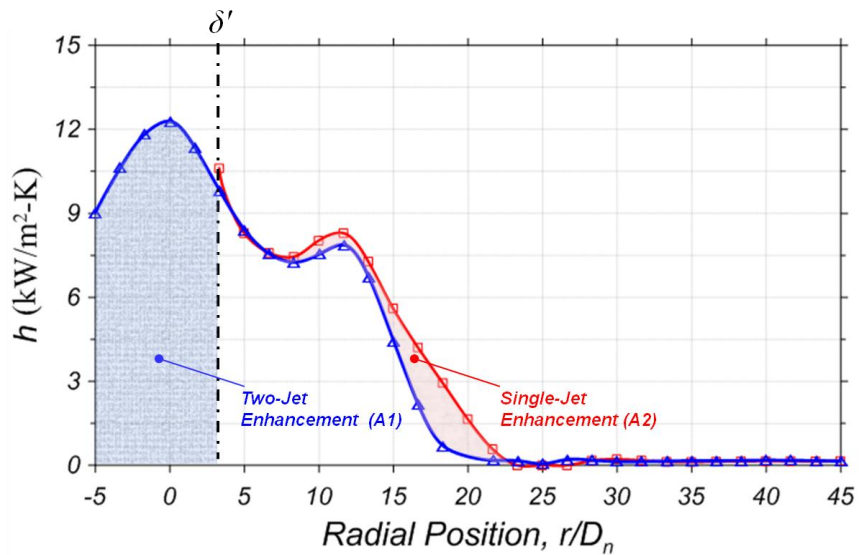


Figure 4.25 : Heat transfer coefficient enhancement ( $\eta$ ) of single jet and two interacting jet of  $W/D_n = 10$ .

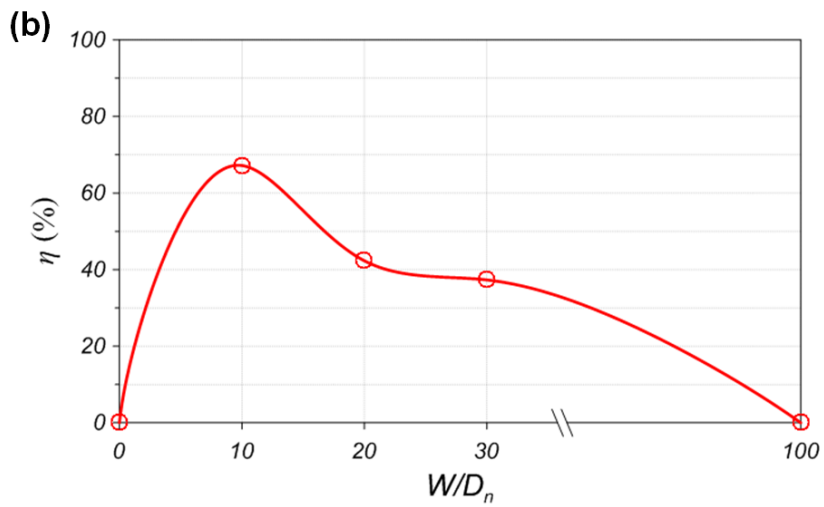
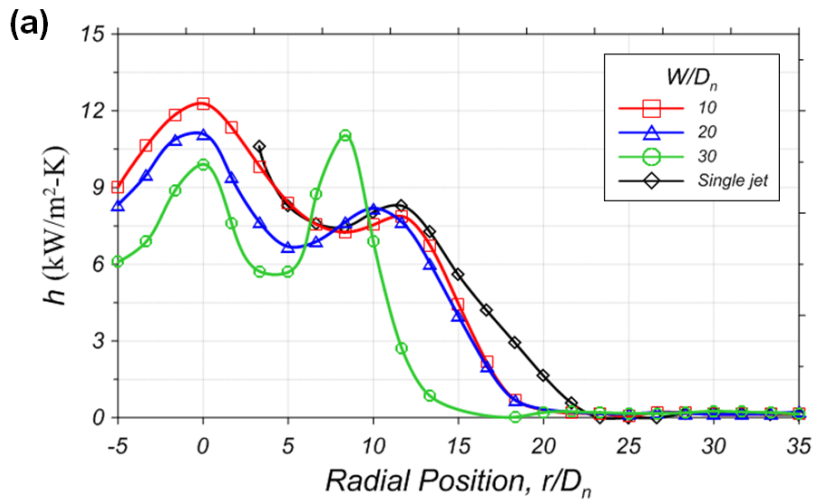


Figure 4.26 : Comparison of (a) heat transfer coefficient, (b) efficiency enhancement between single jet and two interacting jet of  $W/D_n = 10, 20, 30$  at elapsed time 50 s.

## 4.3 Comparison of 4-type of Quenching Method

### 4.3.1 Comparison of Heat Transfer Analysis of 4-type of Quenching Methods

Figure 4.27 shows sequence of high speed imaging during water immersion quenching at lateral surface. The effect of rotating speed is shown by comparing the no rotation and 3000 rpm case at Fig. 4.27(a) and (b), separately. In figure, boiling phenomena are visually shown, namely, film, nucleate boiling, and single phase convection. After the short elapsed time of Fig. 4.27(a-1) and (b-1), the vapor film (white) is observed overall surface where the highly heated surface remains unwetted by film boiling phenomenon. The light brown region which represent wetted surface expands as the time passes. In brown region on surface, we can distinguish the nucleate sites by watching the white air bubble where vigorously nucleate boiling occurs. Comparing no rotation of Fig. 4.27(a) with 3000 rpm Fig. 4.27 (b), the brown area commonly expands from the outside of surface into the inside but the collapsed time can be shortened by almost 30 % with stirrer rotation.

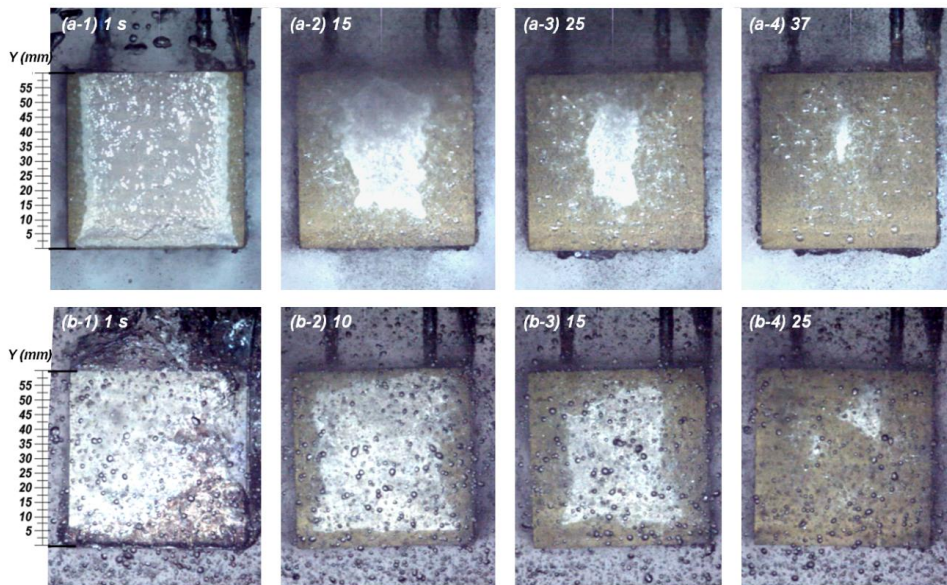


Figure 4.27 : Sequence of high-speed imaging of water immersion quenching at lateral surface with rotating speed of (a) no rotation and (b) 300 rpm.

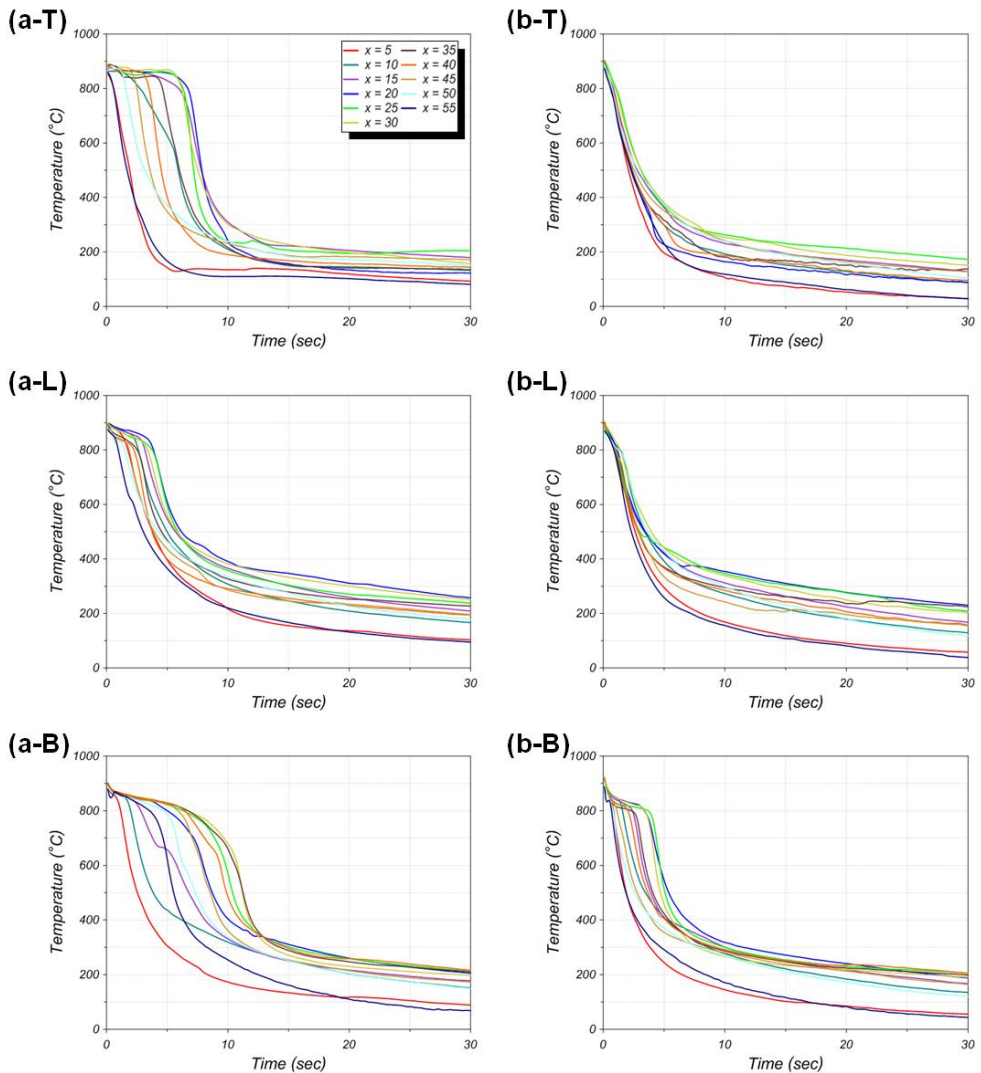


Figure 4.28 : Temperature distribution of water immersion quenching at rotating speed (a) no rotation, (b) 3000 rpm at T-top, L-lateral and B-bottom surface.

A quantitative analysis of IHCP result is shown in Fig. 4.28 and 4.29 which show transient temperature and heat flux distribution at top, lateral and bottom surface along elapsed time. The slope of each graph closely associates with the local boiling regime at specific time. There are three distinct three steps of gradient : a slow grade

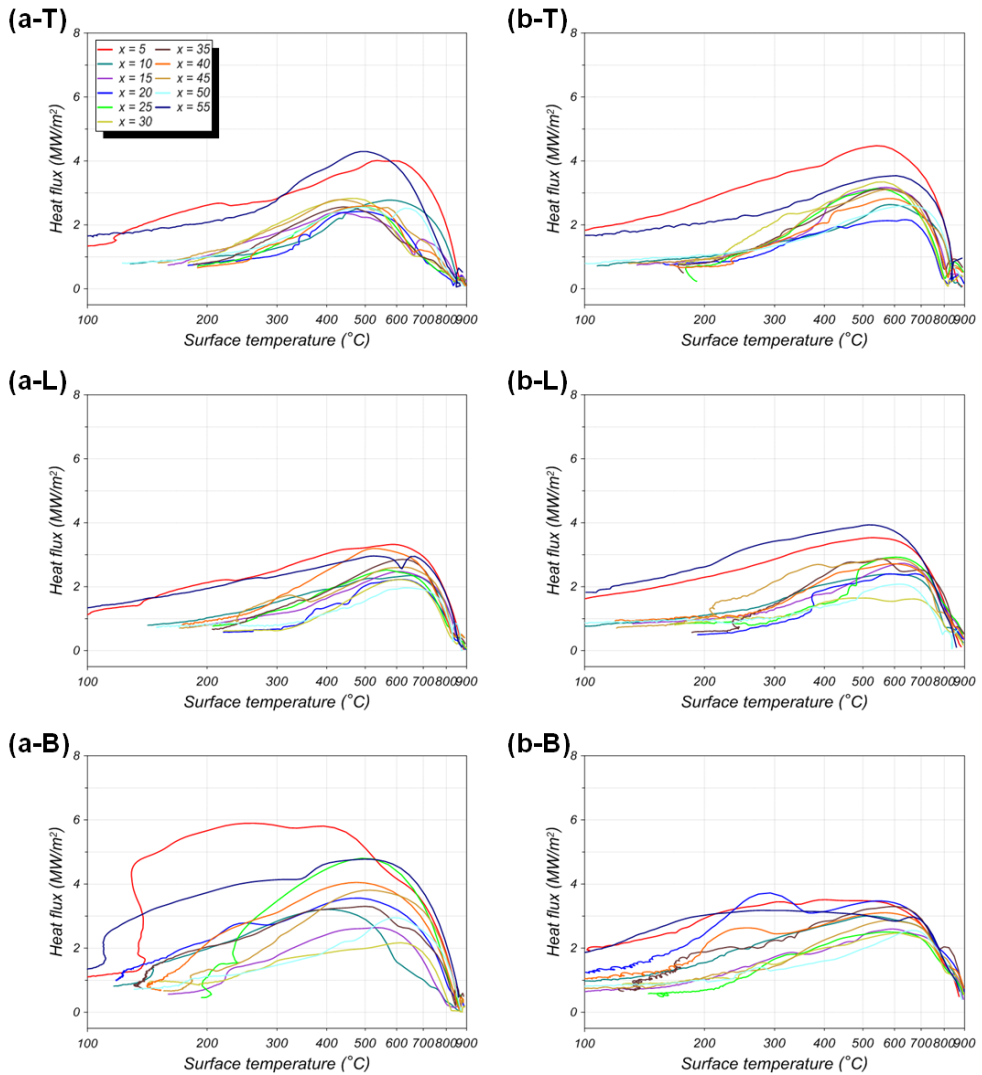


Figure 4.29 : Heat transfer distribution of water immersion quenching at rotating speed (a) no rotation, (b) 3000 rpm at T-top, L-lateral and B-bottom surface.

in early stage, a steep grade in middle stage and a modest gradient until final stage. Each step of slope is categorized as a film boiling, a nucleate boiling and single-phase convection, respectively. Each figure has eleven graphs at various spatial measured points and show that cooling rate of outside surface is faster than inside as shown in Fig. 4.27. With high rotation speed of Fig. 4.28(b), the slope of whole

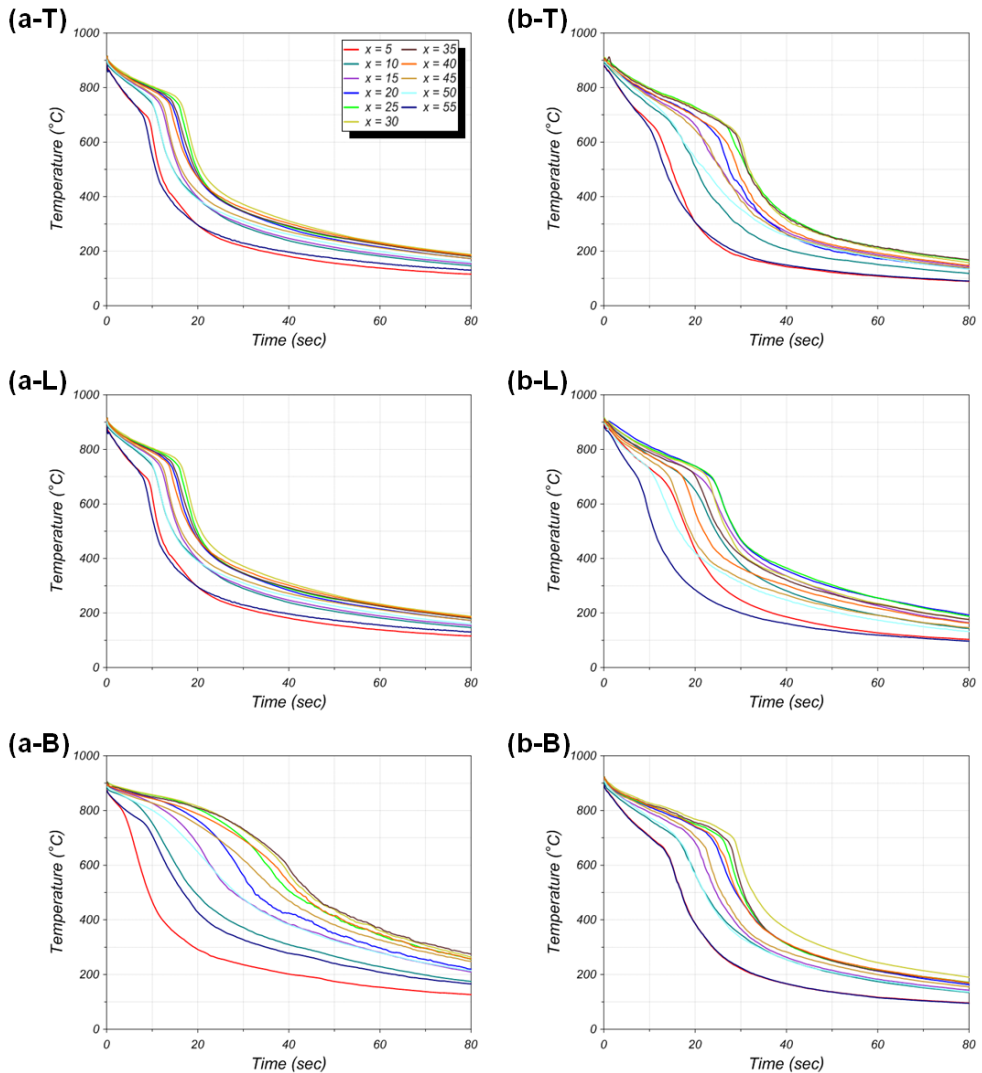


Figure 4.30 : Temperature distribution of oil immersion quenching at rotating speed (a) no rotation, (b) 3000 rpm at T-top, L-lateral and B-bottom surface.

surface becomes sharper and it means that the cooling rate can be faster with dynamic flow around surface. To compare the cooling uniformity of top, lateral and bottom surface, three figures are arranged at each case. Each graph of Fig. 4.27(a-T), (a-L) and (a-B) shows different trend of slopes. Especially, the film boiling of

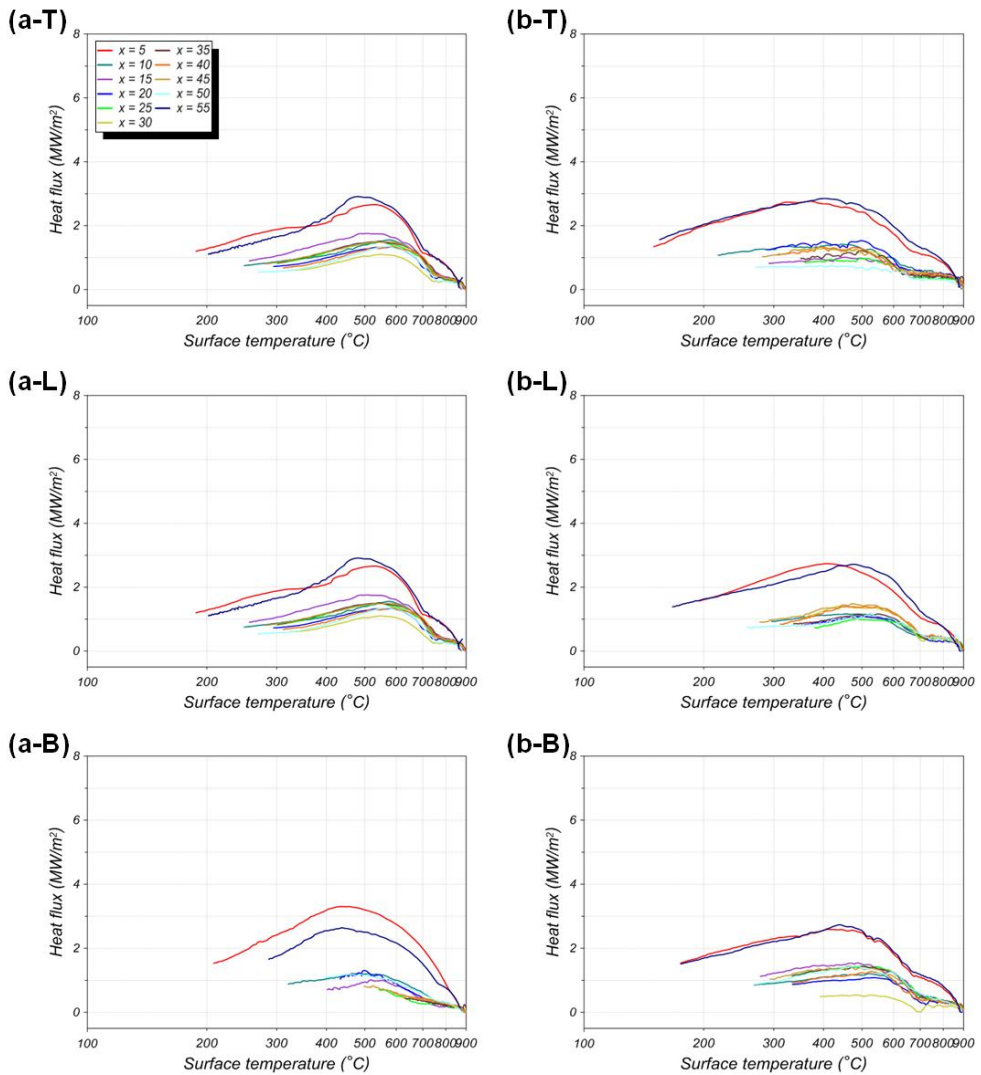


Figure 4.31 : Heat transfer distribution of oil immersion quenching at rotating speed (a) no rotation, (b) 3000 rpm at T-top, L-lateral and B-bottom surface.

bottom surface ends at late time than other surfaces. It is also shown in Fig. 4.28(b-B) comparing with Fig. 4.28(b-T), (b-L). Because the vapor film of formed on top and lateral surface can be easily departure than that of bottom by buoyancy effect. On the bottom surface, the vapor late longest and film boiling remains longer. These

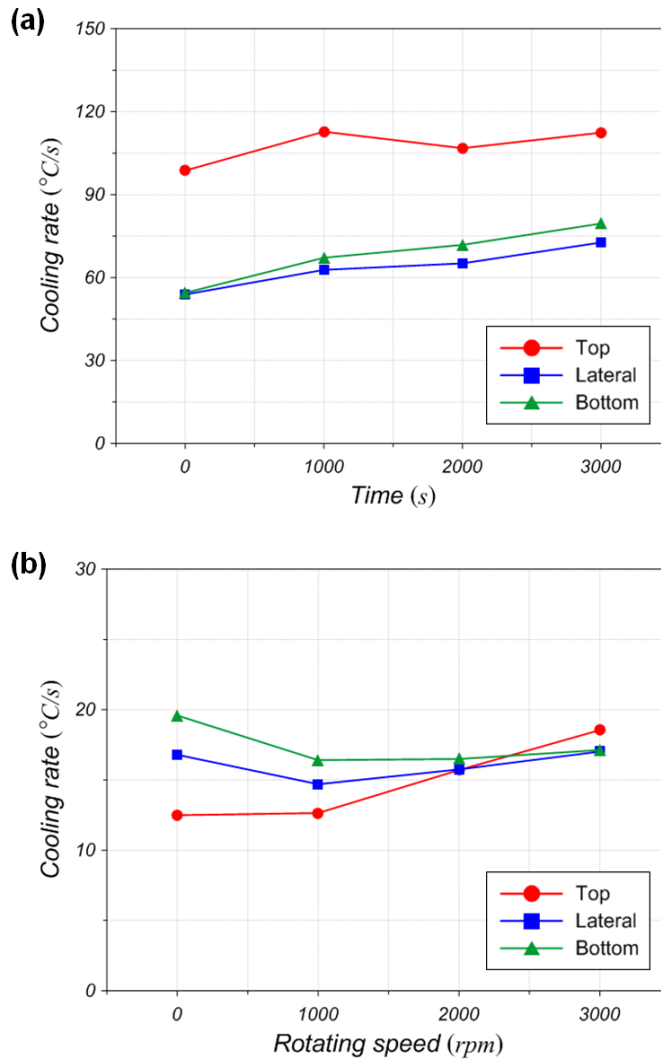


Figure 4.32 : Comparison of cooling rate of (a) water and (b) oil immersion quenching along the various rotation speed.

results are also confirmed by heat flux distribution of the Fig. 4.29. The Figs. 4.30 and 4.31 show transient temperature and heat flux distribution of oil immersion quenching. Unlike the water coolant, the oil has high boiling point of  $220^{\circ}\text{C}$  at 1 atm and has low latent heat capacity. So, the slope at the film boiling regime shows sharper gradient than water coolant and but film boiling last more longer time

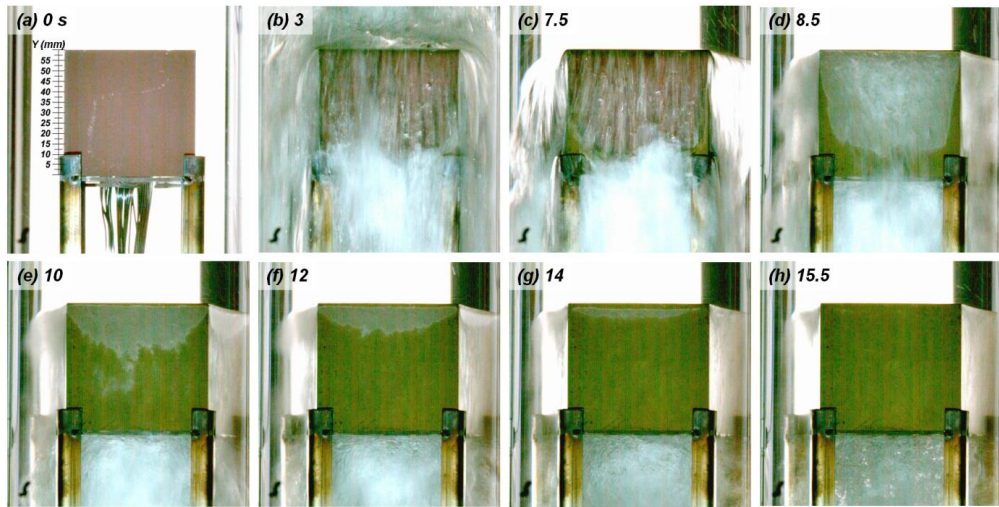


Figure 4.33: Consecutive boiling visualization images of forced immersion quenching at lateral surface along the various elapsed time.

because of its low cooling capacity. But the film boiling regimes last longer at bottom surface of Fig. 4.30(a-B), it shows vaporized oil is also affected by buoyancy force. And the dynamic flow by stirrer rotation shows not remarkable increase in cooling rate as compared in Fig. 4.30(a) and (b). But the cooling uniformity shows good agreement with each other surface as shown in Fig. 4.30, 4.31(b-T), (b-L) and (b-B). Fig. 4.32 shows comparison of cooling rate of water and oil immersion quenching along the various rotation speed. The surface cooling capacity of water shows almost 5 times higher than that of oil. The two of coolant mediums show difference enhancement in cooling rate. In case of water coolant, the cooling rates of entire surfaces (top, lateral and bottom) become grower as the rpm increase. But the cooling uniformity of three cases doesn't shows good agreement. Whereas the cooling uniformity of oil coolant becomes similar with increasing of rotation speed, and it shows almost same value at 2000 rpm.

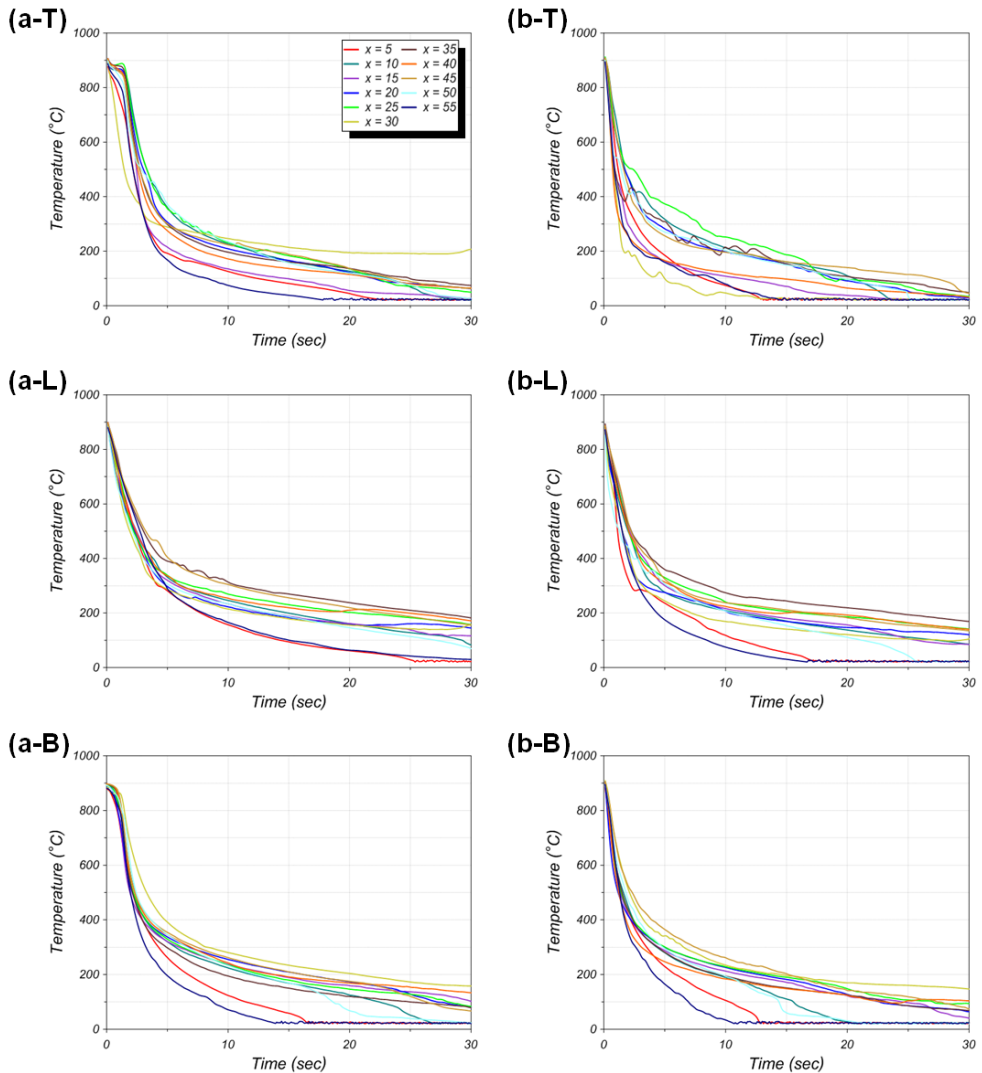


Figure 4.34 : Temperature distribution of forced immersion quenching with total flow rate of (a) 60, (b) 120 m<sup>3</sup>/hr at T-top, L-lateral and B-bottom surface.

Figure 4.33 shows the consecutive high-speed imaging of forced immersion quenching at lateral surface. The transient boiling behavior after the impact of forced immersion can be divided into two parts: wetted and unwetted zone. Each zone of surface accompanies with a distinct boiling mode. At unwetted zone where film

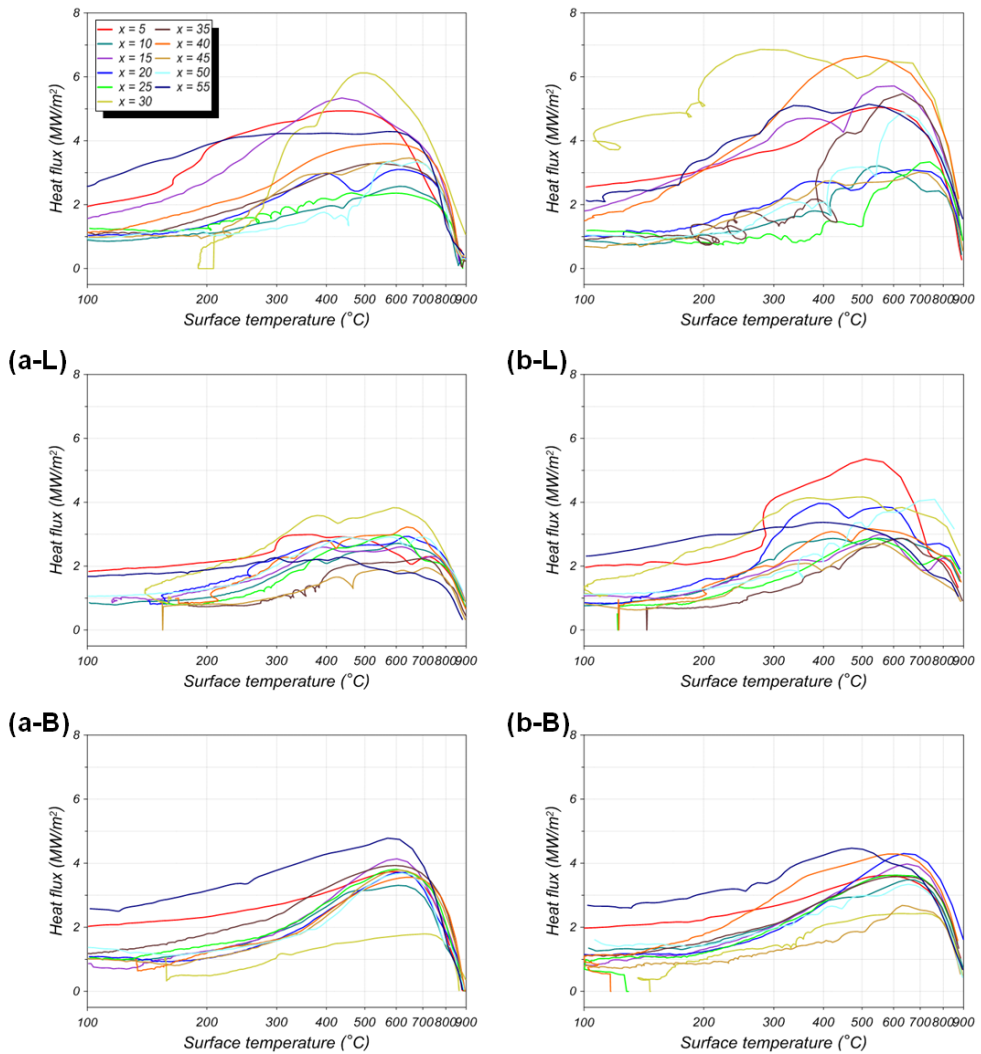


Figure 4.35 : Heat transfer distribution of forced immersion quenching with total flow rate of (a) 60, (b) 120 m<sup>3</sup>/hr at T-top, L-lateral and B-bottom surface.

boiling occurs, the surface is covered with vapor film which becomes a resistance to heat transfer. Whereas the nucleate boiling mode with high heat transfer coefficient occurs at the wetted zone. And the nucleate boiling results in the sharp temperature drop but disappears going through the transition boiling. After that, the single-phase convection accompanying gradual temperature drop is followed. As shown in Fig.

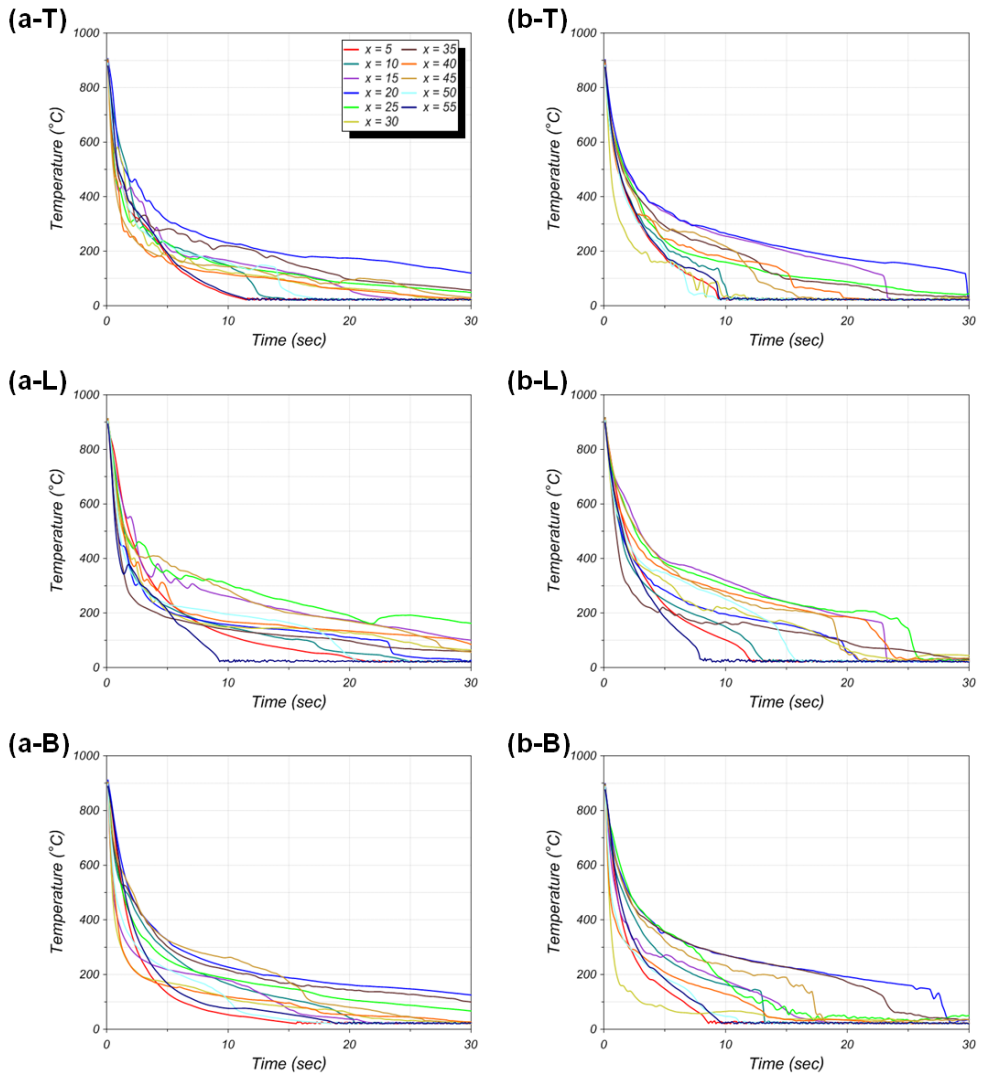


Figure 4.36 : Temperature distribution of multiple jet quenching with flow rate of each multiple jet nozzle (a) 10, (b) 20 m<sup>3</sup>/hr at T-top, L-lateral and B-bottom surface.

4.33, the surface wetting starts to occur from the bottom of the test block, this is attributed to the flow separation from the top-edge of the test specimen. As the cooling time goes by, the film boiling is rapidly depressed from the bottom and the nucleate boiling and single-phase convection turns to cover with the entire surface.

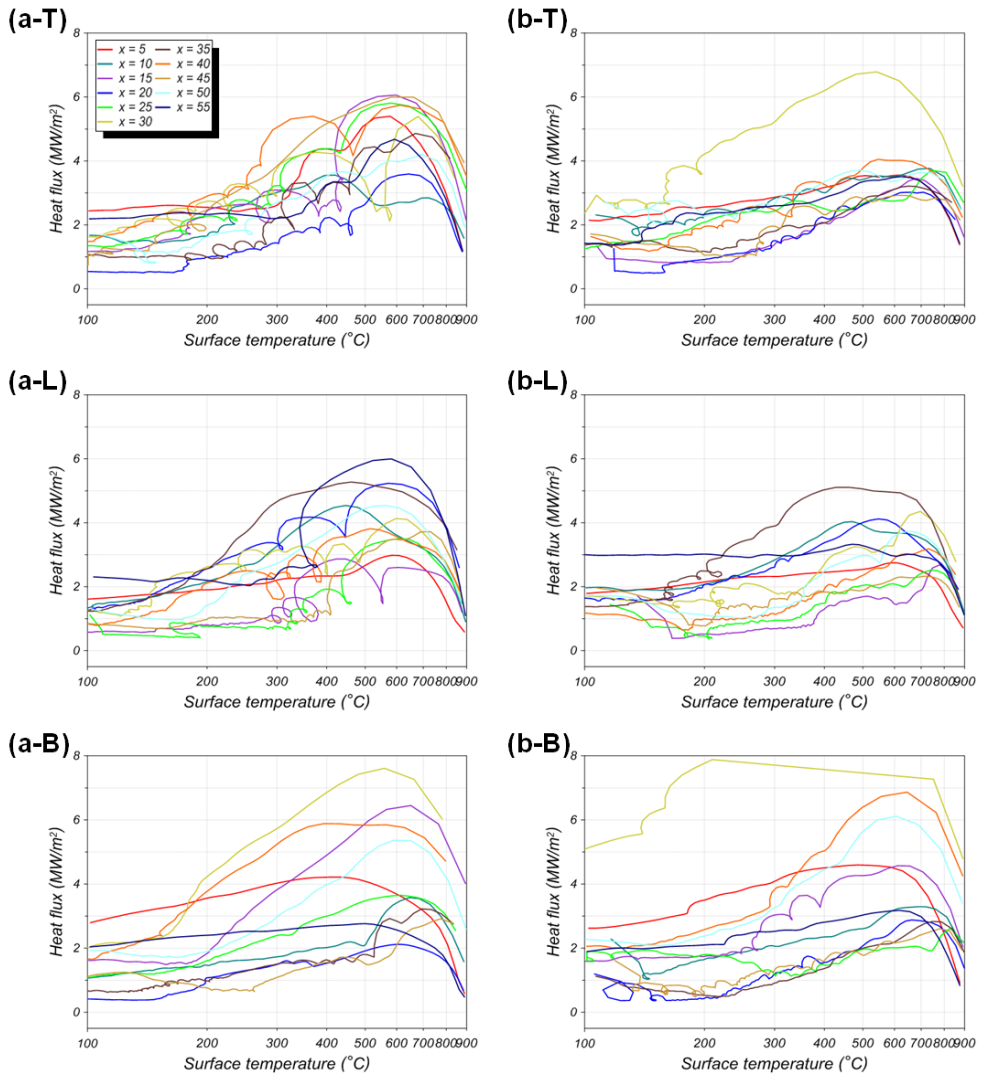


Figure 4.37 : Heat transfer distribution of multiple jet quenching with flow rate of each multiple jet nozzle (a) 10, (b) 20m<sup>3</sup>/hr at T-top, L-lateral and B-bottom surface.

The Figs. 4.34 and 4.35 show the transient temperature and heat flux distribution of forced immersion quenching. The temperature distribution shows sharper gradient than former quenching types. With total flow rate of 60 m<sup>3</sup>/hr of Fig. 4.35(a), the short period of film boiling regime is observed at lateral and bottom surfaces. The

lateral surface is cooled relatively slow due to the flow separation, whereas the top surface with direct impacting flow shows rapid cooling as shown in Fig. 4.33. So, the temperature distribution shows a sharper gradient at top surface than the lateral and bottom surfaces. And it is also confirmed at heat flux distribution of Fig. 4.35(a). Similarly, the maximum heat flux is attained in order of top, lateral and bottom surfaces. Fig. 4.34(b) and 4.35(b) shows heat treatment performance of twice as high in total flow rate of  $120 \text{ m}^3/\text{hr}$ . The film boiling regime doesn't show at any surface and shows higher maximum heat flux. By comparing the former three quenching type of water/oil immersion and forced immersion, we could know that the more dynamic flow efficiently remove the vapor film and can induce the nucleate boiling regime in early time. So, the heat treatment performance can be grower by using stirrer rotation for conventional immersion and large flow rate for forced immersion quenching. To enhance the cooling performance more, multiple jet impinging method of 4<sup>th</sup> quenching type is adopted to maximize the flow dynamic. The following results of 4<sup>th</sup> quenching type are shown in Fig. 4.36 and 4.37. Comparing with the same total flow of  $60 \text{ m}^3/\text{hr}$  ( $10 \text{ m}^3/\text{hr}$  of water is injected form six of multiple jet nozzle), Fig. 4.36(a) shows remarkable increase of cooling rate than Fig. 4.34(a). The film boiling regime doesn't shown at whole surfaces like as Fig. 4.34(b). And also, Fig. 4.37(a) even showed larger maximum heat flux than Fig. 4.37(b). With increase of flow rate up to  $120 \text{ m}^3/\text{hr}$  ( $20 \text{ m}^3/\text{hr}$  from each nozzle unit), the cooling rate shows little enhancement in cooling performance.

From above-results, we can identify the consecutive boiling phenomena with high-speed imaging and followed cooling performance. Finally, the comparison of

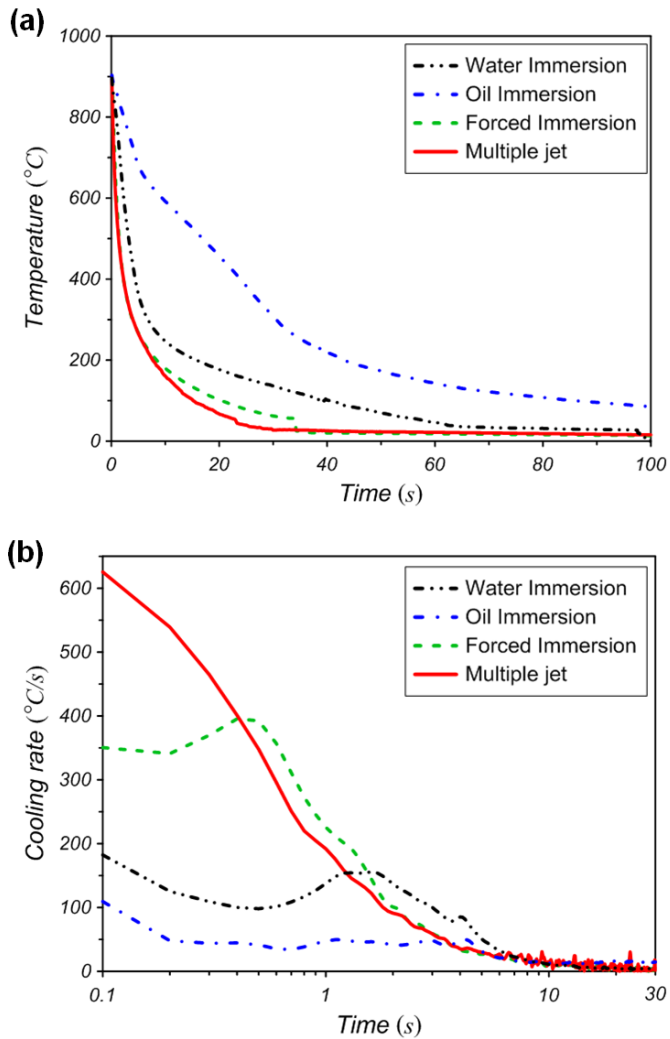


Figure 4.38: Comparison of cooling performance for 4-type quenching methods of (a) cooling curves and (b) cooling rate distribution.

cooling performance of 4-type of quenching methods are investigated in Fig. 4.39. For the comparison, the most efficient conditions are compared as a representative case of each quenching method. Fig. 4.38(a) shows the comparison of average cooling curve. The fastest cooling performance is achieved with 4<sup>th</sup> type of multiple jet quenching. And the next rapid cooling is obtained in order of Forced immersion,

water and oil immersion. It means that dynamic flow by jet impingement is mostly effective method in rapid cooling. This is also confirmed with cooling rate comparison of Fig. 4.38(b). The maximum cooling rate of multiple jet quenching is achieved with elapsed time of almost 0 s, and this indicate the nucleate boiling regime occurs right after quenching start without film boiling. From these results, it can be confirmed that jet impinging is most efficient methods by removing the vapor film on surface and induce nucleate boiling regime in early stage.

### ***4.3.2 Comparison of Microstructure Analysis of 4-type of Quenching Methods***

In order to study the relationship of cooling performance with microstructure and mechanical properties, the morphology of quenched surface by each quenching type are observed in this section. The Fig. 4.39 shows transient temperature distribution of 4-type of quenching methods at 1 mm from surface. Only nine of holes for temperature measurement are machined like as Fig. 2.6(b) to obtain sufficient samples for microscopic test. Three holes are assigned to the top, lateral and bottom surface, respectively. As mentioned in previous section. the cooling performance of bottom of water/oil immersion quenching shows slow gradient than top and lateral surface like as Fig. 4.39(a) and (b). In Fig. 4.39(c), the cooling rate of top surface shows most rapid cooling performance at forced immersion quenching. The graph of multiple jet quenching of Fig. 4.39(d) shows most rapid gradient.

SEM micrographs of quenched surface after each quenching method are presented in Fig. 4.40. The etched samples of quenched SNCM439 alloy steel were used for observing the microstructure by means of SEM. The SEM images were binarized in gray and black to distinguish martensite from bainite. In this figure, light gray and gray parts represent for martensite and black for bainite micro structure. With water and oil immersion quenching shown as Fig. 4.40(a) and (b), the relatively large black spots of bainite are shown with volume fraction of 8.5 and 17.5%, respectively. Whereas, with high cooling rate of Fig. 4.40(c) and (d), the black spots shows remarkable decrease with volume fraction of 1.4% and 0.1%. Form this result, it is confirmed that the martensite structure mainly formed with high cooling rate. Especially, almost 100 % of martensite structure is formed on quenched surface with

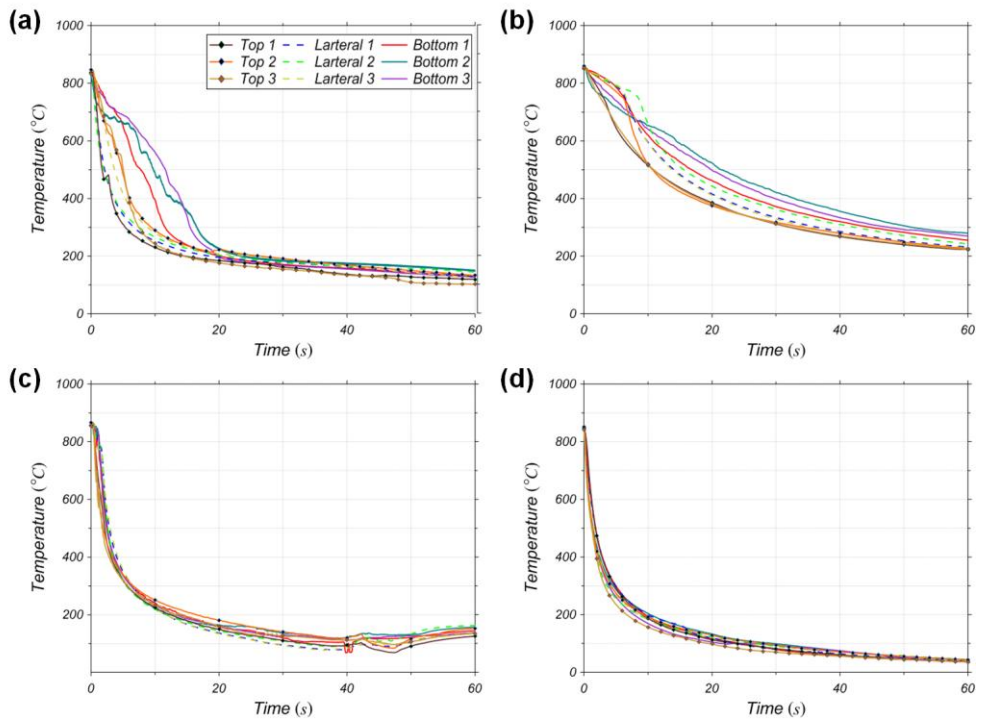


Figure 4.39 : Transient temperature distribution of 4-type of quenching methods (a) water immersion, (b) oil immersion, (c) forced immersion and (d) multiple jet quenching at measuring position of 1 mm from surface.

multiple jet quenching. Fig. 4.41 and 4.42 shows the comparison of surface elongation/hardness profiles of 4-type of quenching methods. The largest surface elongation form on after quenched surface with multiple jet quenching with the value of 24%, but the order of following little differs. The water quenching shows good elongation than forced immersion quenching. And for the surface hardness, the trend is perfectly accords with the cooling rate order. The multiple jet quenching shows the largest value with 711.5 *Hv*. And it is confirmed that that order of hardness continues until 10 mm in depth direction.

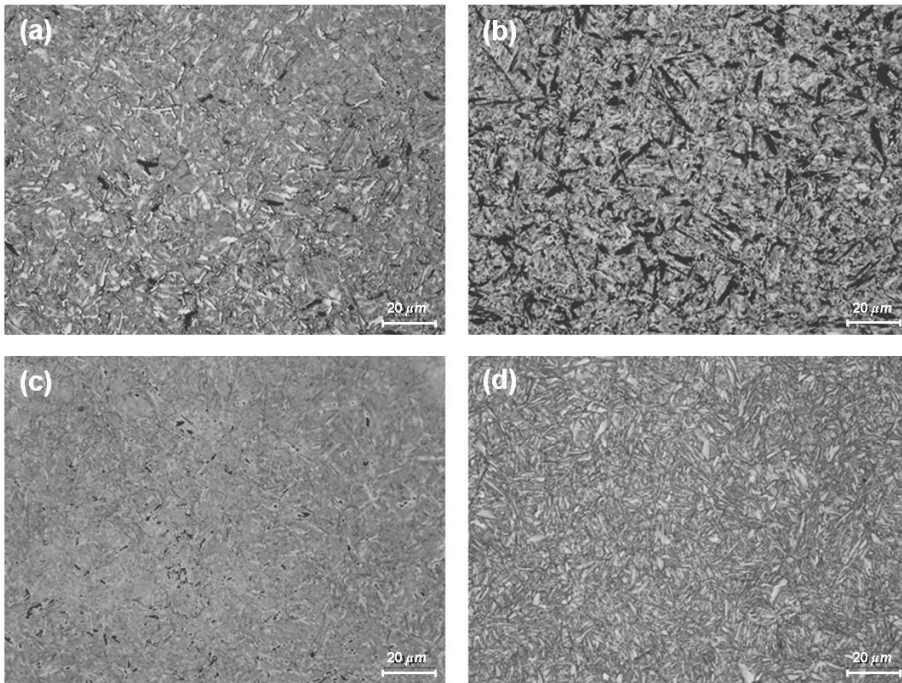


Figure 4.40 : SEM images of quenched surface where light gray and gray represent for martensite and black for bainite after (a) water, (b) oil, (c) forced immersion and (d) multiple jet quenching.

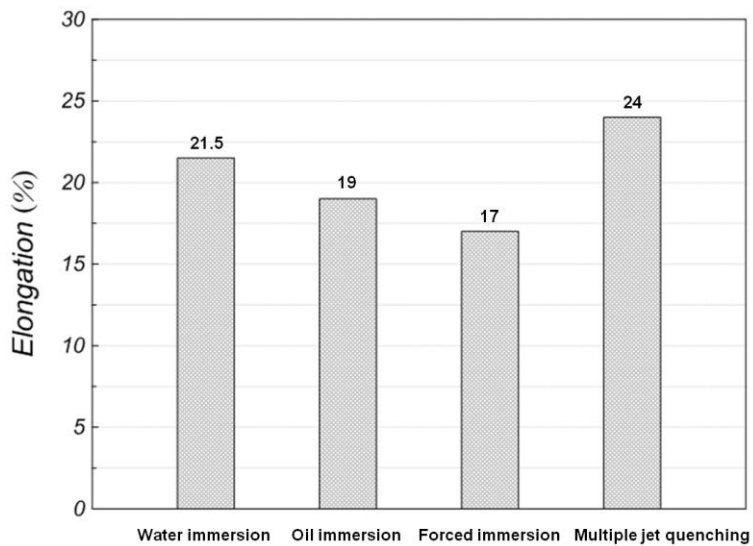


Figure 4.41 : Comparison of elongation profile of 4-type of quenching methods.

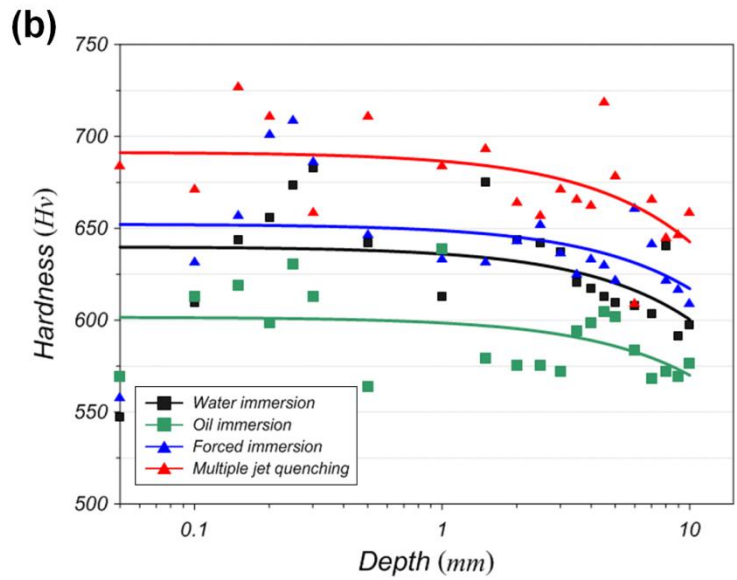
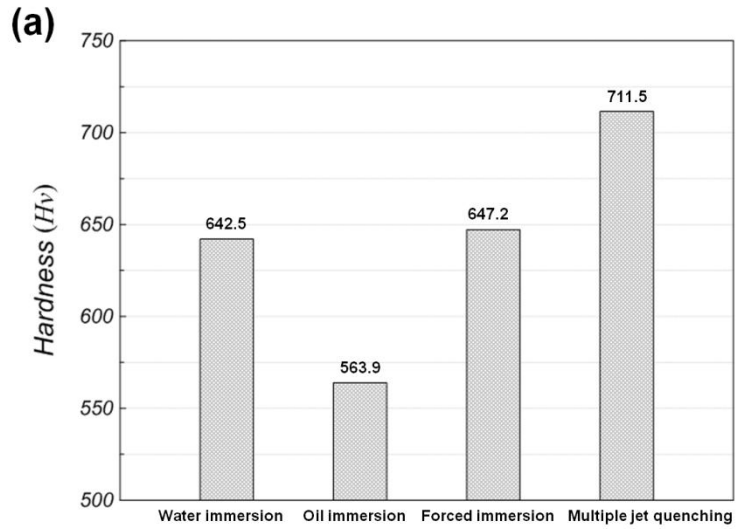


Figure 4.42 : Hardness profiles of 4-type of quenching methods at (a) surface and along (b) depth thickness from surface.

## 5. Concluding Remarks

An experimental study for water jet impingement has been carried out to understand the boiling heat transfer over the relatively higher initial temperature and wide flat plate. With high-resolution imaging and inverse heat conduction analysis we explore very high initial superheat and large surface area features of quench jet impingement boiling and explain the presence of (i) single-phase, (ii) collapsed-bubble (subcooled boiling), (iii) wetting front with ejecting droplets, and (iv) evaporating-droplets cooling regions on the plate. In the wetted region which covers the first three, the high heat flux is the largest. The wetting (or wet) front experiences violent nearly saturated nucleate boiling with high pressure bubbles erupting and causing ejection of droplets toward the dry region. The droplet-evaporation region is also very effective in cooling the plate. Heat conduction within the metallic plate is critical, with cooling spreading both laterally and through the plate. This is demonstrated through the 3-D graph of the measured surface heat flux and temperature at various radial locations versus time, and the predicted axisymmetric transient temperature distribution within the plate. A quasi-steady behavior prevails with the effect of thickness and thermal properties of specimen, where the radial wetting front location increases linearly with time. Liquid is ejected as droplets at the wetting front, and the analysis shows once the quasi-steady state is reached, the fraction of liquid ejected increases linearly with time and reaches over 10% of the liquid flowing out the nozzle. These ejected droplets land on the otherwise dry region and evaporate, which the evaporation rate depends on the local

surface superheat at their landing location. This evaporation cooling is very important in quench jet impingement cooling, as it substantially reduces the local surface temperature before the wetting front reaches it. Furthermore, two interacting jet impingement is experimented and numerically analyzed. The main variable is the separation distance of two jets and the other conditions are set as same with single jet impingement to compare the enhancement. In quenching with two interacting jets, the interacting flow is observed at the center of plate which affects the boiling heat transfer. And the faster spreading of wetting front is confirmed and in the merged region the heat transfer coefficient increases substantially. Furthermore, the enhancement of two interacting jet is evaluated by comparing with single jet. The heat transfer coefficient of 50 s is presented and shows increase in 67.2 %. From this result, the number of nozzle and separation distance both can attribute for cooling performance.

Another interesting observation in this study is comparative analysis of 4-type of quenching methods using boiling heat transfer and microscopic analysis. The distribution data of thermal properties shows the remarkable difference of cooling rate. Through a final heat transfer comparison, the cooling performance could be seen in the following order: Multiple jet quenching, Forced immersion, water and oil immersion. But, with highly agitating flow by stirrer rotation, water coolant shows enhancement in overall cooling rate. Whereas oil coolant shows improvement in cooling uniformity. The forced immersion shows improved cooling rate with high flow rate. But in multiple jet quenching, high cooling capacity is easily obtained at low flow rate in multiple jet quenching.

Additionally, the volume fraction of martensite shows good agreement with cooling capacity of each quenching method.

# References

- [1] F. C. Kohing, Waterwall: Water cooling systems, *Iron Steel Engineering*, 62 (1985) 30-36.
- [2] S. J. Chen, J. Kothar, Temperature distribution and heat transfer of a moving strip cooled by a water jet, *ASME paper*, (1988) 88-WA.
- [3] R. Viskanta, F. P. Incropera, Quenching with liquid jet impingement, *Heat and Mass Transfer in Materials Processing*, (1990) 455-476.
- [4] M. Kiryu, Development of oil-cooled 750 cc motorcycle engine, *Automobile Technology*, 40 (1986) 1154-1158.
- [5] H. Yamamoto, Y. Udagawa, M. Suzuki, Cooling system for FACOM M-780 large scale computer, *In Proceedings of the International Symposium on Cooling Technology for Electronic Equipment*, (1987) 701 -714.
- [6] D.H. Wolf, F.P. Incropera, R. Viskanta, Jet Impingement Boiling, *Advances in heat transfer*, 23 (1993) 1–132.
- [7] R. J. Copeland, Boiling heat transfer to a water jet impinging on a flat surface. *Ph.D. Thesis, Southern Methodist University, Dallas*, (1970).
- [8] M. A. Ruch, J. P. Holman, Boiling heat transfer to a Freon-113 jet impinging upward onto a flat, heated surface, *International Journal of Heat and Mass Transfer*, 18 (1975) 51-60.

- [9] M. Monde, Y. Okuma, Critical heat flux in saturated forced convective boiling on a heated disk with an impinging jet-CHF in L-regime, *International Journal of Heat and Mass Transfer*, 28 (1985) 547-552.
- [10] M. Monde, Y. Katto, Burnout in a high heat-flux boiling system with an impinging jet, *International Journal of Heat and Mass Transfer*, 21 (1978) 295-305.
- [11] T. Nonn, Z. Dagan, L. M. Jiji, Jet impingement flow boiling of a mixture of FC-72 and FC-87 liquids on a simulated electronic chip, *In Proceedings of the 1989 National Heat Transfer Conference-Heat Transfer in Electronics*, 111 (1989) 121-128.
- [12] M. Katsuta, T. Kurose, A study on boiling heat transfer in thin liquid film (2nd report, *the critical heat flux of nucleate boiling*). *Transactions of JSME B*, 47 (1981) 1849-1860.
- [13] H. Martin, Heat and mass transfer between impinging gas jets and solid surfaces, *Advances in heat transfer*, 13 (1977) 1-60.
- [14] S. J. Downs, E. H. James, Jet impingement heat transfer - a literature survey, *ASME, AIChE, and ANS, 24th National Heat Transfer Conference and Exhibition*, (1987) 87-HT-35.
- [15] S. Polat, B. Huang, A. S. Mujumdar, W. J. M. Douglas, Numerical flow and heat transfer under impinging jets: a review. *In Annual Review of Numerical Fluid Mechanics and Heat Transfer*, 2 (1989) 157-197.
- [16] C. S. K. Cho, K. Wu, Comparison of burnout characteristics in jet impingement cooling and spray cooling, *In Proceedings of the 1988 National Heat Transfer Conference*, 1 (1988) 561-567.

- [17] Y. Katto, M. Kunihiro, Study of the mechanism of burn-out in boiling system of high burn-out heat flux, *Bulletin of JSME*, 16 (1973) 1357-1366.
- [18] Y. Katto, K. Ishii, Burnout in a high heat flux boiling system with a forced supply of liquid through a plane jet, *Proceedings of the 6th International Heat Transfer Conference*, 1 (1978) 435-440.
- [19] C. F. Ma, A. E. Bergles, Boiling jet impingement cooling of simulated microelectronic chips, *ASME, New York*, 28 (1983) 5-12.
- [20] S. Toda, H. Uchida, Study of liquid film cooling with evaporation and boiling. *Heat Transfer-Japanese Res.*, 2 (1973) 44-62.
- [21] Y. Y. Hsu, On the size range of active nucleation cavities on a heating surface, *Journal of Heat Transfer*, 84 (1962) 207-216.
- [22] V. Srinivasan, K. Moon, D. Greif, D.M. Wang, M. Kim, Numerical simulation of immersion quenching process of an engine cylinder head, *Applied Mathematical Modelling*, 34 (2010) 2111–2128.
- [23] R. Kopun, L. Skerget, D. Zhang, B. Stauder, D. Greif, Numerical simulation of immersion quenching process for cast aluminium part at different pool temperatures, *Applied Thermal Engineering*, 65 (2014) 74–84.
- [24] J.F. Davidson, C.E. Sci, A.M. Kennedy, T.I. Chem, E.J. Cullen, T.I. Chem, Spray Quenching, 49 (1970).
- [25] C. Li, S. V Garimella, Prandtl-number effects and generalized correlations for convection and submerged jet impingement, 44 (2001).

- [26] D.H. Wolf, F.P. Incropera, R. Viskanta, Local jet impingement boiling heat transfer, *International Journal of Heat and Mass Transfer*, 39 (1996) 1395–1406.
- [27] D.E. Hall, F.P. Incropera, Jet Impingement Boiling From a Circular Free-Surface Jet During Quenching : Part 1 Single-Phase, *Journal of heat transfer*, 123 (2017) 901–910.
- [28] W. Timm, K. Weinzierl, A. Leipertz, Heat transfer in subcooled jet impingement boiling at high wall temperatures, *International journal of heat and mass transfer*, 46 (2003) 1385–1393.
- [29] N. Karwa, L. Schmidt, P. Stephan, Hydrodynamics of quenching with impinging free-surface jet, *International journal of heat and mass transfer*, 55 (2012) 3677–3685.
- [30] G. Spanos, R.W. Fonda, R.A. Vandermeer, A. Matuszeski, Microstructural changes in HSLA-100 steel thermally cycled to simulate the heat-affected zone during welding, *Metallurgical and Materials Transactions A*, 26 (1995) 3277–3293.
- [31] S.I. Kim, Y. Lee, Influence of cooling rate and boron content on the microstructure and mechanical properties of hot-rolled high strength interstitial-free steels, *Metals and Materials International*, 18 (2012) 735–744.
- [32] G.E. Totten, *Steel Heat Treatment Handbook: Equipment and Process Design*, (2006).
- [33] S. Vakili, M.S. Gadala, Boiling Heat Transfer of Multiple Impinging Jets on a Hot Moving Plate, *Heat Transfer Engineering*, 34 (2013) 580-595.

- [34] N. Karwa, L. Schmidt, P. Stephan, Hydrodynamics of quenching with impinging free-surface jet, *International journal of heat and mass transfer*, 55 (2012) 3677–3685.
- [35] T. Kim, D.-W. Oh, K.H. Do, J.M. Park, J. Lee, Effect of Initial Temperature of a Cylindrical Steel Block on Heat Transfer Characteristics of Staggered Array Jets During Water Jet Quenching, *Heat transfer engineering*, 36 (2015) 1037–1045.
- [36] J. Lee, S. Sohn, J. Park, Visual observation of circular water jet impingement boiling on stationary hot steel plate, *Journal of Heat Transfer*, 137 (2015) 80911.
- [37] J. Lee, S. Sohn, S.G. Lee, Boiling visualization of two adjacent impinging jets on hot steel plate, *Journal of Heat Transfer*, 138 (2016) 20909.
- [38] N. Karwa, T. Gambaryan-Roisman, P. Stephan, C. Tropea, experimental investigation of circular free-surface jet impingement quenching: Transient hydrodynamics and heat transfer, *Experimental thermal and fluid science*, 35 (2011) 1435–1443.
- [39] D.E. Hall, F.P. Incropera, R. Viskanta, Jet impingement boiling from a circular free-surface jet during quenching: part 1 single-phase jet, *Journal of heat transfer*, 123 (2001) 901-910.
- [40] S. Ishigai, S. Nakanishi, T. Ochi, Boiling heat transfer for plane water jet impinging on a hot surface, *Proceedings of the 6th International Heat Transfer Conference. Vol. 1. Washington DC: Hemisphere Publishing Corp*, (1978).
- [41] P.L. Woodfield, M. Monde, A.K. Mozumder, Observations of high temperature impinging-jet boiling phenomena, *International Journal of Heat and Mass Transfer*, 48 (2005) 2032–2041.

- [42] H. Matsueda, M. Monde, S. Matsuda, Characteristics of transient heat transfer during quenching of a vertical hot surface with a falling liquid film, *Heat Transfer-Asian Research*, 36 (2007) 345–360.
- [43] M.A. Islam, M. Monde, P.L. Woodfield, Y. Mitsutake, Jet impingement quenching phenomena for hot surfaces well above the limiting temperature for solid-liquid contact, *International Journal of Heat and Mass Transfer*, 51 (2008) 1226–1237.
- [44] P.L. Woodfield, A.K. Mozumder, M. Monde, On the size of the boiling region in jet impingement quenching, *International Journal of Heat and Mass Transfer*, 52 (2009) 460–465.
- [45] M.N. Hasan, M. Monde, Y. Mitsutake, Homogeneous nucleation boiling during jet impingement quench of hot surfaces above thermodynamic limiting temperature, *International Journal of Heat and Mass Transfer*, 54 (2011) 2837–2843.
- [46] M. Zarringhalam, A. Karimipour, D. Toghraie, Experimental study of the effect of solid volume fraction and Reynolds number on heat transfer coefficient and pressure drop of CuO -Water nanofluid, *Experimental Thermal and Fluid Science*, 76 (2016) 342–351.
- [47] D. Toghraie, Numerical thermal analysis of water's boiling heat transfer based on a turbulent jet impingement on heated surface, *Physica E: Low-dimensional Systems and Nanostructures*, 84 (2016) 454–465.
- [48] A.K. Mozumder, M. Monde, P.L. Woodfield, M.A. Islam, Maximum heat flux in relation to quenching of a high temperature surface with liquid jet impingement, *International Journal of Heat and Mass Transfer*, 49 (2006) 2877–2888.

- [49] J. Hammad, Y. Mitsutake, M. Monde, Movement of maximum heat flux and wetting front during quenching of hot cylindrical block, *International Journal of Thermal Sciences*, 43 (2004) 743–752.
- [50] C.E. Bates, Selecting Quenchants to Maximize Tensile Properties and Minimize Distortion in Aluminum Parts, *Journal of Heat Treating*, 5 (1987) 27–40.
- [51] N. I. Kobasko, Intensive Steel Quenching Methods. Theory and Technology of Quenching, *Springer-Vedag, New York*, (1992) 367-389.
- [52] M.A. Aronov, N.I. Kobasko, J.A. Powell, A.M. Freborg, B.L. Ferguson, Intensive quenching theory and application for imparting high residual surface compressive stresses in pressure vessel components, *ASME 2002 Pressure Vessels and Piping Conference. American Society of Mechanical Engineers*, 125 (2003) 188-194.
- [53] S. Tweomey, The application of numerical filtering for the solution of integral equations encountered in indirect sensing measurements, *Journal of the Franklin Institute*, 279 (1965) 95-109.
- [54] J.V. Beak, B. Blackwell, C.R. St. Clair, Inverse heat conduction, *Wiley, New York*, (1985).
- [55] H.K.D.H. Bhadeshia, Model for transition from upper to lower bainite, *Materials Science and Technology*, 6 (1990) 592–603.
- [56] F.S. LePera, Improved etching technique for the determination of percent martensite in high-strength dual-phase steels, *Metallography*, 12 (1979) 263–268.

- [57] T. Giordani, T.R. Clarke, C.E.F. Kwietniewski, M.A. Aronov, N.I. Kobasko, G.E. Totten, Mechanical and metallurgical evaluation of carburized, conventionally and intensively quenched steels, *Journal of materials engineering and performance*, 22 (2013) 2304–2313.
- [58] E. Erişir, S. Gümüş, O.G. Bilir, Microstructural Characterization of Medium Carbon Dual Phase Steels after Intermediate Quenching, *Proceedings of Metal*, (2013) 15-17.
- [59] M. Akmal, A.M.T. Omar, M.S. Hamed, Experimental investigation of propagation of wetting front on curved surfaces exposed to an impinging water jet, *International Journal of Microstructure and Materials Properties*, 3.4–5 (2008) 654–681.

## Abstract in Korean

본 논문에서는 수분류 충돌 제트를 적용하여 고온으로 가열된 표면의 급속냉각 시 발생하는 복잡한 비등 열전달 특성을 실험적으로 연구하였다. 복잡한 비등 현상을 보다 명확히 규명 하기 위해, 열유속계이지를 설계하여 냉각 표면에 가까운 시편 내부의 온도 분포를 실시간으로 측정 하였으며, 동시에 고해상도 시각화 장치를 이용하여 비등가시화를 진행하였다. 또한 금속 시편의 균일한 고온(900℃ 이상) 가열을 위해, 맞춤형 유도코일 설계, 적용하였다. 냉각 표면에서의 온도분포, 열유속 및 열전달계수는 측정된 시편 내부의 온도 분포를 기반으로 자체 개발한 역열전도 해석법을 적용 함으로서 수치적으로 계산되었다. 그리고, 충돌 표면에서 측정된 열전달계수는 불확실성 해석에 따른 오차 범위를 밝힘으로써 정확한 실험 결과를 얻었다. 주요 실험 변수로써 노즐의 갯수, 레이놀즈 수( $Re$ ), 노즐과 노즐 사이의 간격( $L/d_n$ )을 조정하였다. 실시간으로 발생하는 수분류 제트의 복잡한 비등현상의 명확한 규명을 위해 충돌 제트의 개수를 순차적으로 늘려가며 국부 열전달 현상을 규명하였고, 최종적으로 엇갈림 배열로 설계된 충돌제트 노즐의 냉각능 평가를 위해 기존의 담금질과 같은 4가지 열처리 냉각을 모사 설계하여 냉각능 특성을 비교, 검토하였으며, 표면 미세조직 검사를 통해 이를 다시금 확인하였다.

수분류 충돌 제트는 비등 현상에 의해 발생하는 냉각수와 고온의 강제 표면 사이에 열저항 역할을 하는 증기막 층을 빠르게 제거함으로써, 높은 열 및 물질 전달을 가지게 된다. 이때 수반되는 복합적인 비등 현상 규명을 위해 하나의 충돌제트를 넓은 평판 형태의 고온 시편을 수직위

중심에 설치하였으며 생각하는 경우 일어나는 비등현상을 규명하였다. 분사 냉각에 따른 비등 가시화 이미지를 통해 표면 젖음성을 기준으로 특징적인 세 부분(젖음영역, 젖음전방영역, 건조영역)이 발생함을 확인하였다. 또한 특정 시간에서의 비등 가시화와 동반되는 표면 열전달 특성 동기화를 통해 각 부분이 특징적인 비등현상과 연관됨을 확인하였다. 젖음영역은 분사 냉각에 의해 표면의 온도가 충분히 낮아진 부분으로, 표면이 냉각수로 젖어 있는 상태이며 주로 천이 비등 현상과 단상 대류 열전달이 일어나는 것이 확인되었다. 반면, 건조영역은 온도가 높으며 막비등 현상이 일어나기 때문에 표면의 건조한 상태가 유지되었고, 두 영역의 사이에 존재하는 젖음 전방영역은 막비등 현상이 사라지며 핵비등 열전달이 시작되는 구간으로 높은 열유속이 동반됨을 확인하였다. 최대 열유속값이 시간에 따라 감소함을 확인되었는데, 이는 외곽지역 일수록 핵비등 현상이 늦게 발생하므로 시편의 중심보다 낮은 온도에서 핵비등이 일어나기 때문임을 규명하였다. 또한, 시간에 따른 젖음반경과 최대 열유속반경을 비교하여 표면의 젖음이 일어나는 구간과 핵비등 열전달이 동일시 되며 선형의 기울기를 보임을 확인 하였고, 이처럼 상관분석을 통해 특정시간 이후 동반되는 준평형상태를 확인하였다.

앞선 연구에 이어 두 개의 충돌제트의 상호작용에 따른 국부 열전달 특성을 평가하였다. 실험 변수로 두 분사 노즐 사이의 거리를 달리 하였으며, 냉각 분석에 앞서 유동 가시화를 통해 노즐 사이의 거리에 따라 수반되는 유동 특성을 변화를 확인하였다. 이후 냉각 실험을 통해 분사된 두 개의 충돌 제트는 중심 지점에서 발생하는 상호흐름이 표면의 젖음성 및 국부적인 비등현상에 지대한 영향을 미침을 확인되었다. 또한,

앞의 단일 제트 분사를 사용한 냉각실험 결과와 두 개의 제트의 결과 비교를 통해 두 개의 제트를 사용 시 기대할 수 있는 열전달 향상에 관해 비교, 분석을 진행하였다. 두 제트의 가운데 부분에서 간섭에 의한 제트 유동이 형성됨을 확인 하였으며, 국부 열전달 현상에 지대한 영향을 미침을 확인하였다.

최종적으로 수분류 충돌제트의 높은 냉각 특성을 확인하기 위한 비교 실험을 진행하였다. 본 연구에서는 종래의 열처리 냉각방식(conventional method)과 급속냉각(intensive quenching)의 냉각능 비교를 위해 총 4 가지 열처리 냉각 방식을 선정하였다. 비교 실험을 위해 각 냉각 방식을 위한 장치를 설계, 제작하였으며, 담금질 방식의 경우 작동유체를 물과 냉각유를 사용하여 냉각을 진행하였다. 서로 다른 방식의 급속냉각 열처리 냉각방식으로 미국 IQ사에서 개발 및 상용화한 강제 담금질 방식(Forced immersion quenching), 다수의 수분류 제트를 엇갈림 배열로 설계된 제트충돌냉각(Multiple jet quenching) 방식을 사용하였다. 각 냉각 방식은 현저한 냉각능 차이를 보여주었으며, 제트충돌냉각, 강제 담금질 방식, 담금질 방식(물), 담금질 방식(냉각유)의 순서로 높은 냉각성능을 보임을 확인하였다. 또한, 냉각후 표면에 발생하는 미세조직, 기계적 성질 비교분석을 진행하여 냉각능에 따라 높은 비율의 마르텐사이트 조직과 높은 강성 및 인성을 가짐을 확인하였다.

**주요어** : 수분류 충돌제트, 비등 열전달, 표면 젖음성, 급속 냉각, 역열전도 해석, 미세조직 분석

**학번** : 2011-20732